ABSTRACT

Title of dissertation: LAB-ON-CMOS SENSORS AND REAL-TIME IMAGING FOR BIOLOGICAL CELL MONITORING

Bathiya Prashan Bandara Senevirathna
Doctor of Philosophy, 2019

Dissertation directed by: Professor Pamela Abshire
Department of Electrical & Computer Engineering

Monitoring biological cell growth and viability is essential for *in vivo* biomedical diagnosis and therapy, and *in vitro* studies of pharmaceutical efficacy and material toxicity. Conventional monitoring techniques involve the use of dyes and markers that can potentially introduce side effects into the cell culture and often function as end-point assays. This eliminates the opportunity to track fast changes and to determine temporal correlation between measurements. Particularly in drug screening applications, high-temporal resolution cell viability data could inform decisions on drug application protocols that could lead to better treatment outcomes.

This work presents development of a lab-on-chip (LoC) sensor for real-time monitoring of biological cell viability and proliferation, to provide a comprehensive picture of the changes cells undergo during their lifecycle. The LoC sensor consists of a complementary metal-oxide-semiconductor (CMOS) chip that measures the cell-to-substrate coupling of adherent cells that are cultured directly on top. This technique is non-invasive, does not require biochemical labeling, and allows for

automated and unsupervised cell monitoring. The CMOS capacitance sensor was designed to addresses the ubiquitous challenges of sensitivity, noise coupling, and dynamic range that affect existing sensors. The design includes on-chip digitization, serial data output, and programmable control logic in order to facilitate packaging requirements for biological experiments. Only a microcontroller is required for read-out, making it suitable for applications outside the traditional laboratory setting. An imaging platform was developed to provide time-lapse images of the sensor surface, which allowed for concurrent visual and capacitance observation of the cells. Results showed the ability of the LoC sensor to detect single cell binding events and changes in cell morphology. The sensor was used in in vitro experiments to monitor chemotherapeutic agent potency on drug-resistant and drug-sensitive cancer cell lines. Concentrations higher than 5 μM elicited cytotoxic effects on both cell lines, while a dose of 1 μM allowed discrimination of the two cell types. The system demonstrates the use of real-time capacitance measurements as a proof-of-concept tool that has potential to hasten the drug development process.

LAB-ON-CMOS SENSORS AND REAL-TIME IMAGING FOR BIOLOGICAL CELL MONITORING

by

Bathiya Senevirathna

Dissertation submitted to the Faculty of the Graduate School of the
University of Maryland, College Park in partial fulfillment
of the requirements for the degree of
Doctor of Philosophy
2019

Advisory Committee:
Professor Pamela Abshire, Chair/Advisor
Professor Reza Ghodssi
Professor Timothy Horiuchi
Professor Robert Newcomb
Professor Ian White
Professor Elisabeth Smela*

Dedication

To my parents.

Acknowledgments

I would first like to express my gratitude to my advisor, Dr. Pamela Abshire. I thank her for giving me a chance to work on this exciting research, for her patient guidance throughout all aspects of the research, and for being such a wonderful mentor. Her infectious enthusiasm and positive attitude makes everyone around her a better person. A special thanks as well to Dr. Elisabeth Smela for her guidance, and valuable and constructive suggestions during the planning and development of this work, as well as the resources for performing experiments.

I would like to thank Dr. Pamela Abshire, Dr. Reza Ghodssi, Dr. Timothy Horiuchi, Dr. Robert Newcomb, Dr. Elisabeth Smela*, and Dr. Ian White for graciously agreeing to serve on my dissertation committee and sparing the time to review the work.

I would of course like to thank all my lab mates at the Integrated Biomorphic Information Systems (IBIS) Laboratory. Alex Castro for wide-ranging discussions, collaborations for coursework, and general advice throughout my entire graduate student life. Sheung Lu for his invaluable help on this and other projects. From working on chip packaging, to the discussions on eccentric ideas, and the help setting up and performing experiments, this dissertation could not have been realized without his help. Marc Dandin for the valuable technical discussions, logistical help in moving the project forward, and general life advice. His influence at IBIS cannot be overstated. Timir Datta for the early mentorship and allowing me to get involved in the projects that eventually led me to this work. Tsung-Hsueh Lee and Andrew

*I would like to thank Dr. Elisabeth Smela for also being a part of my committee, although she was unable to attend in person due to last minute scheduling conflicts.

Berkovich for advice and assistance setting up CAD tools for VLSI design. Emily Naviasky, Somashekar Prakash, and Nicole Nelson for laying the groundwork for this project.

I am particularly grateful to our collaborators from the University of Oulu and Linköping University, for the technical discussions in developing this project. In particular, Joni Kilpijärvi and Dr. Anita Lloyd Spetz for assembling devices that were crucial for obtaining some of the experimental data presented in this dissertation. I would additionally like to thank Dr. John Basile for the valuable insight on this project from a biologists perspective, and Dr. Yan Shu for graciously providing the cells used in experiments, both from the University of Maryland, Baltimore.

I would also like to express my appreciation to Dr. Ricardo Araneda, Dr. Jonathan Simon, Dr. Bradley Hatfield, Adriane Fang, Karen Bradley for the lively dialogue on other collaborations. Jooik Chung, Shashikant Koul, Jaime Campos, and honorary IBIS member, Estefany Carillo, thank you for the broad discussions and being a positive influence in grad school. Diane Woods and Kirubel Mersha, thank you for the impetus to go to graduate school and inspiration.

I would also like to thank numerous staff at ECE/ISR/IT, including Jeff McKinney, Gwen Flasinski, Jay Renner, and Regina King for support resources, and Dr. Melanie Prange for the academic support and valuable advice during my time at UMD.

Finally, I'd like to thank my parents, aunts, uncles, and cousins for their continuous support and words of encouragement.

Table of Contents

List of Tables

List of Figures

List of Abbreviations

ADC	analog-to-digital converter
CAN	controller area network
CBCM	charge-based capacitance measurement
CMOS	complementary metal-oxide semiconductor
CS	charge sharing
CTF	capacitance to frequency
DI	deionized
ECIS	electric cell-substrate impedance sensing
FEM	finite element method
FPGA	field-programmable gate array
FPR	false positive rate
I^2C	inter-integrated circuit
IBIS	Integrated Biomorphic Information Systems
IPA	isopropyl alcohol
KAMA	Kaufman adaptive moving average
LoC	lab-on-chip
LoCMOS	lab-on-CMOS
LOD	limit of detection
LTCC	low-temperature co-fired ceramic
MAI	moving average indicator
PCB	printed circuit board
ROC	receiver operating characteristic
RPMI	Roswell Park Memorial Institute
SPI	serial peripheral interface
SSD	sum of squared difference
TPM	template matching
TPR	true positive rate

VCO voltage-controlled oscillator

Chapter 1

Introduction

1.1 Lab-on-CMOS Systems

Microelectronic biosensors have the potential to provide low-cost, adaptable, and portable devices for applications in fields such as biology, environmental science, and medicine. In particular, a ubiquitous experimental challenge is to monitor the proliferation of cells over time to determine their response to stimuli or environmental conditions. Monitoring cell growth and migration is an important tool for optimizing cell culture conditions, testing drugs, and screening materials for biocompatibility and toxicity [14]. Conventional approaches involve the use of dyes and markers that can potentially introduce side-effects into the cell culture [15] and often function as end-point assays, eliminating the opportunity to track fast changes and to determine temporal correlation between measurements. Therefore it is important to develop new techniques to perform these measurements. Lab-on-chip devices have shown promise in changing the way that biological samples are analyzed. They allow for smaller sample volumes, reduced cost, faster reaction kinetics, and higher throughput than conventional approaches [16, 17]. Another important advantage of lab-on-chip systems is their potential for automated and unsupervised data collection. In most instances, however, lab-on-chip devices comprise of a passive sensing layer that requires additional external instrumentation for readout and

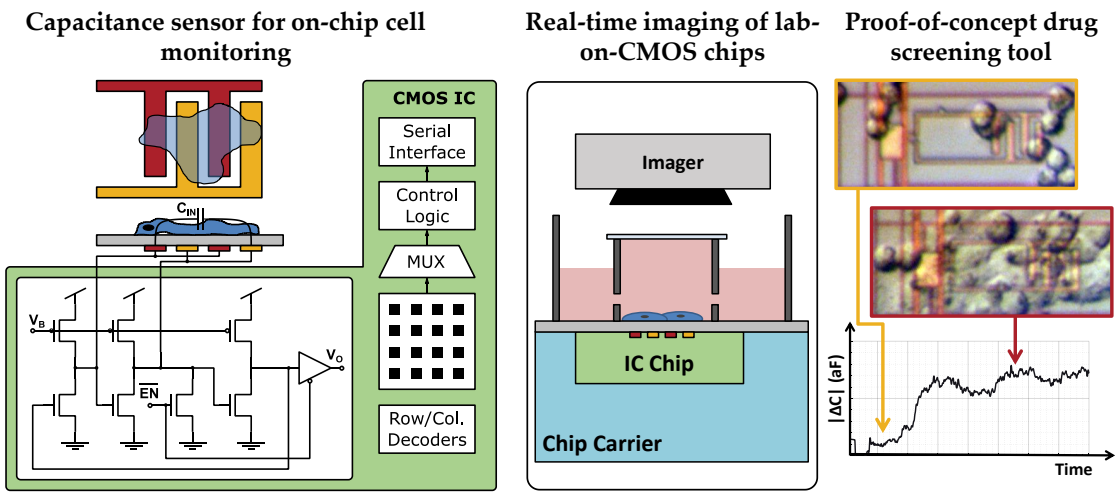

Figure 1.1: Conceptual diagram of sensor system.

signal processing [6, 16].

Recently, complementary metal-oxide semiconductor (CMOS) technology has become an attractive platform for lab-on-chip systems since it facilitates the incorporation of sensing and actuation in intimate contact with readout and electronics, producing systems with smaller size, higher sensing density, and higher sensing fidelity. CMOS technology offers the advantages of having low static power requirements and good noise immunity [16], as well as being widely available and facilitating integration with commercial electronics. This research describes the development of a fully integrated lab-on-CMOS (LoCMOS) capacitance biosensor for on-chip cell sensing applications. The specific focus of the work is on developing a low-cost and low-complexity portable system that can be used for live cell experiments, including drug screening assays. The CMOS sensor chip aims to characterize the adherence of biological cells to a substrate, which is an important indicator of cell viability, through high-resolution surface capacitance measurements. This sensing paradigm relies on the biophysical morphology of adherent cells. Healthy cells with

well-formed membranes create small changes in the dielectric properties of the area around the electrodes [18, 19]. Additionally these cells bind tightly to their substrates in comparison to dead or compromised cells [20]. These properties provide an avenue for monitoring cell health through an integrated LoCMOS system [9]. An imaging platform for CMOS chips is then presented that allows for simultaneous data recording and image acquisition to provide ground-truth data for sensor validation. Finally the LoCMOS system is used as a proof-of-concept drug screening tool. An overview of the goals of this research is shown in Fig. 1.1.

1.2 Research Contributions

The primary contributions of this work are highlighted in the points below:

- **Design of CMOS capacitance sensors for on-chip cell monitoring**. A low-cost, low-complexity CMOS sensor was developed that provides high-resolution capacitance measurements. The chip is designed with on-chip signal digitization and serial communication, which facilitate sensor packaging for experiments, and allows for readout with any commercial microcontroller. No large laboratory equipment or electrical hardware is required for operation, enabling future extensions to point-of-care (PoC) devices.

- **Real-time imaging of lab-on-CMOS chips**. An imaging platform was developed for simultaneously making recordings using a CMOS sensor and taking images of the sensor surface. This allowed for validation of sensor measurements by providing ground-truth images for cell sensing applications.

The imaging does not interfere with cell viability and maintains image quality over several days of experiments.

- **Drug screening on chip**. Proof-of-concept experiments are performed to characterize the potency of chemotherapeutic drugs on cells using the lab-on-CMOS capacitance sensor. Results showed the ability to discriminate drug-sensitive and resistive cell lines using capacitance measurements. The high temporal-resolution data provided by the chip allowed quantification of cell death kinetics.

1.3 Thesis Organization

Chapter 2 provides background information on cell-substrate adhesion, and techniques to monitor cell viability. An overview of CMOS-based capacitance sensors is also presented. **Chapter 3** introduces the capacitance sensor developed in this work. The front-end design is discussed along with a system-level description of the chip, and simulation results. The fabricated chip is characterized on the benchtop to extract performance metrics. **Chapter 4** presents results of *in vitro* experiments using cancer cell lines that are grown on the sensor. The chapter discusses packaging methods, the experimental protocol, results, and presents quantification metrics to track population cell growth. **Chapter 5** introduces the real-time imaging platform. Background material on visualizing cells is presented. The hardware implementation is described and results of simultaneous imaging and capacitance recording in *in vitro* experiments are shown. Images are used to validate the capac-

itance sensor measurements and show the ability to detect single-cell morphology changes. Finally, preliminary work on image processing to perform automatic cell detection and coverage estimation is presented. Results are correlated with the data recordings from the LoCMOS sensor. Chapters 6 and 7 present work towards using the chip as a tool for drug development. **Chapter 6** shows results of using the sensor to detect cell mitosis activity, is an important prognostic factor and indicator of metastatic risk in cancer patients. **Chapter 7** presents results of drug screening assays done on chip where drug-sensitive and drug-resistive cell types are exposed to a cancer drug. Results show the ability to discriminate cell lines using capacitance sensor measurements. The data is then used to extract cell death kinetics.

Chapter 2

Capacitance Sensing on CMOS

2.1 Sensing Approaches

Many types of CMOS-based capacitance sensors have been developed and used in various applications. The fundamental sensing mechanism is to detect changes in the dielectric properties of a material with respect to a baseline such as air or liquid solution. Common applications of these types of sensors include detecting proximity, humidity, and force detection. One of more ubiquitous applications in modern times are their use in human interface devices such as trackpads, smartphone screens, and non-mechanical buttons. A number of different transduction methods have been employed in CMOS technology for use in capacitance measurements. Two specific mechanisms that have been developed for biological applications are charge-based and time/frequency-based sensors.

2.1.1 Charge based capacitance measurements

Charge based capacitance sensors have been used in many prior applications, initially starting with characterizing interconnect capacitances [21, 2] and fingerprint sensing [1, 22]. This transduction mechanism has since been adapted for use in numerous biological cell applications [9, 23, 24, 25, 10].

2.1.1.1 Fingerprint Sensor

Lee *et al.* introduced a fingerprint sensor chip based on an array of capacitance sensors that use the charge sharing (CS) sensor scheme [1]. Fig. 2.1 illustrates this technique. The input analyte (finger) acts as the upper electrode of the capacitor, and the metal plate on the chip acts as the other electrode. The capacitance C_S is related to the capacitance being sensed and will decrease as the distance between the finger and the passivation layer increases. Therefore C_S will be at its maximum value when a ridge on the finger contacts the passivation layer. Capacitances C_{p1} and C_{p2} represent parasitic capacitances on nodes N_1 and N_2.

Sensing of the capacitance works in two phases: precharge and evaluation. In the first precharge phase, S_1 and S_3 are on while S_2 is off, causing N_1 and N_2 to

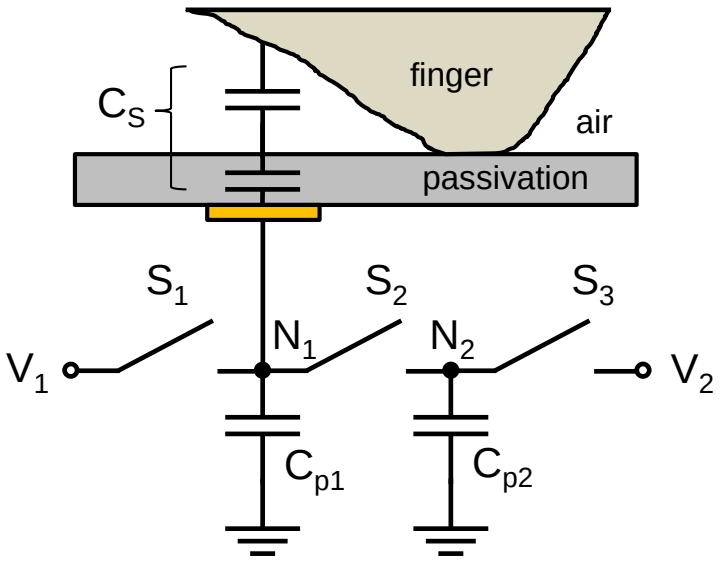

Figure 2.1: Schematic of the charge sharing measurement system. [1]

charge to known voltages V_1 and V_2, respectively. In the next stage the switches are flipped. This causes the charges on the two nodes to re-distribute, giving a final output voltage of:

$$V_O = V_{N1} = V_{N2} = \frac{C_{p1}V_1 + C_{p2}V_2 + C_S V_1}{C_{p1} + C_{p2} + C_S} \tag{2.1}$$

The output voltage is thus related to the input sensed capacitance, and it drops off rapidly as the distance between finger and sensor surface increases [1].

2.1.1.2 Metal Interconnect Characterization

Another charge-based sensing scheme is charge-based capacitance measurement (CBCM) which was introduced by Chen *et al.* to analyze parasitic capacitances of overlaid metal interconnents on CMOS chips [2]. Fig. 2.2 shows the CBCM-based test structure used for this characterization. The structure consisted of identical PMOS and NMOS transistors that were controlled by non-overlapping signals V_1 and V_2. The capacitance being sensed (C_S) was attached to one pair of transistors. In Fig. 2.2, this amounts to the addition of a grounded metal 2 line that overlaps the existing metal 1 line connected to the right-pair's middle node.

The control signals V_1 and V_2 alternately charge and discharge the interconnect capacitance at a frequency f. The capacitance can be derived by finding the difference between the DC currents I and I' (measured externally using an ammeter):

$$I_{net} = I' - I = C_S V_{DD} f \tag{2.2}$$

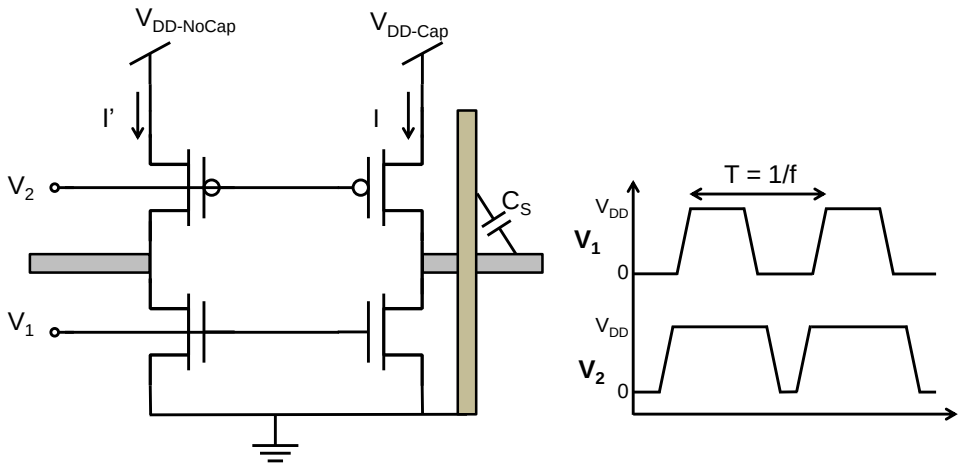

Figure 2.2: Schematic of the CBCM test structure. [2]

The actual capacitance is computed by finding the slope of the I_{net}-V_{DD} curve and dividing by the frequency [2]. In the ideal case, both sides of the CBCM structure will be identical, having the same drain overlap and drain junction capacitances. However, any mismatch between the two sides will limit the minimum achievable resolution.

2.1.2 Frequency-based Capacitance Measurements

The capacitance to frequency (CTF) sensing technique uses capacitive loading to modulate the frequency of oscillating circuits. The oscillating element in these circuits generally consist of a capacitor along with a resistor or inductor. For integrated CMOS sensors, the capacitor is replaced directly with the input sensing electrodes, while the resistor (for an RC element) simply consists of parasitics. Charging and discharging of the element is generally performed using current, resulting in an output frequency that is proportional to 1/RC or $1/\sqrt{LC}$. As an example, Lu *et al.*

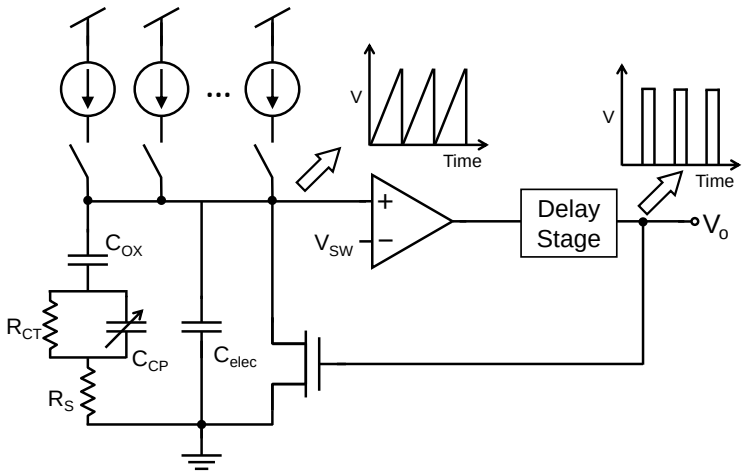

Figure 2.3: Schematic of frequency based capacitance readout circuit. [3]

used a CTF technique to detect the presence of the neurotransmitter dopamine, the binding of which changed the charge profile at the sensor interface, inducing changes in capacitance [3]. Fig. 2.3 shows the CTF-based readout circuit.

The input capacitance (C_{elec}) lies in parallel with parasitics that include interface capacitive impedance (C_{CP}), oxide capacitance (C_{OX}), charge transfer resistance (R_{CT}), and solution resistance (R_S). R_{CT} and R_S are assumed to be negligible and so the overall impedance is purely capacitive. A tuneable bank of current sources that range from 1 μA to 16 μA is used to charge C_{elec}, producing a ramping signal. When this signal reaches a certain switching voltage (V_{SW}), the comparator output goes high and after a delay stage, causes the capacitor charge to reset through an NMOS transistor. This feedback loop sustains a continual generation of output pulses at a frequency:

$$f = \left[\frac{C_S V_{SW}}{I_B} + \tau_d\right]^{-1} \tag{2.3}$$

where I_B, τ_d, and C_S are the charging current, time delay of the output stages, and overall input capacitances, respectively.

2.2 Cell Adhesion & and Viability sensing

2.2.1 Cell-Substrate Coupling

Adherent cells modify the dielectric properties at the cell-substrate interface as they settle onto a substrate, adhere, proliferate, and eventually lift off due to cell death, forced detachment, or other morphological changes. Fig. 2.4 shows a diagram of three stages of the cell adhesion process. When cells are first placed in suspension they drift downwards and make an initial attachment with the substrate (top panel). They then begin attaching to the surface through a variety of cell adhesion mechanisms (middle panel) [4]. The cells then anchor and flatten themselves, spreading outward over a larger area until they reach their maximum spread (bottom panel) [26]. Healthy cells will continue to bind tightly to the substrate and spread out as they grow and proliferate, while compromised cells contract and may even lift off from the surface entirely. These changes in cell morphology modulate the dielectric properties of the cell-substrate interface, which can be measured as changes in surface capacitance [9].

2.2.2 Non-Electronic Techniques

Numerous non-electronic methods for quantifying cell adhesion have been explored [26]. Traction force microscopy is a technique that involves culturing cells

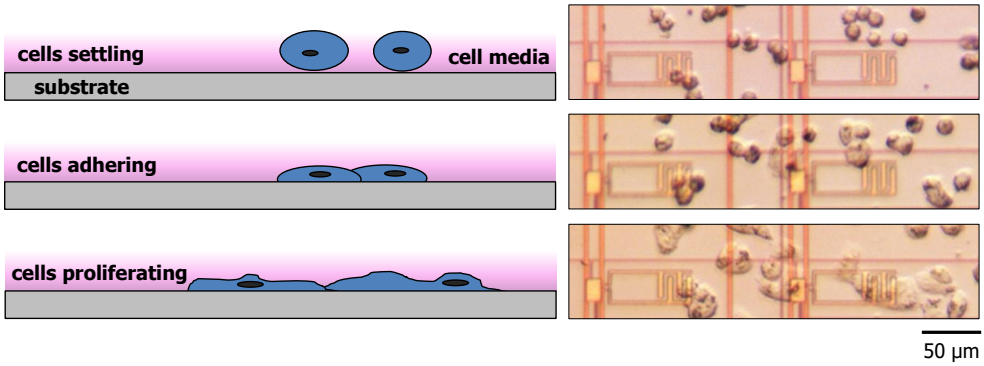

Figure 2.4: Cell dielectric layer formation on a solid substrate. Left: Cells in suspension first drift downwards to settle on the surface. They begin adhering to the surface through various mechanisms involving cell adhesion molecules [4]. The cells then anchor and spread outward as they proliferate. Right: Microscope images of cells cultured on the biosensor surface, during the settling, adhering, and proliferating phases (top to bottom).

onto a polyacrylamide gel that has been embedded with fluorescent beads. When cells adhere they generate traction forces that can be quantified by monitoring the fluorescent beads [27]. Another technique involves the exposure of cells to shear fluid flow through microfluidic channels [28]. The strength of cell adhesion is related to the balance between the adhesion strength and the shear fluid forces. Another mechanical technique of quantifying adhesion is to use a micropipette to apply a suction force to the top of a cell. The minimum amount of force required to pull the cell of the substrate is a measure of its adhesion strength [29].

Traditional methods of assessing cell viability involve direct visual counting of healthy cells or indirect measurement of a separate biomarker. One method involves incubating cells with a reagent (such as Alamar Blue) that develops a visible color through the metabolic activity of active cells. Measurement of the color development is performed using spectrophotometry and is then an analogue for cell viability [30, 31]. Another method of assessing cell viability is to analyze the health of cell

membranes. When a dye, such as trypan blue, is applied, healthy cells with intact membranes will exclude the dye, whereas dead cells will be stained. The number of cells that have not been stained can then be counted under a microscope to get an indication of viability. These optical techniques typically require microscopes and optical filters for measurement. Methods that require the addition of a dye or fluorescent agent can compromise viability and lead to cell death [32]. Additionally these approaches require sampling of the analyte, which might not be feasible for small culture volumes. Therefore a label-free detection method would be beneficial. Furthermore, many traditional characterization methods are end-point assays which provide a measure of adhesion only at the end of an experimental procedure. Many parallel experiments are required to obtain a temporal sequence of discrete sample points, with temporal accuracy limited by the variability across samples and the sampling technique. Much richer information about the dynamics of cell growth would be available from a real-time measurement method.

A number of physical transduction mechanisms have been introduced for monitoring biological cells. Impedance spectroscopy, quartz crystal microbalances, and surface acoustic waves [33, 34, 35], commonly used for characterization of material properties, have been used to study cells; however they generally require large external equipment for readout. Ion-sensitive FETs have also been used to detect bacterial activity [36], but they are generally used to measure analogues of cell activity (such as pH changes), rather than viability directly. Amperometry has also been used in cell detection [37], however post-fabrication of electrodes on CMOS chips are required.

2.2.3 Electric Cell-Substrate Impedance Sensing

One of the most popular and well-established electronic methods of cell sensing is electric cell-substrate impedance sensing (ECIS), first introduced by Giaever and Keese [38, 39]. This measurement technique monitors the impedance across a pair of sense and counter electrodes. In general, a 1 V amplitude AC signal is applied to the electrodes through a 1 $M\Omega$ resistor at a given frequency (nominally 4 kHz). A separate lock-in amplifier is used to detect the phase and magnitude of the resulting signal. A schematic of the readout system is shown in Fig. 2.5.

The detected signal is fitted to an equivalent resistor and capacitor model to extract barrier resistance, membrane capacitance, and current flow parameter values [5]. The resistance and capacitance of the electrodes (typically gold) are assumed not to change, so any measured changes in resistance and capacitance values is due to the cells altering the current flow.

ECIS systems are commercialized and have been used in several studies. Gi-

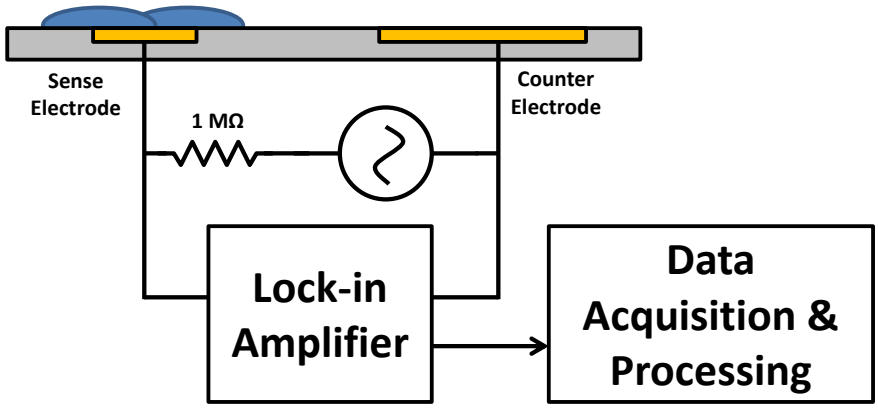

Figure 2.5: Schematic of the ECIS measurement system. [5]

aever and Keese initially performed studies on cell attachment, motion, and effects of metabolite application [40, 5, 38]. Other research has also been performed using commercial ECIS systems. Balasubramanian *et al.* studied changes in cell morphology induced by integrin binding peptides [33]. Opp *et al.* monitored cytotoxicity of human endotheliel cells to different dosages of metabolies [41]. Allen-Gipson *et al.* observed wound healing characteristics of bronchial epithelial cells in the presence of cigarette smoke extract [42].

2.2.4 Integrated Sensing on CMOS

CMOS-based capacitance sensors have been developed for a number of cell monitoring applications. These chips implement arrays of sensing electrodes that detect capacitive changes as cells adhere to and grow across the surface of the chip. The electrodes are generally insulated from the cell culture environment and so limit undesirable electrochemistry that may otherwise occur.

Both charge sharing and charge-based capacitance measurement sensing have been used in LoCMOS systems for live cell sensing experiments. Prakash *et al.* used a CS-based chip to track adhesion and proliferation of smooth muscle and breast cancer cells [43, 9]. Ghafar-Zadeh *et al.* used a CBCM structure to measure growth of bacteria in medium [44, 25]. This system included a $\Sigma\Delta$ ADC to convert the output voltage to a serial stream of bits that is read off-chip using a field-programmable gate array (FPGA). Prakash *et al.* extended the single-ended CBCM structure to a fully differential version with rail-to-rail output [45, 46]. It showed a

measured resolution of 15 fF based on benchtop experiments.

As described previously, any mismatch in the CBCM structures can limit the resolution of the sensors. Additionally, if current subtraction is done on-chip it is possible for the parasitic mismatches to drive the output signal into saturation at the zero-level baseline [23, 47]. One method to combat this is to use a bank of reference currents in the CBCM structure to do offset cancellation [24, 12]. Alternatively, Prakash *et al.* extended the differential CBCM design to include floating-gate trimming circuits to perform the mismatch and offset cancellation [23].

For the CTF paradigm, Cuoniot *et al.* used a five-stage ring oscillator loaded with five separate large interdigitated electrodes (total area 100×100 or 200×200 μm^2) to detect bacteria in saline buffer solution [48]. Table 8.1 presents a summary of existing work.

2.2.5 Discussion of Integrated CMOS Approaches

Mismatch & Offset Capacitance. Single-ended CS or CBCM systems have high sensitivity to capacitive changes but can be limited in resolution due to parasitics. Additionally, the permittivity of the immediate surroundings of the electrode can create a large offset capacitance that can reduce the effective dynamic range of the sensor. The differential CBCM systems described previously were shown to compensate for parasitics, to increase dynamic range, and to give high resolution readings, especially when post-fabrication compensation can be completed (e.g. using floating gate trimming [23]). However, these systems still require a

complex readout system and initial programming stage. Capacitance to frequency based transduction systems have the benefit of being inherently resistant to large offset capcitances and parasitic mismatch. This is because there is technically little limit to the range of output frequencies at which the oscillators run. If the integration time is long enough, even very slow signals (large capacitances) can be resolved. Single-ended CTF sensors are still subject to the environmental permittivity, which can cause a large baseline frequency shift. This can be removed in post processing, but a differential CTF structure could negate this offset. Damilano *et al.* [49] developed a CTF readout circuit for tactile skin sensors that uses a second electrode to generate a reference frequency that was used to subtract out offsets, creating a "pseudo-differential" setup. Simulation results showed a 10 fF sensitivity per output LSB, with a pixel size of $22 \times 79\ \mu m^2$.

Analog to Digital Conversion. Another important point of consideration for a lab-on-CMOS platform is digitization of the sensor output, since analysis of recorded data will almost exclusively be done digitally. For traditional CS or CBCM sensors, the output signal is an analog voltage that must be sent off-chip to an external ADC. However, this provides a path for the addition of noise into the analog signals and so careful shielding is necessary [50]. In a cell culture environment this may be difficult. As mentioned previously, CBCM sensors with on-chip $\Sigma\Delta$ ADCs have been implemented [25, 12]. In these systems an external FPGA is used to provide the switching signals for the CBCM core circuitry, to decode the $\Sigma\Delta$ bitstream, and to create the array readout controls. This setup has been shown to work in experiments with polystyrene beads and live cells. However, the use of an

FPGA, and the complexity of the signal transduction and control methods increases the required chip readout requirements and may have adverse effects on total system power consumption. This limits future sensor development for use in portable applications. Frequency based systems are inherently suited for digitization because the output signal is digital, with capacitance information encoded in its oscillation frequency. A straightforward method of converting the frequency information into a digital format is to use it to drive a counter [51, 49].

System Readout. It is important to design CMOS chips with packaging considerations in mind. This is especially important for cell sensing applications, since adequate passivation of the exposed electrical traces is required in wet environments. Possible future incorporation of microfludics is also an important factor for consideration [50]. With this in mind, minimizing the number of I/O pads used by the chip is a relevant goal since this will limit the number of possible failure points during packaging. The number of bondpads required depends on how many external bias voltages are required, the number control signals needed for chip control, and how data from an array of sensors is read. On-chip bias circuitry can be used to limit the need for external pins. The control and readout pins generally depend on how many sensors are implemented on chip and the transduction method. In order to reduce the number of pins required, parallel or sequential readout can be used. CBCM-based systems have been used with a parallel readout format where sensors in an array were read in a column-wise fashion [23, 12]. External row selection signals were used to cycle row-by-row through all columns of the array, and data was read through the N_{col} output pins, where N_{col} is the number of columns in the

array.

A sequential readout system cycles through each sensor in the array. This means a single set of readout lines can be used for the entire array, at the cost of a slower total readout speed. Readout of digital data can be further streamlined by reading data out serially. To this end one could leverage ubiquitous serial communication protocols such as serial peripheral interface (SPI), inter-integrated circuit (I^2C) buses, or controller area network (CAN) buses. These systems generally have two signal lines (clock and data) and can be interfaced with most modern microcontrollers. Another benefit is the ability to have multiple devices on the same readout bus, thereby allowing for multiple chips to be interfaced together.

2.2.6 This Work

The standard methods of monitoring cell adhesion and viability outlined in Section 2.2.2 have been used for a number of applications. However, they use specialized methods that often require the use of large laboratory-based equipment. These methods only provide data at discrete time points, so higher throughput monitoring would be labor-intensive. Additionally they generally involve physical removal of samples for each observation, which might not be feasible for small sample volumes. The ECIS technique outlined in Section 2.2.3 has shown success in numerous studies varying from cell proliferation and toxicity to cell migration and wound-healing [52]. However, this technique still requires the use of large external equipment. Additionally, the electrodes used in the system are exposed directly to the analyte and so

may be vulnerable to electrochemical effects in the long term. Another important consideration is the sensitivity of the measurements to additive noise since signals at the electrodes are routed to the measurement equipment through wires that may not be minimally short. The integrated lab-on-CMOS approaches, on the other hand, have the advantage of incorporating most of the sensing circuitry on chip along with the sensing electrodes. This helps in reducing the need for specialized equipment. Additionally, digitization can be performed on chip, helping to make the system more robust to noise. Continuous recording can also be achieved, creating a system for long-term label-free cell monitoring.

Here we develop an integrated CTF sensor that provides high-resolution measurements with on-chip digitization and a readout system that minimizes I/O requirements. The system provides unsupervised recording of measurements using only low-cost equipment ($< \$50$) and allows for high-throughput assays through the use of parallel devices. Within the possible capacitance sensing paradigms outlined in Section 2.2.4, the capacitance to frequency approach has numerous advantages. As discussed in Section 2.2.5, the transduction mechanism can inherently manage large variations in capacitance caused by changes in the permittivity of the cell media/environment. Additionally it offers simple data digitization with no additional circuitry required. A high capacitance resolution can be achieved, but at the cost of a long integration time (slow sampling rate). However for applications of cell sensing, a low sampling rate is adequate since timescales of interest are on the order of several minutes to hours. Therefore this work proposes to implement a CTF sensing approach to cell based capacitance sensing.

Chapter 3

Capacitance Sensor Design

3.1 Cell Capacitance Model

As introduced in Section 2.2.1, adherent cells modify the dielectric properties directly above the substrate interface. This creates a change in capacitive coupling that is then sensed through metal electrodes that are fabricated underneath the substrate on the CMOS IC. A schematic of the cell-substrate interface is shown in Fig. 3.1. While the cell media and cell itself are conductive, the effect of parasitic conductance/resistance is neglected because no current flow is expected. The passivation layer is assumed to be a very good insulating layer and so only capacitive effects are considered [53, 9].

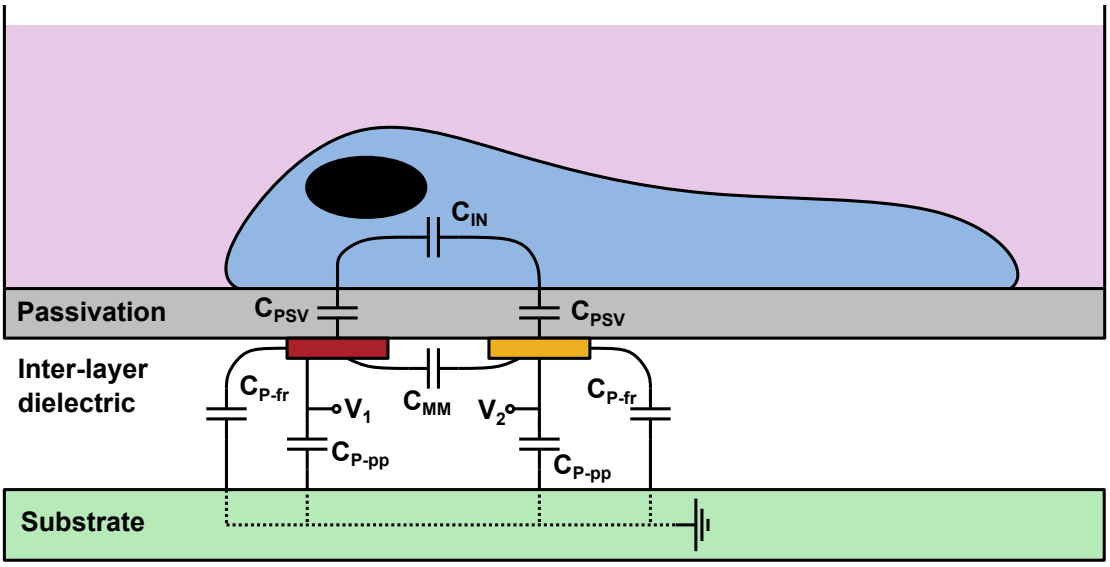

Figure 3.1: A model of the capacitances at the cell-substrate interface.

The CMOS IC consists of the silicon substrate, layers of dielectric (silicon dioxide) that separate the intermediary metal layers, and finally a passivation layer. The input electrodes are shown and labeled as nodes V_1 and V_2. These electrodes sense a net capacitance through the series combination of the passivation layer capacitance (C_{PSV}) and input capacitance (C_{IN}).

The passivation is the unmodified dielectric layer that comes from the CMOS foundry and generally consists of a stack of silicon dioxide and silicon nitride. Here we model this layer with as silicon nitride only, with a dielectric constant of 7.5. Per foundry parameters, the thickness of the passivation is 1.6 μm, giving an approximate capacitance area density of 42 aF/μm^2. The input capacitance, C_{IN}, is the sensed capacitance that couples through the fringing electric fields between the two input electrodes. As a first-order approximation, this input capacitance is modeled as a parallel plate capacitance. Given dielectric constants of 50 and 80 for cell cytoplasm and cell media, respectively, the capacitance area density of C_{IN} is expected to be 92 and 148 aF/μm^2, respectively. Since C_{PSV} and C_{IN} are on the same order of magnitude, they both contribute to the sensed capacitance that is detected through the CMOS sensor. Indeed, since they are in series with one another, one way to improve sensitivity to C_{IN} would be to decrease the passivation thickness or use a high-K dielectric.

An additional double-layer capacitance (C_{DL}) exists at the interface between the solid substrate and aqueous ionic cell media. However, the size of this capacitance is inversely proportional to the Debeye length which is on the order of several nanometers for cell media. This means the double-layer capacitance would be orders

of magnitudes larger than C_{PSV} and C_{IN}, and so can be ignored [54].

Further parasitics exist at the electrodes that give rise to a baseline offset capacitance. These include the electrode-substrate area (C_{P-pp}) and fringe (C_{P-fr}) capacitances, and the metal-metal coupling capacitance between the two electrodes through the inter-layer dielectric (C_{MM}). Based on foundry parameters, these parasitic capacitances are expected to be roughly 8 aF/μm^2, 31 aF/μm, and 74 aF/μm, for C_{P-pp}, C_{P-fr}, and C_{MM}, respectively. The net sensed capacitance between the two electrodes is given by:

$$C_{V1-V2} \cong \frac{C_{P-pp} + C_{P-fr}}{2} + C_{MM} + \frac{C_{PSV} C_{IN}}{C_{PSV} + 2C_{IN}} \tag{3.1}$$

This two-electrode model can be expanded to consider electrodes laid out in an interdigitated fashion, as is done on the designed CMOS sensor, and shown in Fig. 3.2.

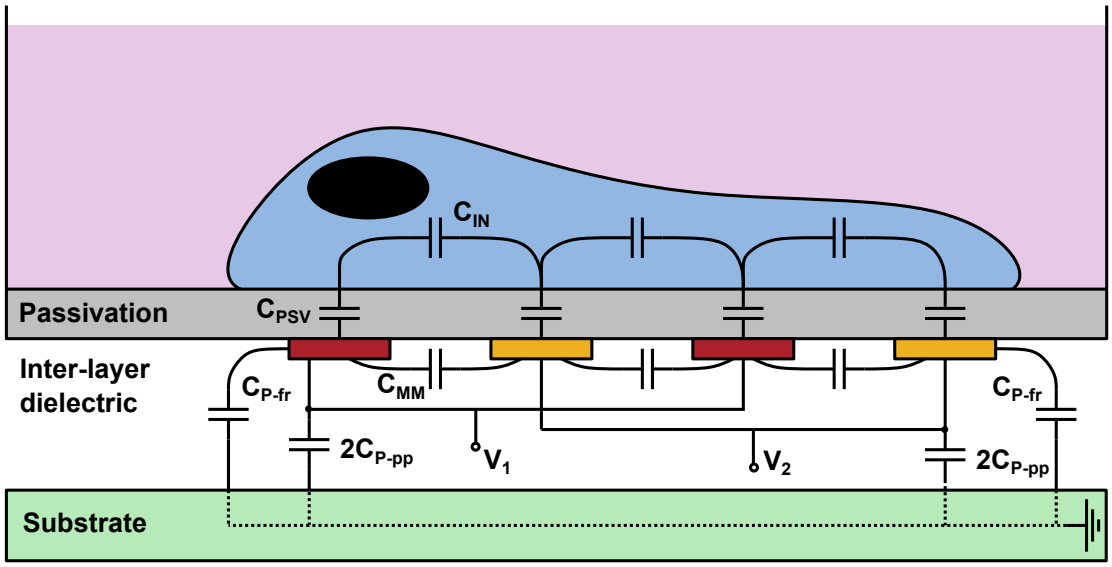

Figure 3.2: A model of the capacitances at the cell-substrate interface with interdigitated electrodes.

The sensed capacitance for this interdigitated case can be approximated by:

$$C_{V1-V2} \cong C_{P-pp} + \frac{C_{P-fr}}{2} + 3C_{MM} + \frac{3C_{PSV}C_{IN}}{C_{PSV} + 2C_{IN}} \tag{3.2}$$

As can be seen, there is a roughly 3× increase in the sensitivity to C_{IN}, althrough parasitic baseline capacitances are also increased. A plot of the sensed capacitance vs. relative permittivity is shown in Fig. 3.3a. A linear fit of the data points results in a slope of 12 aF/ϵ_r and offset of 10.6 fF at $\epsilon_r = 0$.

3.2 Multi-physics Simulations

To validate this model, the interdigitated electrode (four fingers) cross-section was created in an finite element method (FEM) multi-physics solver (COMSOL Multiphysics). Each finger of the electrodes was 4.2 μm wide and 23.1 μm long and spaced 4.8 μm apart. The thickness of the silicon, silicon dioxide, silicon nitride, and metal are 50, 4.06, 1.60, and 1.00 μm, respectively. The cell media was modeled as a large rectangular volume directly above the passivation layer with $\epsilon_r = 80$ and $\sigma = 1.5$ S/m. The cell was modeled as a 1 μm tall cylinder with a radius of 30 μm laying on top of the passivation layer above the electrodes ($\epsilon_r = 50$ and $\sigma = 0.2$ S/m). A plot of the effective capacitance across the electrodes as a function of the permittivity of the cell is shown in Fig. 3.3b. A linear fit of the data points results in a slope of 19 aF/ϵ_r and offset of 23.4 fF at $\epsilon_r = 0$.

As expected there is a larger parasitic capacitance component at the electrodes in the FEM results when compared to the analytical model. This is due to the

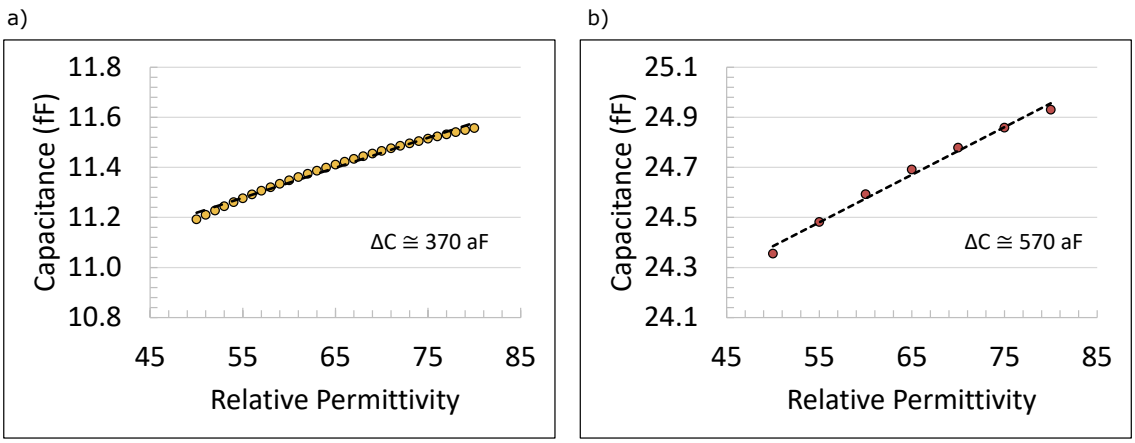

Figure 3.3: Sensed capacitance as a function of the relative permittivity of the environment over the input electrodes, for a) the analytical model, b) the FEM simulation.

simplistic parallel plate modeling of C_{IN} that ignores the fringing effects that will be the primary contributor in co-planar electrodes. The overall change in capacitance due to a cell binding event, where ϵ_r decreases from 80 to 50 is $\Delta C \cong 570$ aF and 370 aF for the FEM and analytical models, respectively. Thus the CMOS sensor must be able to resolve capacitance changes well below this threshold in order to reliably detect cell binding interactions.

3.3 Capacitive Sensing Approach

A custom CMOS capacitance sensor has been designed based on the capacitance-to-frequency transduction mechanism. The sensor and overall system was designed to have a large input dynamic range, provide unsupervised high resolution measurements, require a minimal number of I/O pins, and have a readout interface that requires only low cost components and allow for multiple devices.

3.4 Sensor Element

This section describes the individual sensor element that has been developed. Work related to the sensor was presented in two prior conference publications [55, 56], and journal paper [57].

3.4.1 Oscillator

The basic element in the capacitance-to-frequency transduction mechanism is the oscillating signal generator. There are numerous oscillator topologies that can be used, including LC tank, RC, and ring oscillators. These different structures have varied advantages and disadvantages. The ring oscillator topology was used for its simplicity, small size, and stability.

The basic sensor cell consists of a voltage-controlled oscillator (VCO) made of three stages [51, 55, 56, 57] and can be seen in Fig. 3.4a. It has two of its nodes connected to electrodes fabricated in the top-most metal layer. The capacitance sensed on these electrodes load the oscillator, causing changes in its charging and discharging rates, leading to a change in frequency at the output [55]. The parasitic load capacitances at each inverter stage in the oscillator ($C_{L1} - C_{L3}$) introduce finite switching delays ($\tau_1 - \tau_3$) and these contribute to the total delay period which sets the oscillation frequency of the sensor:

$$f = \frac{I_B}{V_{TH}(C_{L1} + C_{L2} + C_{L3})} \tag{3.3}$$

where V_{TH} is the MOSFET threshold voltage, and I_B is the bias current. The

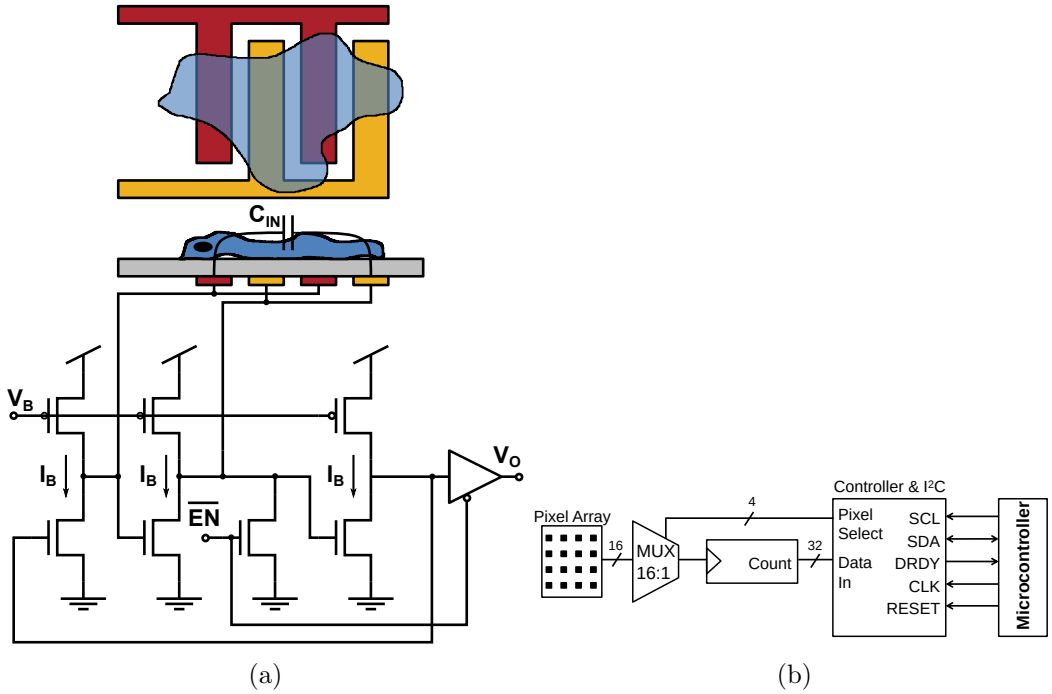

(a) (b)

Figure 3.4: a) Circuit diagram of capacitance sensor pixe, b) System block diagram

interdigitated sensing electrode contributes an input capacitance, C_{IN}, across one stage of the ring oscillator. During a switching transition, one side of the capacitor is charged to VDD while the other is discharged, increasing the effective capacitance across the inverter through the Miller effect. The delay period of this input stage can be written as [58]:

$$\tau_2 = \frac{V_{DD}}{I_B}(C_{L2} + 3C_{IN}) \tag{3.4}$$

This means a hyperbolic change in frequency is expected as the input capacitance changes. However, under the expected operating conditions and expected small variations in sensed capacitance, the capacitance-frequency relationship can be approximated as linear, which is discussed in the following sections. On the fabricated sensor, the NMOS transistors making up the oscillators are sized with a width-to-length ratio of 2.8/0.7 μm.

3.4.2 Simulation Performance

3.4.2.1 Capacitance Sensitivity

Fig. 3.5 shows simulation results of how the output oscillator frequency varies as a function of sensed capacitive load. As expected from analytical equations, the oscillation frequency decreases as the sensed capacitive load increases. The expected range of capacitance load values based on an FEM solver model was 2 fF with a baseline of approximately 10 or 20 fF, depending on the model. Within this range, the output frequency varies quite linearly, with an R^2 value of 0.9985 and a slope of 1.22 MHz/fF.

Ring oscillators exhibit variations in their outputs due to noise sources such as flicker and white noise [59]. The jitter due to this resulting phase noise must be considered because it may affect the final output count. Simulations incorporating flicker and white noise showed an approximately 24 μs accumulation of jitter over the 1 s of collection time. Given the sensitivity of 1.22 MHz/fF at an oscillation frequency of 56.6 MHz, the minimum resolution limited by phase noise comes to 1.1 aF. This figure is an improvement over previous designs, but is based upon expected sensitivity obtained from simulations.

Monte Carlo simulations of mismatch variations were performed to see their effects on the oscillation frequency. Fig. 3.5 shows results for a range of sensing capacitances. The standard deviation in oscillation frequency at a sensed capacitance of 10 fF is 759 kHz. This leads to an expected uncertainty of 1.8 fF in measurements due to mismatch. This mismatch is greater than many cell-related capacitances of

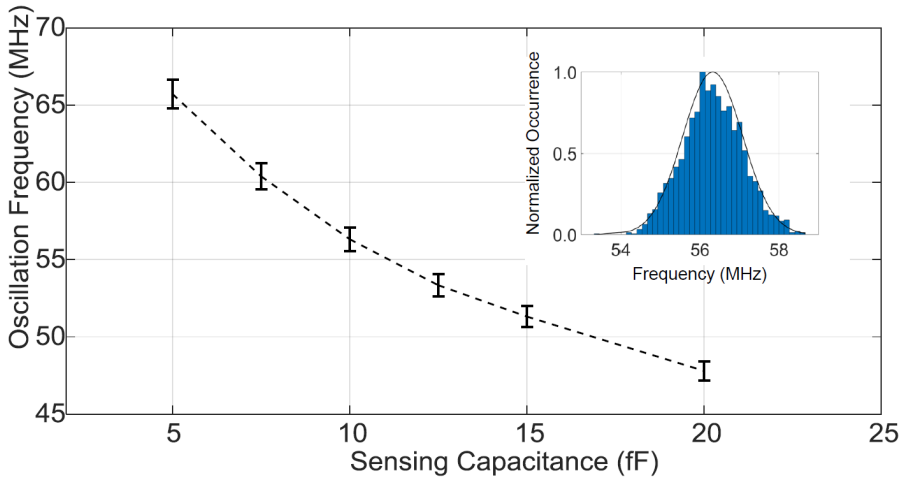

Figure 3.5: Output frequency as a function of sensed capacitive load. Results for typical expected capacitances are shown in red. The dotted line shows Monte Carlo simulation results with the inset showing a histogram for a sensed capacitance of 10 fF.

interest, so the system will require per-pixel calibration so that it can retain sensitivity to cellular phenomena. Fortunately, in this counter-based design, saturation and dynamic range are not issues, so the calibration will be implemented in post-readout digital signal processing.

3.4.2.2 Temperature Sensitivity

A series of temperature sensors were implemented on chip in addition to capacitance sensor elements. In order to simplify the overall system, the temperature sensors were designed as additional pixels in the chip using the same base ring oscillator. Instead of a fixed reference current, a bandgap reference circuit is used to bias the ring oscillator with a current that is proportional to absolute temperature [60].

Fig. 3.6 shows how temperature affects the simulated output frequency of both the capacitance and temperature sensors. The temperature range of interest

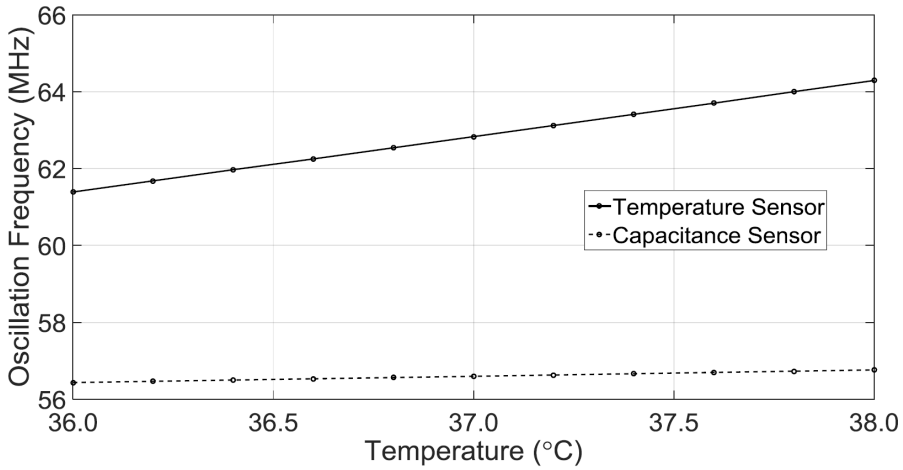

Figure 3.6: Output frequency for the temperature and capacitance sensors as a function of temperature.

is from 36 to 40 $°C$, since the experiments will be done in a temperature-controlled incubator. The output frequency of the temperature sensor responds linearly to changes in temperature, with an R^2 value of 1.00 and a slope of 1.47 MHz/$°C$. The capacitance sensor is also affected by ambient temperature, and this relationship is also linear, with an R^2 value of 1.00 and a slope of 160 kHz/$°C$. These linear relationships allow for pixel-level calibration before experiments for correcting the output data.

3.5 System Overview

The lab-on-CMOS chip contains an array of 4×4 sensor elements. In order to facilitate the required automatic data readout without the use of large and expensive laboratory equipment, a serial readout bus is implemented. The system is designed to allow for simple implementation and ease of experimentation. It only requires a microcontroller and computer for data readout and storage. Fig. 3.4b shows a

block diagram of the system. Each of the 4×4 sensor pixels generates an oscillating signal. This is passed through a digital buffer and into a multiplexer which then connects to a 32 bit counter. The counter integrates the oscillating signal for a specified time. Once the integration time is reached, the final count value is stored and then sent off-chip via an I^2C interface implemented on chip. Details of the logic can be found in Section A.1. In addition to the capacitance sensor pixels in the sensing array, two additional sensors are also included on chip placed within the outer padframe area of the chip. This isolates them away from the wet environment during experimentation and allows them to be used as reference pixels, as described in Section 3.10.

3.5.1 Multiplexer and Counter

The output signals from each pixel are buffered to a standard digital multiplexer, and the selected signal is fed to a single shared counter, which reduces the total circuit area. The individual pixels are read out sequentially. The minimum achievable sensor resolution (Δf_{min}) is inversely proportional to the collection time (T_c):

$$\Delta f_{min} = \frac{Q_{min}}{T_c} \tag{3.5}$$

where Q_{min} is the desired minimum difference in count value. Therefore, one can trade sensor speed for resolution. For typical operation the sensitivity of the sensor is 1.22 MHz/fF, or 12.2 kHz/10 aF (Fig. 3.5). Given a target resolution of 10 aF and an arbitrary desired minimum difference in count value of 100, the required

integration time is 8.2 ms. In reality, however, parasitic capacitances [50] reduce sensitivity [9]. To address this, the integration time T_c in the final system design is set to be >1 s, providing a safety margin of two orders of magnitude for the measurement range of interest. This collection time is set using a timing clock that is generated by frequency dividing the system clock (f_{clk}). Divisions are in factors of 2 and so the maximum timing clock frequency that satisfies the integration time requirement is $f_{clk}/2^{22} = 0.72$ Hz, which means $T_c = 1.40$ s.

The minimum counter size (N_c) required to avoid saturation of the sensor signal is a function of the oscillation frequency and counting time:

$$N_c = ceil(log_2(fT_c) \tag{3.6}$$

where f is the sensors oscillation frequency. Given a frequency of 56.6 MHz and collection time of 1 s, the minimum counter size is 26 bits. The I^2C serial readout protocol used in this system has packet sizes of 8 bits, so a 26 bit data transfer requires 4 packets, where the last byte is zero-padded. Therefore, a 32 bit counter is used in this design. The added space and power costs due to this increase are minimal. Additionally, the larger counter, having a maximum T_c of 75 s, allows for more flexibility in varying the collection time and leads to a minimum theoretical resolution of 0.06 aF. In reality, phase noise would limit resolution to a higher floor.

3.5.2 Serial Readout

Each sensor pixel generates a 32 bit data sample. The most direct method of reading out the samples is to output each bit to an I/O pad. However this results in 32 bond pads that must be dedicated for readout, which may not be feasible in real fabrication. Additionally, a large number of I/O pins introduces packaging difficulties, especially in cell culture monitoring for which passivation of the electrical leads is crucial. An alternative method is to read subsections of the 32 bits at a time. For example, if one byte of data is read out at a time, the number of bond pads required for readout would be 10 (eight bit lines and two byte select lines). To minimize the I/O requirements further, we implement an I^2C serial readout bus.

I^2C is a serial bus data transfer protocol designed for communication between multiple sensor chips. It implements a two-wire bus with support for up to 128 individual peripheral chips. The I^2C communication interface was implemented by modifying an open-source I^2C core [61] written in Verilog HDL. The core code was modified to implement only read commands with a packet size of 4 bytes. A separate logic controller was created to interface with the I^2C block. This logic controller implements the sequential reading and data transfer phases of the system. The oscillator in each pixel is turned on, and the signal is fed into the shared counter. Once the required counting time has been reached, the value is latched and sent to the I^2C controller for transmission off-chip. The oscillator start-up time may vary between pixels, so a delay stage has been implemented to allow the oscillator to start up before the counter starts accumulating. Another consideration is the finite

rise and fall times of switching bits in the counter, which introduce brief (< 100 ps) periods of time when the count is unstable and should not be latched. In this implementation, latching only occurs after a negative edge of the oscillator clock, since the counter is positive-edge triggered. The digital I^2C and chip controller logic were synthesized using an RTL compiler. A floorplan layout was then created using Place & Route software and merged with the manually drawn pixel array.

3.6 Fabricated Chip & Readout Platform

The 4×4 array of pixels (shown in Fig. 3.7) were arranged with an X and Y pitch of 196 μm and 186 μm, respectively, covering an area of 618×588 μm^2 on a 3×3 mm^2 chip. Since the electrodes are 30×30 μm^2 in size and are sensitive to permittivity changes in their immediate surroundings, the actual sensing area covered by the electrodes is roughly 120×120 μm^2. This means that the spatial resolution of the sensor is relatively low. However, when looking at the mechanics of the cell population as a whole, discrete measurement sites spread over a large area can suffice. A higher pixel density would be ideal for performing studies of individual cells. Eight I/O pads are used which were duplicated for packaging redundancy.

The readout system used in this work is a commercially available microcontroller (MicroPython PYB v1.0), although any device capable of I^2C communication can be used. All bias voltages are generated internally (Section A.1) and the supply voltage of 3.3 V is provided by the microcontroller directly. The finite ramping time of the power supply and startup circuits built into the bias generator ensure the

oscillators start up correctly. The microcontroller additionally supplies the digital clock signal that is used for timing of the controller logic on chip and the I^2C bus. Therefore no additional equipment besides the sensor, microcontroller, and a battery are required to perform measurements, allowing for experiments to be done easily outside of the laboratory setting. The average power consumption for the entire system was measured to be 300 mW with the IC chip consuming 8 mW. Therefore the complete lab-on-CMOS system can easily be implemented on a portable platform. In fact, a low power microcontroller can be used in order to extend battery lifetime to several days to facilitate longer term experiments.

The presented sensor was fabricated in a commercially available 0.35 μm CMOS process and wirebonded to a standard DIP-40 ceramic carrier for dry benchtop experiments. For wet experiments, the wirebonds were passivated using a high electrical resistivity epoxy (Durapot 863, Cotronics). The passivation was performed by first heating the chip-in-carrier to 120 °C and then manually applying the epoxy

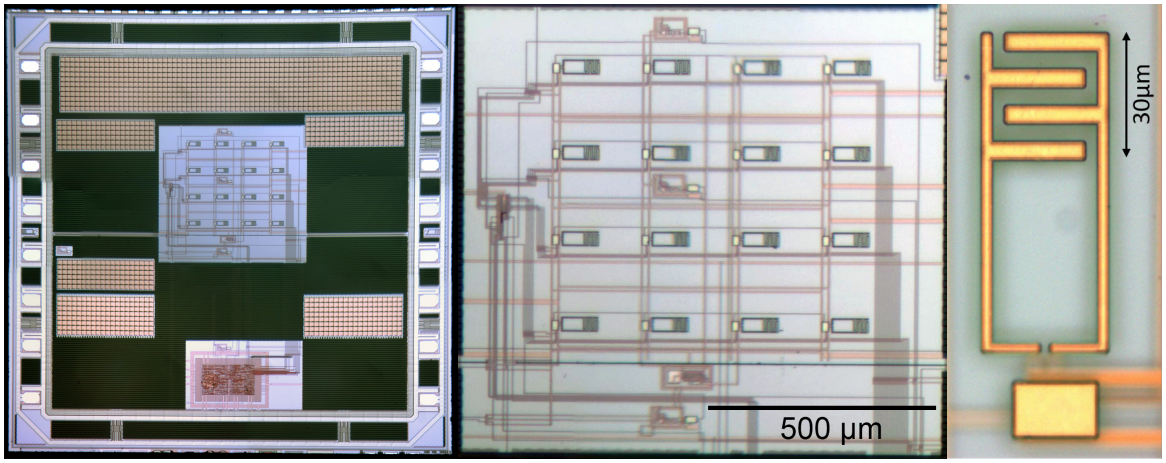

(a) (b) (c)

Figure 3.7: Photomicrograph of a) Fabricated die (3×3 mm^2), b) sensing array, and c) sensing electrodes (30×30 μm^2).

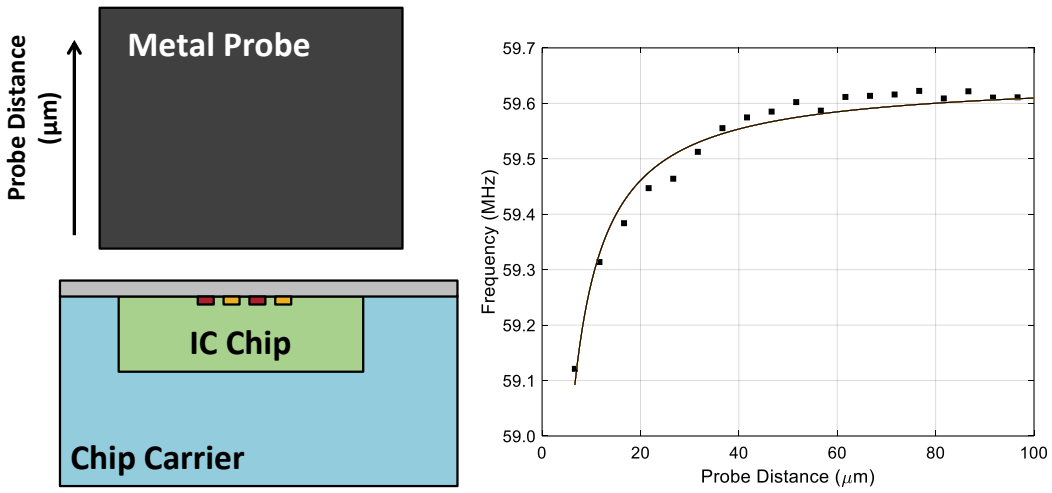

(a) (b)

Figure 3.8: a) Exeprimental setup to characterize sensor as a distance sensor. b) Sensor output frequency as a metal probe is moved away from the surface of the chip. Solid line shows a regressive fit of the measured data.

over the bond wires and onto the chip surface, leaving only the sensing area uncovered.

3.7 Capacitance Computation

The sensor data was calibrated by placing a metal probe close to the surface of the chip and varying the vertical distance of the probe relative to the chip (Fig. 3.8a). The position of the probe was controlled automatically using a piezoelectric actuation platform. The probe was moved in steps of 5 ± 0.5 μm, and the sensor outputs were allowed to settle for 10 minutes between movements. These experiments were performed with Sheung Lu. Fig. 3.8b shows how the measured frequency of oscillation varies as the metal probe is moved away from the chip surface. The output frequency increases as a function of probe distance, corresponding to a decrease in capacitance.

This setup was simulated in a FEM solver to obtain the capacitive loads induced by the probe positions. For the small operating range of interest (less than 2 fF) in cell sensing applications, the sensor output frequency response, $f(C_{IN})$, can be modeled linearly as follows:

$$f(C_{IN}) = -\alpha(C_{IN} + C_0) + f_0 \tag{3.7}$$

where C_{IN} is input capacitance, C_0 is the total parasitic and offset capacitances at the circuit level, f_0 is a baseline frequency, and α is the sensor's sensitivity. The capacitive load measured due to the metal probe is then modeled using an inversely proportional relationship:

$$C_{IN}(x) = \frac{\beta}{x + x'} \tag{3.8}$$

where β is a scaling parameter that relates sensed capacitance to probe distance, and x' is a parameter that accounts for any displacement errors introduced by the piezoelectric actuators. We then obtain a model of the sensor's output frequency as a function of probe distance:

$$f(x) = -\alpha(\frac{\beta}{x + x'} + C_0) + f_0 \tag{3.9}$$

The parasitic capacitances in this model were estimated to be 12.1 fF by simulating the electrode and probe structure in an FEM solver (COMSOL Multiphysics). A regressive fit was performed on the data and the resulting curve is shown in Fig. 3.8 (solid line). The sensor output can thus be characterized by generating calibra-

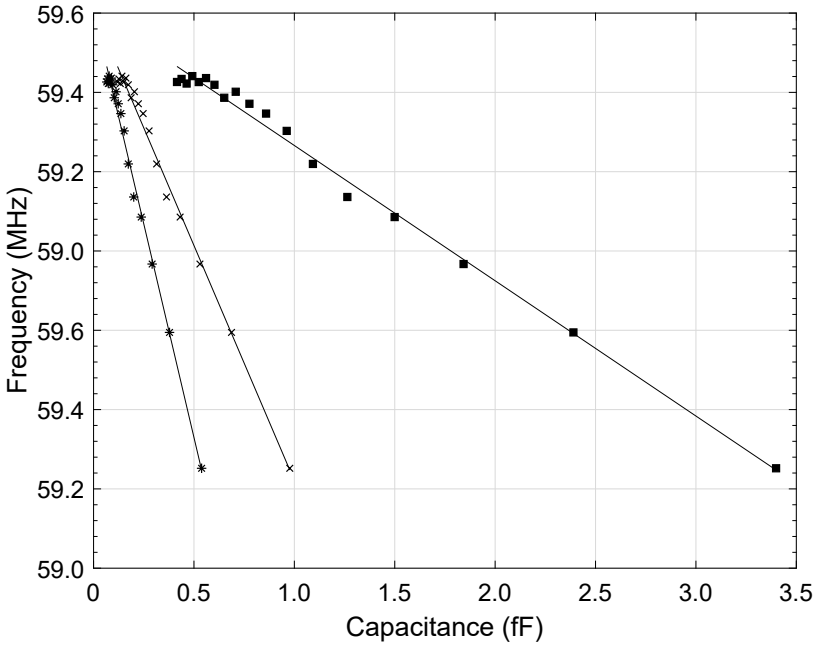

Figure 3.9: Sensor characterization curves generated by mapping electrode probe distance to modeled capacitance value. The curves from left to right indicate the best, average, and worst case sensitivity scenarios.

tion curves using this relationship. Fig. 3.9 shows three curves corresponding to the best, average, and worst sensitivity. The capacitance sensitivities corresponding to each scenario are 1077, 593, and 171 kHz/fF. respectively. These curves were obtained by using the smallest, largest, and average β values obtained from a set of 1000 regressive fits. The sensitivity figure $\alpha = 593$ kHz/fF, is the measure that is used in subsequent capacitance calculations.

3.8 Bench-Top Characterization

3.8.1 Response to Organic Solvents

The packaged chip was evaluated by measuring the response to fluids placed in the sample well. We selected fluids with a range of dielectric constants in order to induce changes in permittivity of the environment surrounding the chip, causing changes in signal output. The fluids were deionized (DI) water ($\epsilon_r = 80.1$), acetone ($\epsilon_r = 20.7$), and isopropyl alcohol (IPA) ($\epsilon_r = 17.9$) [62].

Cell media was also used. Fig. 3.10a shows data from a representative pixel that illustrates the application and removal of each fluid over time. Fluids with higher relative permittivity induce a stronger drop in amplitude from the baseline (air, $\epsilon_r = 1.0$) since they correspond to a larger sensed capacitance. Of the tested solutions, DI water has the highest relative permittivity and causes a change in capacitance of 12 fF from the baseline, based on FEM simulations. Therefore the input range of the sensor as tested in this work is 12 fF. The sharp features seen in Fig. 3.10a are artifacts related to physical movements in the experiment. This is especially the case with acetone since its relatively high vapor pressure means constant fluid replenishment is needed if the package is not sealed. Fig. 3.10b shows the mean sensor output across all 16 pixels with error bars marking standard deviations, and Fig. 3.10c shows the response as a function of relative dielectric permittivity.

The capacitance sensor chip was also exposed to varying concentrations of IPA diluted in DI water. The bottom panel of Fig. 3.11 shows the sensor out-

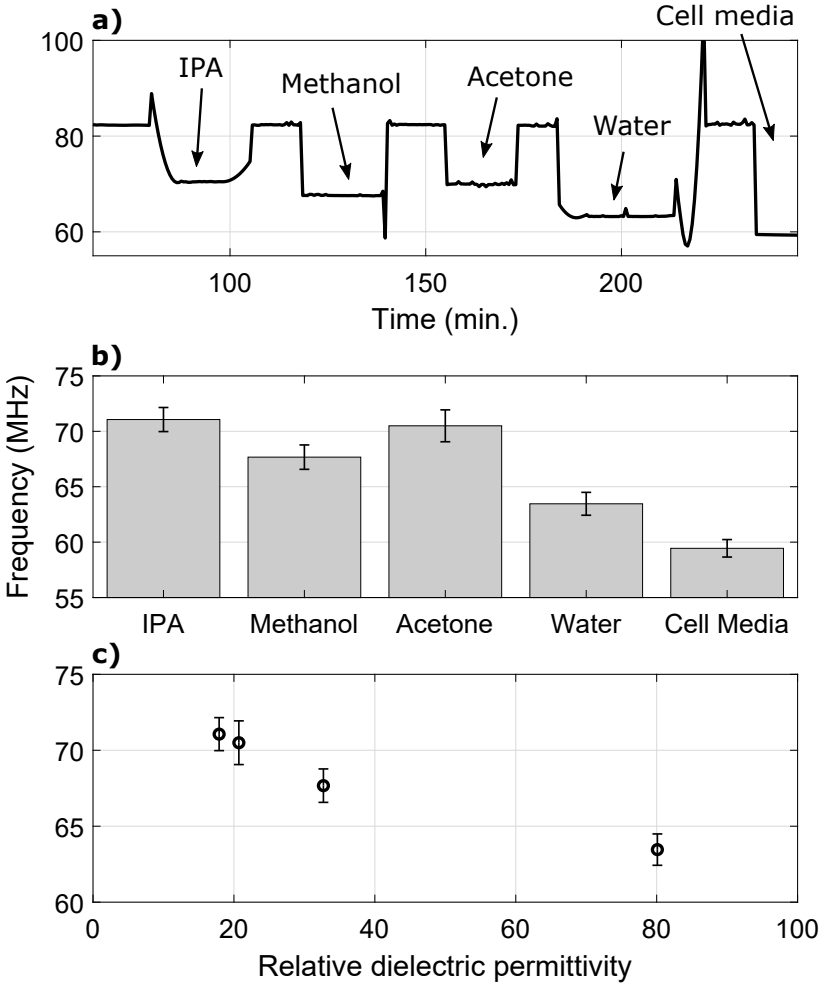

Figure 3.10: Sensor response to addition of different fluids. (a) Transient plot of response for a single pixel. (b) Mean response and standard deviation across 16 pixels. (c) Mean response as a function of relative dielectric permittivity.

put frequency, averaged across 15 pixels; data from one channel was discarded due to readout error. As can be seen the sensor frequency response decreases as the percentage by volume of IPA is decreased.

3.8.2 Spatial Correlation of Capacitance Sensors

The sensor chip contains an array of 16 capacitance pixels, distributed into four rows and four columns. Following the experimental protocol outlined in Section 3.7, it is possible to create a map of responses over time by matching each pixel with its physical location. Fig. 3.12 shows an experiment where the metal probe was brought down onto the sensor surface and then lifted off. For this particular run, the probe was purposefully aligned off-center from the sensor array. The change in frequency (δf) from the baseline measurement is plotted for all 16 pixels. The bottom panel shows a map of the 16 responses at four different time points, marked by the blue dashed line in the top panel. Each grid square corresponds to a pixel's physical location on the chip. The probe begins to touch down at 190 min and lifts off at 290 min. The bottom panel shows that the change in frequency is more prominent in the right side and upper-right side pixels. As the probe lifts off, the

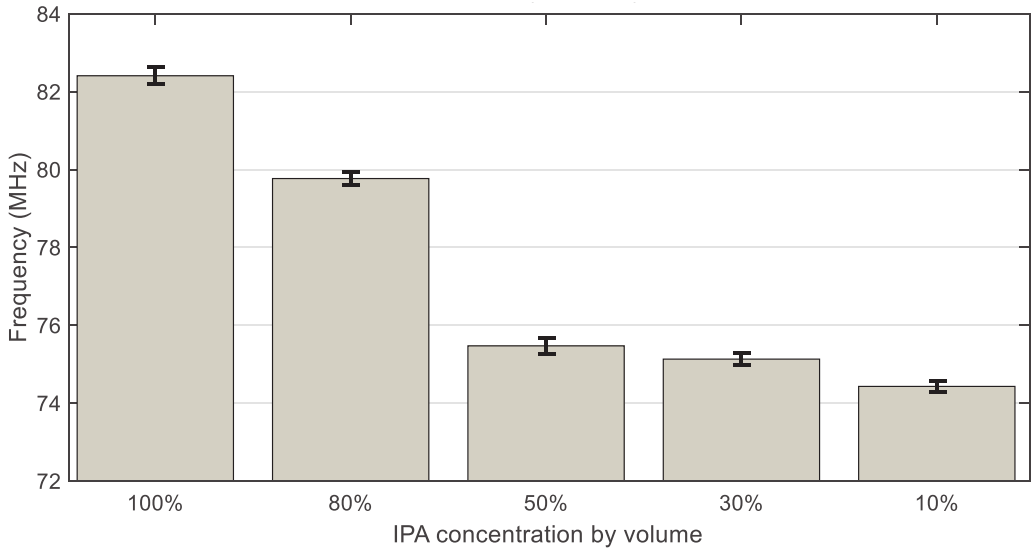

Figure 3.11: Sensor response due to application of difference concentrations of isopropyl alcohol.

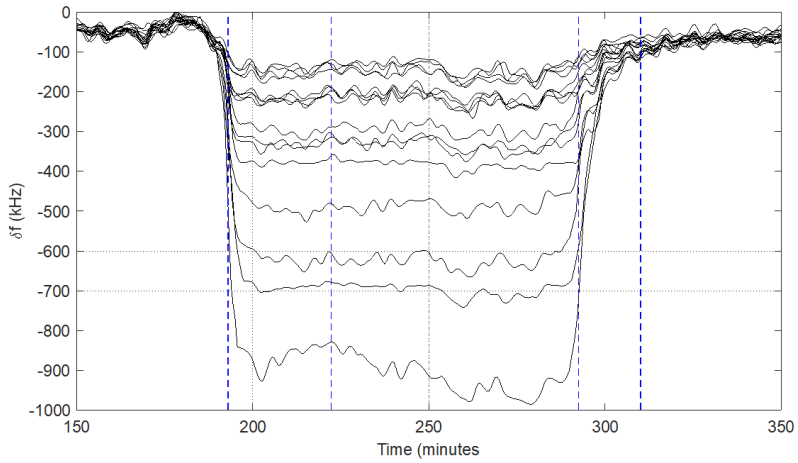

(a)

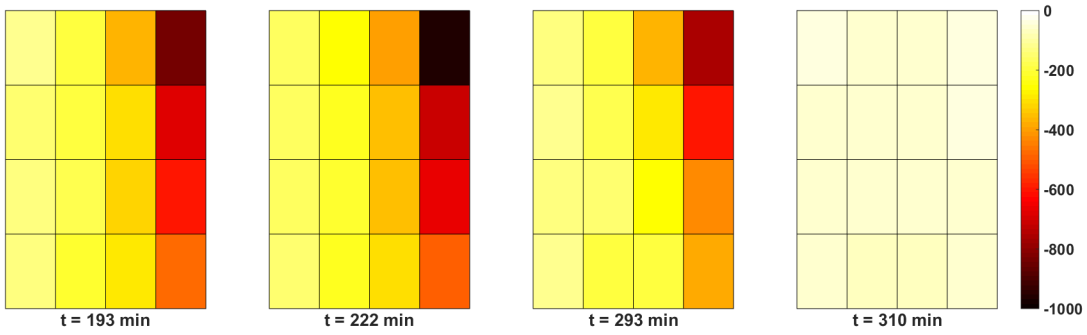

(b)

Figure 3.12: Mapping sensor response to external probe interacting with chip surface. a) 16 pixel responses plotted over time as the probe is brought down and lifted off. b) Shaded plot mapping responses to physical pixel locations. Each array image corresponds to time points indicated by the dashed lines in (a).

pixels gradually decrease in their response, with the top-right pixel being the last to settle. This is consistent with the initial alignment of the metal probe in this experiment.

3.9 System Level Improvements

3.9.1 Parallel Readout

In the 2nd generation of the chip, the architecture was improved to perform parallel readout. The chip maintained a 4×4 array, with multiple sensors activated at the same time, in a column-wise format. Four row units, each consisting of a multiplexer and counter, were used to integrate a column of sensors at one time. Each communication cycle on the I^2C readout bus would then send 4×32 bits of data. Fig. 3.13a shows a block diagram of the system with a column-wise readout. This version allows for a $4\times$ improvement in sensor speed allows the IC to be used for shorter-term cell experiments while maintaining the same high resolution required for detection of cell binding events. A die photo of the fabricated chip is shown in Fig. 3.13b.

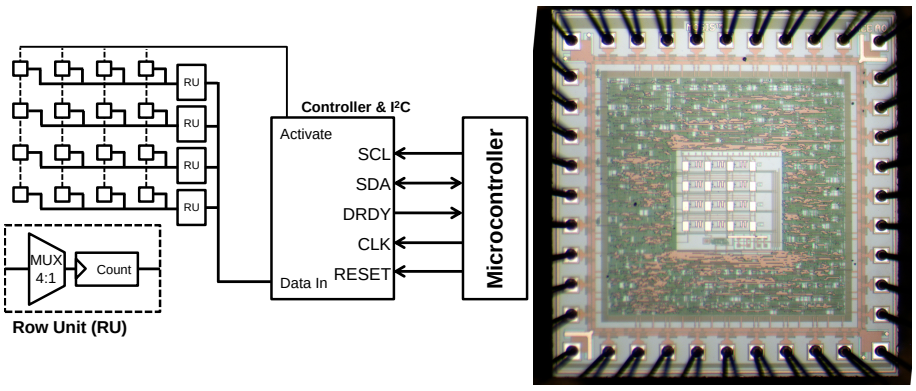

(a) (b)

Figure 3.13: a) Expanded system to include column-wise readout. b) Die photo of the 2nd generation chip

3.9.2 Tunable Integration Time & Active Pixel Selections

The resolution of the sensor is directly related to the integration time, as discussed in Section 3.5.1. In the generation 1 fabricated chip, the integration time was set to 1.39 seconds ($1/(f_{clk}/2^{22}), f_{clk} = 3$ MHz) per pixel, which means 22.2 seconds are required to read 16 pixels. This is a relatively slow sampling rate, but while it is adequate for cell experiments with long time constants, a faster sampling rate would help to capture minute differences that would otherwise be lost. The most direct way to increase sampling rate is to reduce the integration time at the cost of reduced resolution.

To this end we look at the noise resolution of the device. The sensor was run under stable operating conditions (sensor surface covered, dark light conditions) over a period of several hours. The mean standard deviation of the output frequency across all channels was computed to be 22.3 kHz which means a noise floor of 37.6 aF (given the measured sensitivity of 593 kH/fF). For an integration time of 1.39 s, the 22.3 kHz noise level means that a value of $\sim 62 \times 10^3$ of the integrated sensor count output can be considered within the noise floor, that is the effective number of bits (ENOB) is 16.1. Thus, by reducing the integration time, the ENOB can be increased. At the extreme, an integration time of $\sim 22.4\ \mu s$ would reduce the noise value to ~ 1.

With this in mind, a 3rd generation chip was designed and fabricated. The chip is designed with a programmable integration time from 20 ms to 5.6 s, in 20 ms increments. This parameter is programmed through the I^2C bus and does not

require any additional wiring requirements. This version of the chip also implements programmable sensors to activate and deactivate sensors in the array individually. This spatial readout selection allows the sensing area of the array to be fine-tuned for certain applications. For example, if global capacitance variations are expected such as during cell death and detachment due to application of a toxin, the number of active pixels can be minimized in order to increase sensor sampling rate. An increase in sampling rate of 32x is achievable if only a single sensor is required for readout. A block diagram and die photo of this 3rd generation chip is shown in Fig. 3.14.

Finally, another aim is to enable high throughput bioassay experiments by allowing multiple devices to run in parallel without the need for additional equipment. This could prove to be useful in certain applications, and help to make this lab-on-CMOS system a more practical tool for biological assays.

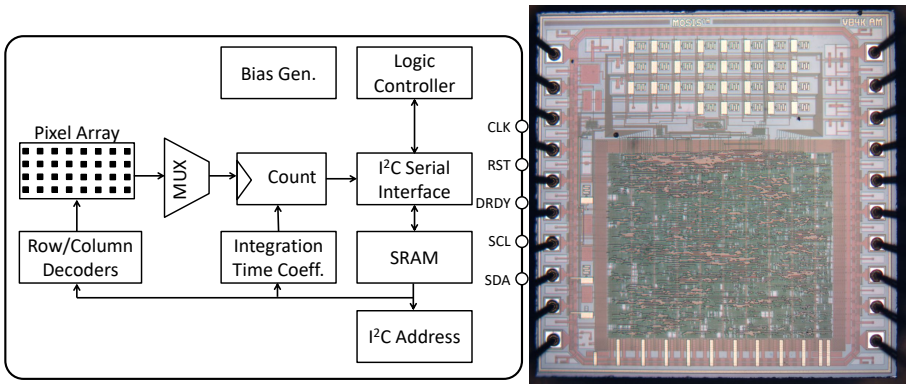

Figure 3.14: a) System block diagram of chip with programmable integration time, pixel activation and programmable I^2C address. b) Die photo of the 3rd generation chip

3.10 Sensor Calibration

Pixel-to-pixel variations in the output frequency are expected due to process variations and parasitics inherited from fabrication. This can result in each of the sensor pixels having slightly different baseline frequency levels from one another. Additionally, fluctuations in power supply levels and temperature may affect the pixel output frequencies. Therefore, measurements are computed with respect to an on-chip reference pixel that is also exposed to global supply and temperature variations, but is unaffected by the analytes being detected. This provides a pseudo-differential measurement as given by the following:

$$\Delta C_N(t) = \alpha([f_N(t) - f_N(0)] - \lambda[f_{Ref}(t) - f_{Ref}(0)]) \tag{3.10}$$

where $f_N(t)$ is the raw data for channel N, $f_{Ref}(t)$ is the data for the reference channel, and $\Delta C_N(t)$ is the final computed capacitance value. The parameter is the frequency-to-capacitance sensitivity factor (590 kHz/fF) obtained experimentally in Section 3.7, [56]. The parameter λ is a calibration coefficient that can either be fixed for all channels ($\lambda = 1$), performing a global calibration, or be set individually for each pixel ($\lambda = \gamma_N/\gamma_{Ref}$). Coefficients γ_N and γ_{Ref} are the slopes of linear fit lines for $f_N(t)$ and $f_{Ref}(t)$, respectively.

3.10.1 Temperature Sensitivity

The temperature sensitivity of the device was analyzed by pipetting a drop of cell media onto the sensor array and placing the packaged device in a hot plate

oven at 44 °C. Measurements were started and the oven was turned off to allow it to cool down to 33 °C over a period of 80 minutes. The mean output frequency of the pixels is shown in the top panel of Fig. 3.15 (black circles). The temperature-response of the device is approximately linear ($R^2 = 0.99$) with a sensitivity of 80.6 kHz/°C or 1374 ppm/°C. After calibration using the reference pixels as described previously with $\lambda = 1$, the sensitivity is reduced to 10.1 kHz/°C or 172 ppm/°C. The resulting data points are shown as red diamond markers. Per-pixel calibration was also performed by computing the γ_N coefficients for each channel. This results in diminishing temperature sensitivity down to mean across channels of 0.0 kHz/°C. The data points for this case are shown as the yellow square markers. It should be noted that in cell culture experiments, the growth environment has to be strictly controlled and so the ambient sensor temperature is expected to remain stable at 37 °C throughout the duration of an experiment.

3.10.2 Power Supply Sensitivity

Portable biosensor applications can be prone to power supply fluctuations and so we analyze the power supply sensitivity of the device. The chip was powered using an external DC power supply (SourceMeter 2400, Keithley) and the supply was swept from 3.0 to 3.3 V in 10 mV increments. The mean output frequency of the pixels is shown in the bottom panel of Fig. 3.15 (black circles). The response of the device is approximately linear ($R^2 = 0.97$) with a sensitivity of 797 kHz/V. After global calibration, the sensitivity is reduced to 58 kHz/V (red square markers).

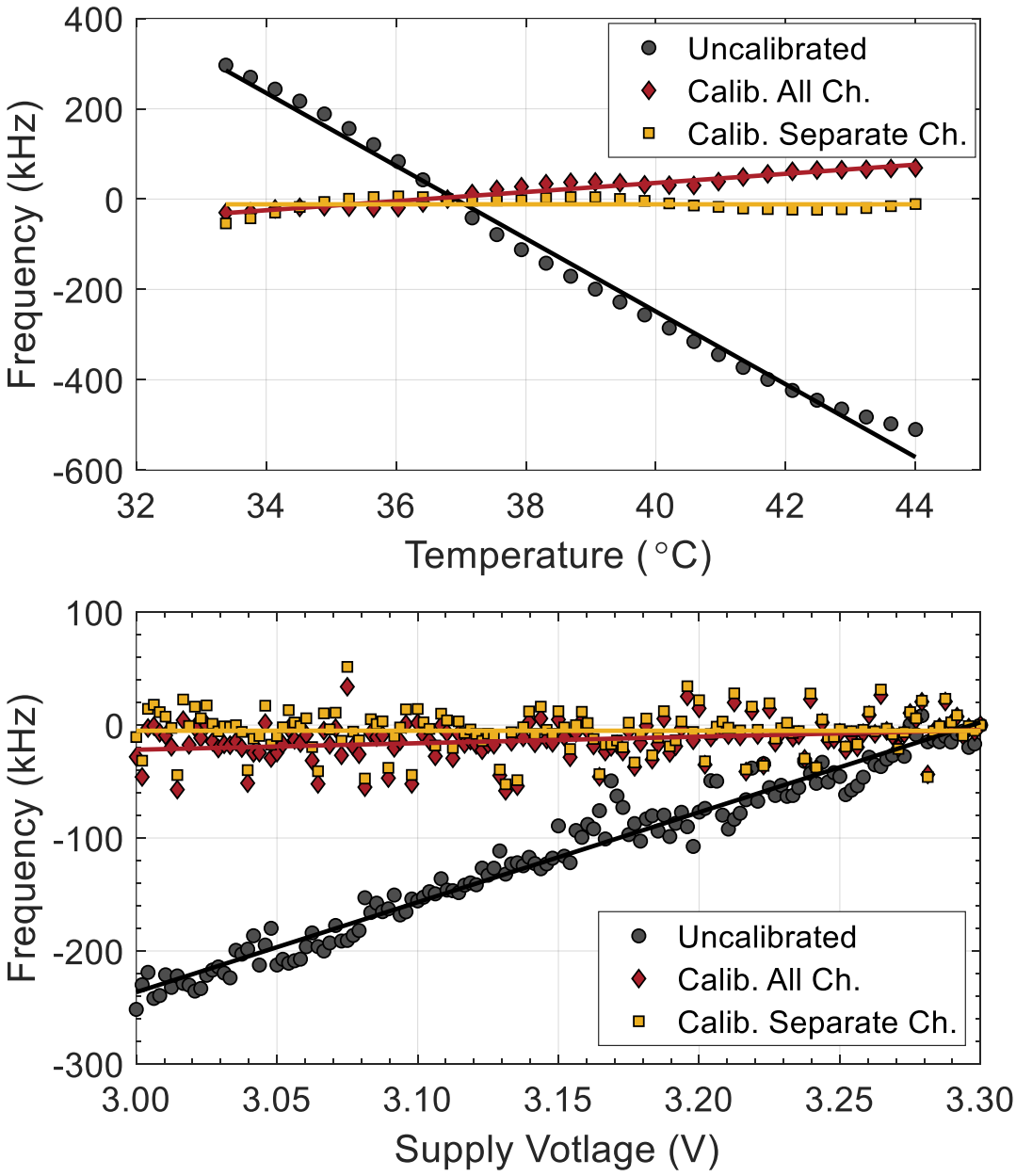

Figure 3.15: Sensitivity and compensation for temperature (top) and power supply (bottom)

Finally, the single pixel calibration was seen to reduce sensitivity down to 0.0 kHz/V (yellow square markers).

3.10.3 Noise

Ring oscillators are subject to flicker, thermal, and white noise that result in phase noise and timing jitter [59, 63]. These effects are manifested as fluctuations in the oscillators' output frequencies. In order to quantify noise and resolution of the sensor elements, we performed benchtop experiments under cell culture conditions.

A standard microbiology tube (1.5 mL, Eppendorf Flex-Tube) was cut and glued onto the packaged chip to form a well. Cell culture media was put into the well and the device was placed in an incubator at 37 °C for 15 hours while sensor data was being recorded. The pixels oscillate with baseline frequencies ranging between 58.0 and 60.5 MHz. Global calibration was performed ($\lambda = 1$) as described in Section 3.10. A plot of the resulting data is shown in Fig. 3.16a. The gray traces are signals for each pixel while the black line shows their mean. Fig. 3.16b. shows a histogram of the mean output. The mean standard deviation of frequency over all pixels is 9.3 kHz, which corresponds to a dynamic capacitance variation of 16 aF.

It should be noted that while pixel level calibration reduces temperature and power supply sensitivity, it requires computation of calibration coefficients. Therefore for simplicity, the *in vitro* experimental data presented in this work uses global calibration ($\lambda = 1$). As such, sensor measurements are expected to exhibit noise contributions from random temperature and power supply fluctuations. However, the extent of the noise contributions is expected to fall within the measured noise resolution of 16 aF. For example, since experiments are done in a regulated incubator, temperature stability is expected to be within ±0.2 °C [64] which corresponds

to ±3.4 aF given a 17 aF/°C sensitivity. Additionally, the chip is powered from a voltage regulator on the microcontroller board, with a dropout voltage of < 50 mV at a 2.5 mA load current [65]. This corresponds to variability of roughly ±5 aF given a 98 aF/V sensitivity.

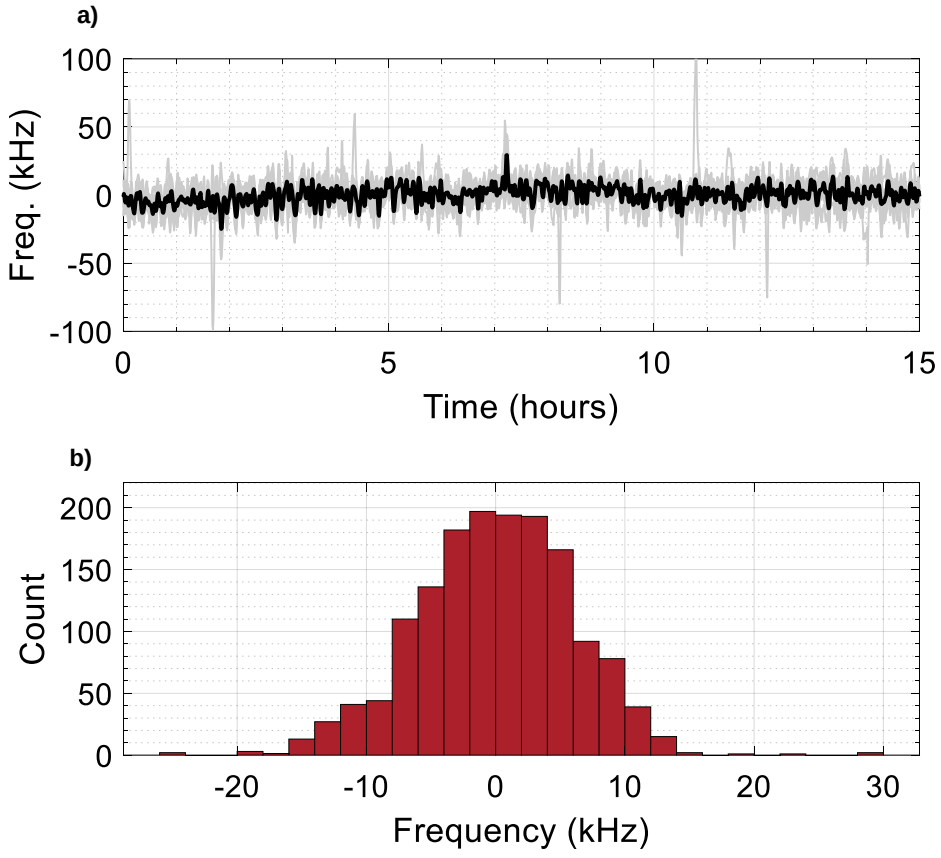

Figure 3.16: Long-term sensor response and noise when exposed to cell media at 37 °C. a) Output frequency vs. time for each pixel (gray) and their mean (black). b) Histogram of the mean frequency.

Chapter 4

Tracking Cell Metrics

4.1 Introduction

This chapter presents results of *in vitro* experiments testing the capacitance sensor chip with live cells. The experimental protocol is described, along with discussion of encapsulating the chip in biocompatible materials. Experimental results are then presented with preliminary ground-truth validation using standard microscopy. Finally the sensor data is used to corroborate with actual cell mechanics by generating quantification metrics to monitor cell adhesion, proliferation, and mitotis.

4.2 Device Packaging

The presented sensor was fabricated in a commercially available 0.35 μm CMOS process Three different packaging methods were used. The first method involved gluing the dies to a ceramic carrier, wirebonding to form electrical connections, and passivating using an epoxy, as described in Section 3.6. The second method involved encapsulating the die in an epoxy mold, patterning a zinc/copper/nickel metal stack to make electrical contacts with the chip, and finally passivating the electrical traces using a second layer of epoxy [66]. Cross-sectional schematics of these two packaging methods are shown in 4.1. The third method involved mounting the chip to a low-temperature co-fired ceramic (LTCC) carrier by using Au-Au

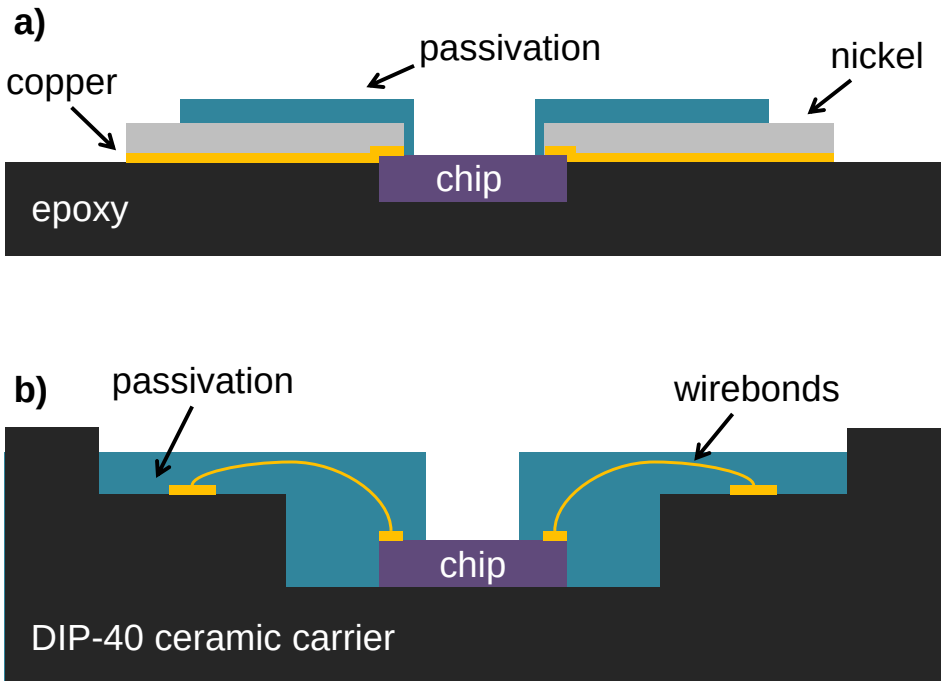

Figure 4.1: Cross-sectional views of chips packaged in a) an epoxy handle wafer, and b) a passivated DIP carrier

thermocompression bonding. Under-filling with epoxy was used to create a liquid tight seal between the sensor chip and the LTCC carrier [67, 68]. For all packaging methods, cell culture wells were created by gluing either standard microbiology or polypropylene tubes around the sensing area. No variation in chip characteristics or performance were observed due to choice of packaging method. Photographs of chips in each of the three packages are shown in Fig. 4.2a (from left to right: ceramic carrier, epoxy carrier, LTCC carrier).

The readout system consisted of two printed circuit boards (PCBs), a daughterboard that housed the chip and a motherboard that held the microcontroller (MicroPython PYB v1.0) used for readout (left panel of Fig. 4.2b). The daughterboard contained a zero-insertion-force socket that the chip plugged into. The

motherboard contained headers that interfaced with the microcontroller. A flat shielded Ethernet cable was used to connect the two PCBs. The microcontroller stored the data locally on an SD card and also sent the data to a graphical user interface on a laptop computer (custom MATLAB GUI) which plotted and stored the data in real time. Power to the chip was supplied by a voltage regulator on the microcontroller, which itself was powered via USB from the computer. A photograph of the microcontroller, and daughterboard inside the incubator is shown in the right panel of Fig. 4.2b.

4.3 Experimental Protocol

The results shown in this chapter are from experiments performed with fabricated sensors. These peliminary biological tests were performed by growing adherent cells onto the chip array. Growth media (RPMI 1640) was prepared with 10 % fetal bovine serum, and supplemented with antibiotics and anti-fungals (penicillin/streptomycin 100×). Human ovarian cancer cell lines A2780 and CP70 were used in this experiment. The cells were grown in a cell culture vessel until they reach lag phase growth. At this point the cells were detached using 0.25 % Trypsin/EDTA, formed into a pellet and re-suspended into 12 mL of fresh cell media. The devices were prepared by sterilizing them with UV light, and rinsing them with deionized water, phosphate buffer solution (Dulbeccos Phosphate Buffer Solution), and cell media. Fresh media was then added and the device was maintained in an incubator (37 °C, 5 % CO_2) for 15 minutes. Then 40 μL of the cell suspension was added to

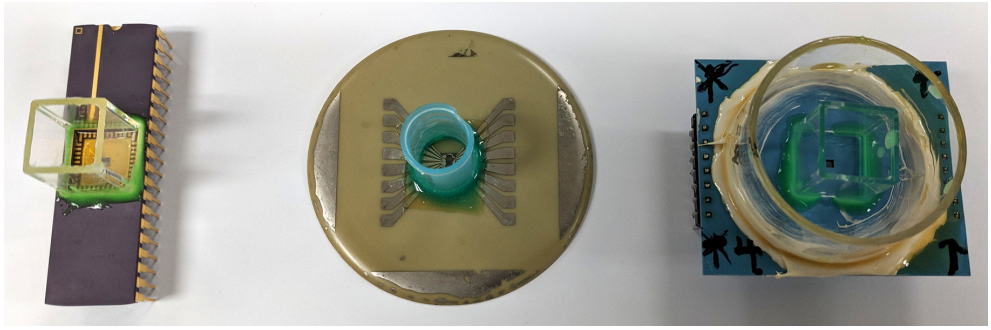

(a)

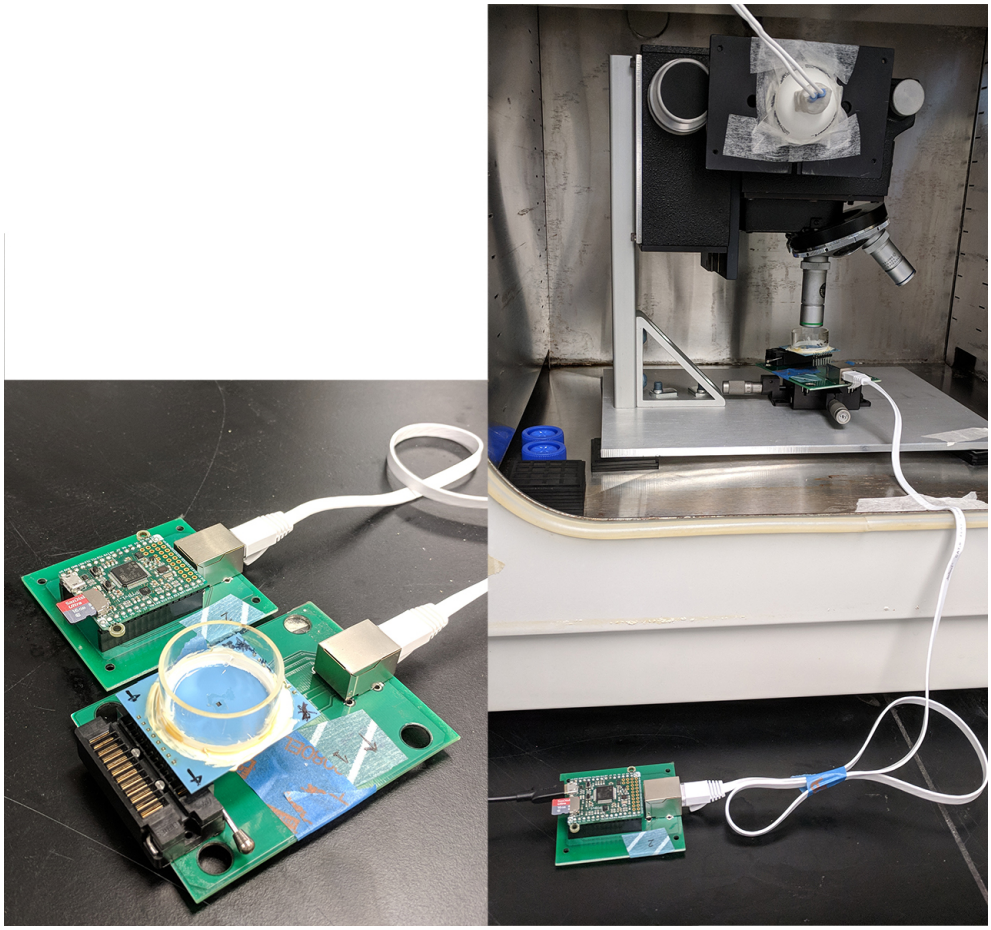

(b)

Figure 4.2: a) Photographs of the capacitance sensor chip packaged using the three different methods (from left to right: ceramic carrier, epoxy carrier, LTCC carrier). b) The test setup. Left: image of a packaged chip on a daughterboard connected to the readout microcontroller using an Ethernet cable. Right: image of the daughterboard inside the incubator.

the device, and data was continuously recorded throughout the experiment. Two separate devices were packaged and plated with each of the two cell lines in separate experiments, resulting in a total of four experimental datasets. All 16 sensor pixels on each chip were active and recording. The devices were kept in the incubator and connected to the readout microcontroller and laptop (located externally) using a shielded Ethernet cable. Fig. 4.2b shows a photograph of the testing setup.

4.4 Tracking Cell Adhesion & Migration

Fig. 4.3a shows response curves obtained from a device plated with CP70 cells. The two vertical lines at $t = 21$ hours and $t = 44$ hours indicate time points when recording was paused to take images of the chips surface, shown in Fig. 4.3b and Fig. 4.3c. For all but one sensor the signal remained relatively low until 5 hours of incubation. This is consistent with the pre-adhesion phase of growth where cells settle onto the chip surface. After this phase, cells start adhering to the chip surface, showing a corresponding increase in signal. The strength of the signal change is indicative of cell growth quality at that electrode, which in turn is dependent upon where the cells first settle down from the solution. Therefore certain electrodes show little change in signal if no initial settling (and subsequent adhesion) occurs. This is evident in sensor 5 (row 2, column 1 of the array) which shows little change through 34 hours of incubation. Fig. 4.3b shows the corresponding absence of nearby cells at this electrode. Likewise, the response of sensor 11 (row 3, column 3) stays below 50 aF through 44 hours of incubation. Both Fig. 4.3b and Fig. 4.3c show this

electrode to have no cells directly on top of the sensing electrodes.

Fig. 4.4 shows results from a second and third experiment, using the same device. Each panel shows the output of two sensors, one that was observed to have cell coverage (red) and one without coverage (black). As before, the results show a correlation between sensor output and observed cell coverage. A difference of at least 500 aF was observed between electrodes with and without cell coverage.

As cells adhere and proliferate, they can also translate from one location to another, a phenomenon called cell migration [69]. This can also be observed in the transient response curves of Fig. 4.3a. As cells proliferate and cover more electrode area, a corresponding increase in absolute sensed capacitance is observed. Likewise if cells migrate away from an electrode, they cover less and less electrode area, causing a corresponding decrease in signal. Several sensor channels show signal fluctuations

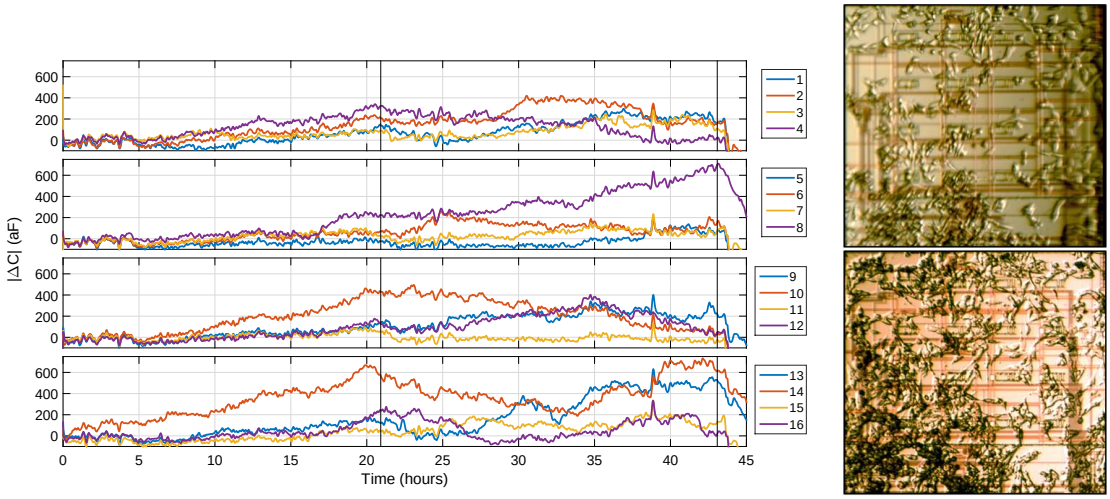

(a) (b) top (c) bottom

Figure 4.3: a) Response curves of the chip as CP70 cells adhere and proliferate across the sensor array. The two vertical black lines at t = 21 hours and t = 44 hours indicate times when data recording was paused for imaging. Right panel shows image of surface of chip after b) 21 hours, and c) 44 hours of incubation of CP70 cells.

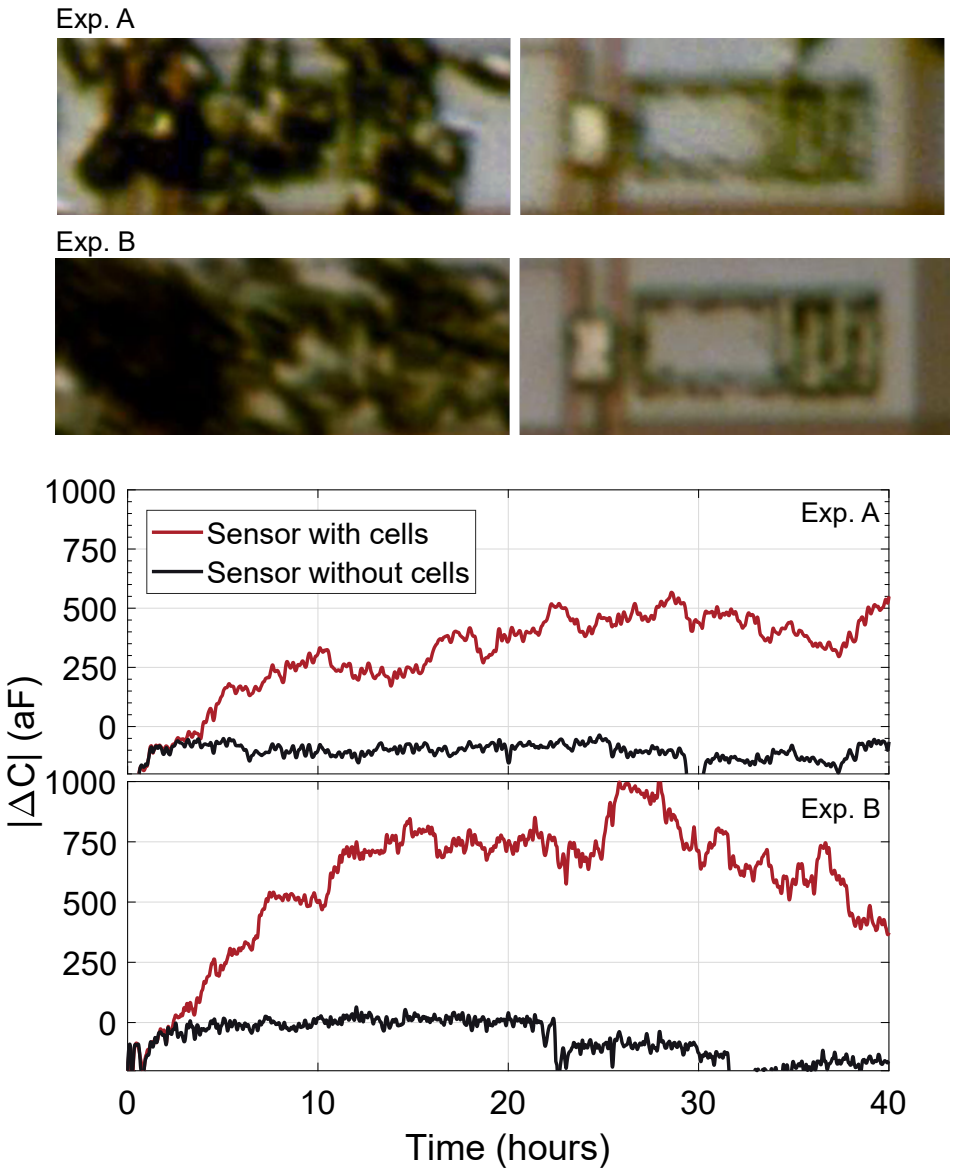

Figure 4.4: Results from two cell experiments performed after cleaning and reusing a device. Lines show output from sensors with (red) and without (black) cell coverage

up and down over a period of several hours. These trends can be caused by cell migration to and away from the electrodes. For example, sensor 4 (row 1, column 4 of the array) shows a gradual signal drop from 300 aF to 20 aF between $t =$ 21 hours and $t = 44$ hours. Examination of the images in Fig. 4.3b,c shows a corresponding absence of cells on sensor 4 between these two time points. Sensors

10 (row 3, column 2), and 16 (row 4, column 4) also corroborate this observation, with decreases of 392 aF and 226 aF, respectively. Additional sample data can be found in Appendix A.2.

4.5 Quantifying Cell Growth Rates

The growth rate of cells can be monitored by looking at the cumulative number of sensors (N_{CS}) in the array that record a significant change in capacitance, designated by a threshold value, during the experiment. Fig. 4.5 shows such a plot with the capacitance threshold set at 200 aF (> 5 times the noise threshold of 22.3 kHz, Section 3.9.2), for each of the four experiments. For clarity, the increments were recorded for each hour of incubation. As can be seen, there is an initial 5 hour period where a small number (< 5) of sensors show a capacitance change. This is indicative of the cell sedimentation process. Then as the cells adhere and proliferate, the number of sensors showing a response greater than 200 aF increases. Over the course of several hours the number of affected sensors increases and plateaus.

A quantitative estimate of the cell growth rate can be obtained by calculating the rate at which sensors detect cells over the course of the adhesion. The slope of N_{CS} for each of the experiments in Fig. 4.5 was calculated; the solid lines show the calculated slope line. A nominal area growth rate can then be estimated by scaling this growth rate by the known 30×30 μm^2 area of each pair of electrodes. Table 4.1 summarizes the estimated growth rate for each of the experiments.

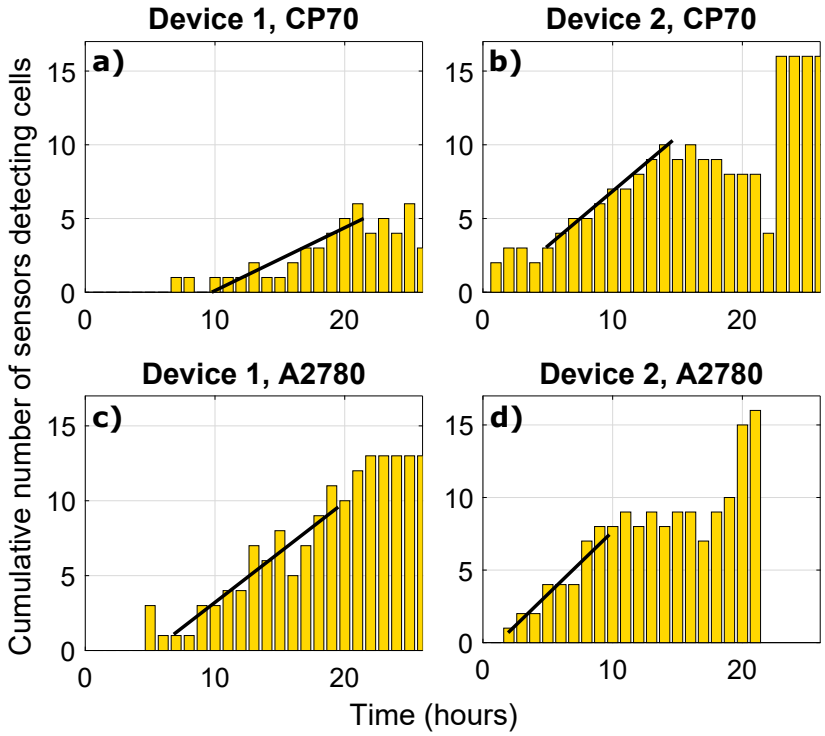

Figure 4.5: Cumulative number of sensors that show an increase in capacitance as a function of time, for each of the four experiments described in Section 4.3. The large plateau after 22 hours in (b) is due to solution evaporation.

Cell Line	Device	Adhesion Time (hrs)	Growth Rate (sensors/hr)	Growth Rate (μm^2/hr)
CP70	1	11.7	0.43	380
CP70	2	9.8	0.74	670
A2780	1	12.7	0.67	600
A2780	2	7.8	0.87	780

Table 4.1: Cell Growth Rate Estimation

The experimental data shows a clear pattern of cell coverage detection; as a larger area of a pixel's electrodes are covered, a corresponding increase in the sensor signal is recorded. Fig. 4.6b shows the average capacitance change across all experiments. A linear fit ($R^2 = 0.94$) estimates a response of 100 aF/cell. Error bars corresponding to the standard deviation of the measurements indicate that variability is relatively large compared to the mean: $\pm$200 aF for 2 cell coverage.

However, since the experiments vary in both device used and type of cells cultured, discrepancies are expected.

The dynamic change in measured capacitance also has strong correlation with changes in cell coverage. Fig. 4.7 shows such a plot for the experiment with Device 1 and CP70 cell line. The change in measured capacitance (ΔC) is the difference in signal between two time points that correspond to the two images. The change in cell coverage is the difference in the estimated number of cells covering each pixel at the two time points. For this experiment the change in coverage ranged from -3 to $+2$ cells.

As can be seen there is a correlation between the change in cell coverage and

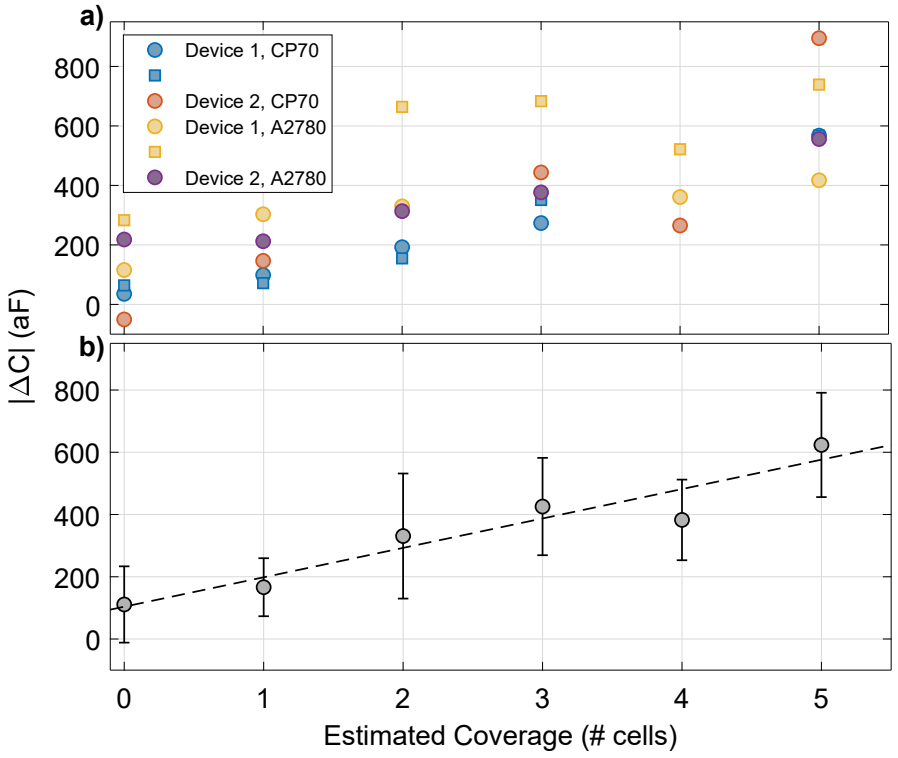

Figure 4.6: Plot of the measured sensor response as a function of estimated cell coverage of pixels. a) All experiments separately, b) Mean value. Linear fit shows a sensitivity of 100 aF/cell.

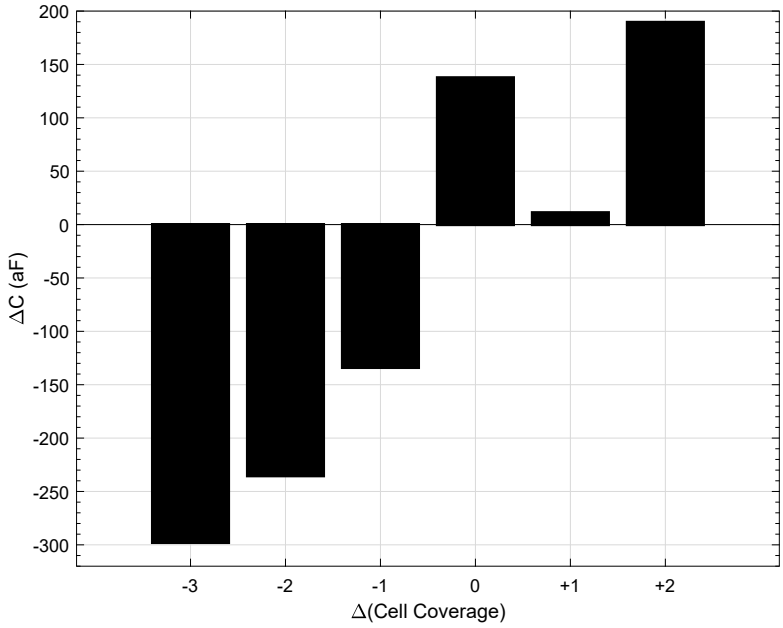

Figure 4.7: Plot of the measured change in capacitance as a function of change in cell coverage (Device 1, CP70 cells)

the change in measured capacitance. An average decrease of 300 aF in the signal was observed for sensors that showed a 3 cell decrease in coverage between the two time point, and a 130 aF decrease for a sensors exhibiting a single cell decrease in coverage. However an average signal increase of 140 aF was measured for sensors that had no change in coverage. We note that the cell coverage estimates were obtained manually and reflect an estimate of the number of cells on the electrode, so reported changes in cell coverage are limited in accuracy.

4.6 Summary

This chapter presented preliminary results of *in vitro* cell experiments using the cell capacitance sensor. The chip was packaged using three different meth-

ods (including one assembled at the University of Oulu) and does not require any surface functionalization or post-processing prior to experiments. Human ovarian cancer cell lines CP70 and A2780 were cultured in wells attached to the chip surface, and capacitance data was taken automatically over a period of three days. Microscopic images were taken of the sensor surfaces during the experiments to provide visualization of cell growth and proliferation.

Analysis of the data showed transient capacitive changes during experiments which correlated with visual images of the chip. Estimates of the cell growth rate were obtained from analysis of the transient data for each experiment. Cell migration was also observed at some sensor locations. Finally, the sensitivity of the sensors was quantified by comparing the measured capacitance responses to the cell coverage at each individual pixel. Analysis of four experiments showed good correlation between cell coverage and change in capacitance measurement.

In the following chapter, higher resolution imagery is used to further validate measurements from the chip, including the investigation of single cell binding events.

Chapter 5

Real-time Imaging in Lab-on-CMOS Applications

5.1 Preface

This chapter includes excerpts of an article published in IEEE Transactions on Biomedical Circuits and Systems that was authored by myself, Sheung Lu, Dr. Marc Dandin, Dr. Elisabeth Smela, and Dr. Pamela Abshire. The core idea for the two well cell culture platform was formulated in discussions with Sheung Lu. Sheung additionally sourced parts for the custom microscope assembly. My other contributions include setting up and performing the experiments, developing the cell detection algorithm, performing image processing, and most of the writing.

5.2 Introduction

In order to obtain accurate ground truth information, it is important to be able to obtain visual confirmation of what is occurring on the sensor surface. This is especially important since capacitive changes are the result of changes in the permittivity of the immediate surroundings at the input electrode, whether it be due to the adhesion of cells or changes in the media. The quantification of data presented in Section 4.4 used ground truth information from manual discrimination of cells based on microscopic images. There are a few drawbacks with this approach. Manual human identification is inherently subjective since it is difficult to make estimates that

are always consistent throughout multiple trials. Therefore a method of objectively quantifying ground truth cell coverage would be beneficial. A major obstacle that exacerbates the issue of subjectivity is the difficulty in obtaining clear images of the sensor surface. Since the sensor substrate is opaque, imaging techniques that require a through-sample optical path cannot be used. These include phase contrast and inverted light microscopy that are normally used in microbiology. This means that reflective microscopy is required. However, acquiring clear images with this method is difficult due to light refraction through the air-liquid interfaces, as can be seen in Fig. 4.3b,c. In order to mitigate this problem, higher-quality images could be obtained using a microscope with immersion lenses [6].

Another important consideration in validating the biosensor is having higher temporal resolution of the ground truth. This means continual imaging of the sensor surface as the experiments are run. This introduces logistical difficulties since the sensor would need to be moved to an imaging facility numerous times through a recording session. The physical movement itself could compromise the viability of cells since the samples need to be removed from the cell culture incubator often. This chapter presents work towards building a platform to perform long-term and concurrent time-lapse imaging and data collection. No such platform has previously been reported for LoCMOS sensors.

5.2.1 Visualizing Cells

Cells absorb little to none of the light that passes through their bodies. Rather cells are phase objects: they create changes in image contrast due to variations in their thickness and their different refractive index from the cell media [70]. As such, a number of different microscopy methods have been developed to properly visualize cells. Fluorescence microscopy involves the addition of a fluorescent stain that can label certain proteins or chemical compounds within cells. These labels are excited with light at a certain wavelength, and the resulting fluorescence emission can be measured. However, the dyes themselves can affect normal cellular function and so are rarely used in long-term live cell imaging [15]. Additionally, the excitation light intensity can be phototoxic to cells, and affect their behavior over time [70, 15]. Phase-contrast and differential interference contrast microscopy are popular label-free alternatives to fluorescence imaging [71]. They use additional optical hardware to convert phase shifts caused by cells into detectable light intensity variations. Most cell microscopy methods are commonly used with optically transparent samples, and so are not suitable for imaging cells on optically opaque CMOS chips.

5.2.2 Challenges

There are several significant challenges in obtaining clear images of a CMOS sensor in the cell culture environment. Since the sensor substrate is opaque, imaging techniques that require a through-sample optical path cannot be used. These include phase contrast and inverted light microscopy that are commonly used in mi-

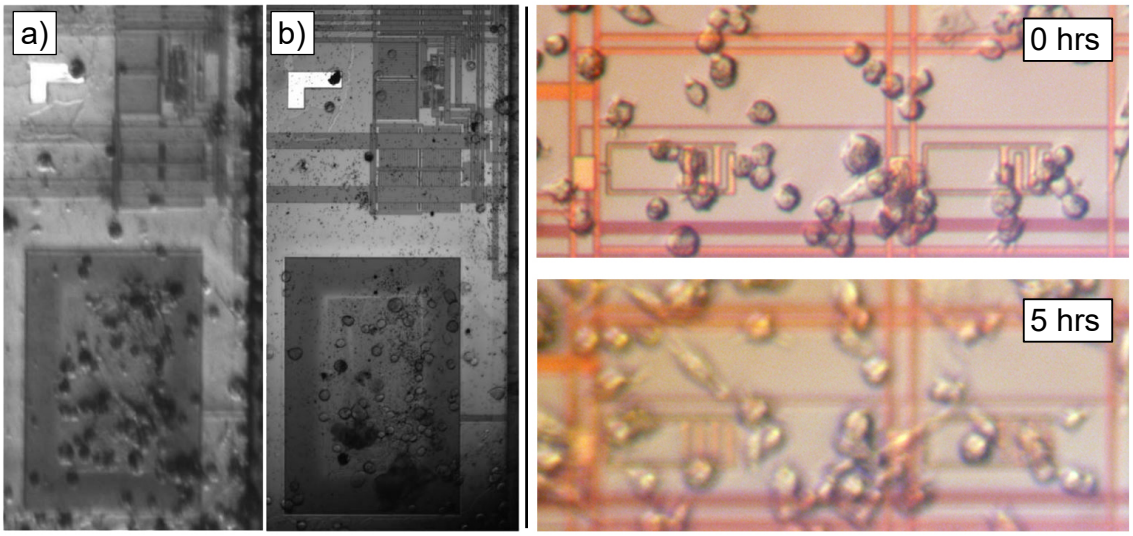

Figure 5.1: Photomicrographs of cells on CMOS chips. Left: Images of sensory neurons taken with a) standard objective lens, b) immersion lens. Image from [6]. Right: Images of ovarian cancer cells, with media evaporation resulting in loss of focus after 5 hours.

crobiology. This means that reflective microscopy is required. However, acquiring clear images for samples in a fluid environment with this method is difficult. Light refraction through the air-liquid interface results in blurry or poor quality images, as can be seen in Fig. 5.1a (left panel). Curvature of the interface due to surface tension (i.e. meniscus) is particularly problematic. Higher-quality images can be obtained using immersion lenses [6], which are designed to be used with an immersion liquid (e.g. oil). Water immersion lenses, in particular, can be used for live cell imaging by dipping the lens directly in cell medium, resulting in much clearer images Fig. 5.1b (left panel). However these lenses are quite expensive and are not typically used for long-term observation [72].

Mammalian cells require a stable growth environment that matches physiological conditions, usually achieved by keeping the sample inside an incubator (37 °C, 5% CO_2). Since a continuous stream of images is required for validating the

high-temporal resolution sensor data, the sensor/culture would need to be moved to an imaging facility numerous times throughout a recording session. This would compromise the viability of cells since the device needs to be removed from the controlled culture environment. This often means that the sensor recording needs to be stopped and restarted as well. Therefore, imaging should occur continuously within the cell culture environment.

Furthermore, the cell media has to be maintained at a constant pH level for optimal growth conditions. This is ensured by gaseous exchange with 5% CO_2 within the incubator, so the culture well cannot be covered with an airtight seal. During long-term experiments, this leads to evaporation of the cell media which increases the salt concentration and osmotic pressure and decreases viability [73]. Media evaporation further causes a change in the height of the air-liquid interface, leading to the sensor surface moving out of focus, as can be seen in the right panel of Fig. 5.1. This is not an issue in traditional transmittance-based microscopy, because the lens is focused on the underside of culture well that always remains the same distance away from the lens.

5.2.3 Alternative Imaging Systems

Several research and commercial grade systems exist that integrate cell culture incubator conditions and imaging [74, 75, 76, 77, 78]. These systems generally incorporate an inverted microscope, illumination sources, and CCD camera into an incubation chamber with standard heat and humidity controls. The stage po-

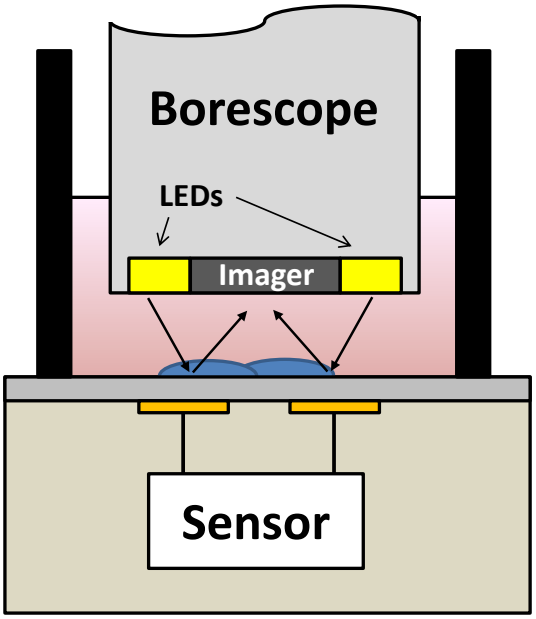

Figure 5.2: Schematic of a borescope-based imaging system. Placement of the lens within the cell solution can help to reduce effects of light refraction.

sition can either be manually or automatically controlled. Each of these systems are designed for use with transparent samples since the inverted microscopes rely on light transmission through the samples. Since substrates on lab-on-CMOS chips are opaque these systems would not be applicable without modifications. Jin *et al.* developed a wireless imaging platform that can be placed inside commercial incubators [74]. It is based on a Sony QX10 camera that his housed in a 3D printed bracing structure that includes an excitation filter, emission filter and lens for fluorescent microscopy applications. The camera itself is WiFi enabled and so it can be controlled remotely, eliminating the need for wiring that needs to pass out of the incubator door, which can compromise the stability of the incubation environment.

A low-cost alternative could take inspiration from healthcare. Endoscopes

and borescopes are visual inspection devices with a camera head on one end and an eyepiece on the other. Video versions of these devices act as miniature video cameras with the eyepiece replaced by either a video screen or connection to a computer. Additionally, endoscopes in particular are designed to be waterproof. If the camera-end of the scope can be placed into the culture well, then the problems of refraction may be avoided. Electronic cameras can be done remotely to allow for automatic time-lapse imaging (Fig. 5.2).

Another system would involve the use of a normal reflective microscope, with an attached CCD camera. This would be similar to the setup developed by Jin *et al.* [74], with a modified light source and microscope/lens setup in order to work with opaque substrates. An important constraint with this approach is the physical size of the well. The walls of the assay well need to be high enough to contain enough cell media during experiments. Therefore they will limit how close the microscope objective lens can get to the sample. A possible solution is to use a microscope that has a long working distance at the cost of lower magnification, and loss of image quality due to refractive effects.

5.2.4 Previous Approaches

Imaging cells on top of CMOS chips has been performed using different microscopy methods, including normal light [10, 11, 37, 57], scanning electron [79, 80, 81, 82], and fluorescence-based methods [83, 84, 85, 86, 87]. Park *et al.* obtained fluorescence images of cells at 24 hour intervals to validate impedance measurements

[85]. They also monitored cells during extracellular stimulation and recording [83]. Chi *et al.* used a fluorescence image to validate cellular impedance and optical measurements [84]. Lopez *et al.* and Abbot *et al.* used fluorescence images to locate cells for comparison with extracellular recordings [86, 87]. Niitsu *et al.* used light microscopy to correlate cell locations with cyclic voltammetry measurements [37]. Nabovati *et al.* used light microscopy to image cells on top of a capacitance sensor chip [11]. Couniot *et al.* used images of cells to count cell coverage in order to quantify the sensitivity of their device [10]. However, in each of these cases, imaging was done at discrete time points outside the incubator using standard imaging platforms. This is sufficient for some applications such as extracellular cell monitoring where a single snapshot of neuron locations is adequate to localize sources. However for other applications such as cell proliferation or motility monitoring, these imaging techniques do not meet the temporal resolution needed to correlate with cell morphological changes.

5.3 This Work

5.3.1 In-incubator Imaging

This work uses an in-incubator platform to perform long-term imaging of live cells on LoCMOS. A standard reflective microscope head unit (Microzoom II, Bausch & Lomb) with a camera (16 MP, Amscope) is secured to a custom-machined microscope assembly that was designed to fit within the incubator (Isotemp, Fisher Scientific). A white LED lamp (MR16, EcoSmart) with a peak emission wavelength

of 960 nm was used as the light source. The CMOS chip is placed under the microscope on top of a two-axis linear stage (Thorlabs) to facilitate XY alignment, with height controlled using the vertical adjustment of the microscope head unit. A standard objective lens with a long working distance (>2 cm) is used to facilitate positioning of the LoCMOS within a cell culture well. The sensor is powered and automatically collects data while images of the sensor surface are automatically taken every 5 minutes. Since the system has minimal wiring requirements, it does not disrupt normal operation of the incubator, ensuring a stable culture environment (37 ° C, 5 % CO_2). This allows data to be recorded over the course of the experiments (up to 3 days), in an unsupervised and uninterrupted manner.

5.3.2 Dual-Well Approach

A dual-well structure, as shown in Fig. 5.3a, was developed to alleviate the challenges of imaging CMOS chips. The inner well serves as the primary culture well where cells interact with sensors. This well is filled with cell media and covered with a glass coverslip to prevent media evaporation and keep a fixed focal distance for microscopy. A larger outer well is also filled with cell media but is left uncovered to allow gas exchange and maintain physiological pH levels. Ports are created in the inner well to allow for diffusion between the two wells, thereby maintaining proper growth conditions in the inner well.

The size and shape of the well can be customized for different package sizes. In this work, the primary well was formed using a cuvette (10×10 mm) that was

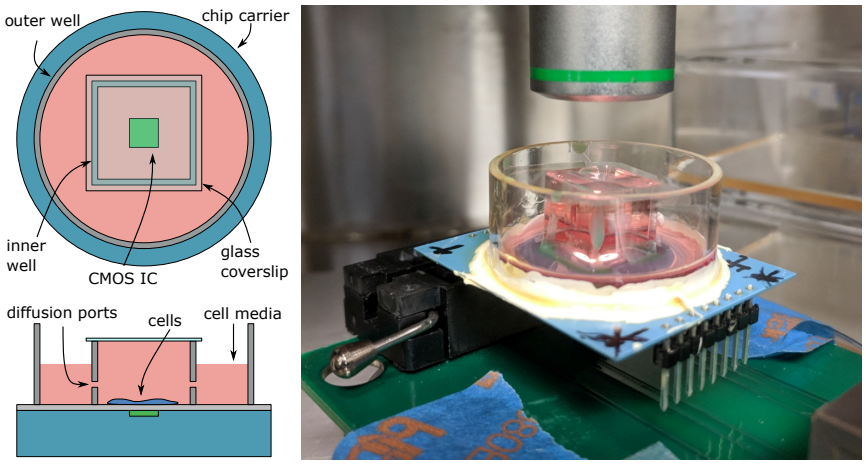

(a) (b)

Figure 5.3: a) Schematic of dual-well package. b) Photograph of packaged chip inside an incubator

glued onto the packaged device using a using a bio-compatible silicone glue (Kwik-Cast, World Precision Instruments). The cuvette had 5 mm holes drilled through the bottom of two of its sidewalls to create the diffusion ports. The secondary well was formed by attaching a larger plastic tube (30 mm diameter) on the device. The outer well should be taller than the inner well to prevent media overflow. A photograph of a packaged device is shown in Fig. 5.3b.

5.4 Live Cell Experiments

5.4.1 Experimental Protocol

Human ovarian cancer cell lines A2780 and CP70 were prepared following the protocol described in Section 4.3. Prior to each experiment, the packaged devices were sterilized by exposure to UV light for 30 minutes. They were then sequentially rinsed with deionized water, phosphate buffer solution, and fresh cell media. Both

wells on the device were filled with pre-warmed cell media and then 10^5 cells/ml were added directly over the sensing area using a micropipette. More media was then added to fill the primary well and then a coverslip was used to seal the well. Excess media was then aspirated out from the secondary well, allowing the coverslip to form a tight seal around the primary well. The device was then placed inside an incubator and recording was started. Cells were allowed to grow for 72 hours before the experiment was stopped.

5.4.2 Experimental Results

In order to validate the capacitance sensor measurements, experiments were first conducted with the imaging and sensor recordings running concurrently. Fig. 5.4 shows time-lapse images taken using the in-incubator imaging system along with the corresponding capacitance measurements for four sensors in the array. During this portion of the experiment, cells were pipetted into the culture well over the sensor array, then allowed to settle onto the chip surface in a random manner.

As cells first seeded onto the surface they were rounded, as can be seen in image A of Fig. 5.4a. While this initial binding is weak, a noticeable difference was seen in channels 2 and 4, which had an initial seeding of cells compared to channels 1 and 3, which were void of cells. Over the next several hours, the cells began to flatten and adhere more strongly, as can be seen in the progression to images B and then C. Corresponding capacitance increases to 380 aF and 600 aF were seen in channels 2 and 4, respectively. Channel 3 showed a brief increase in capacitance between hours

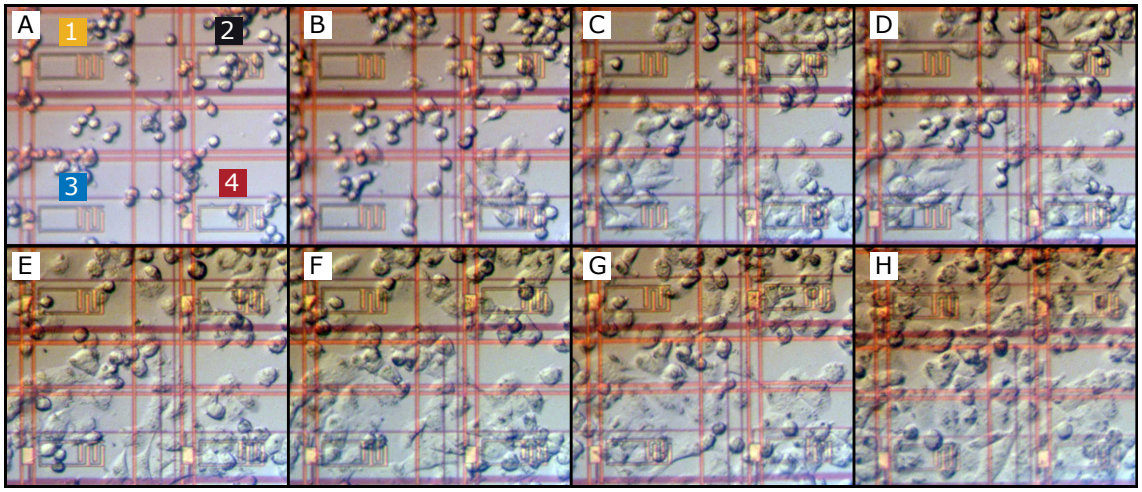

(a)

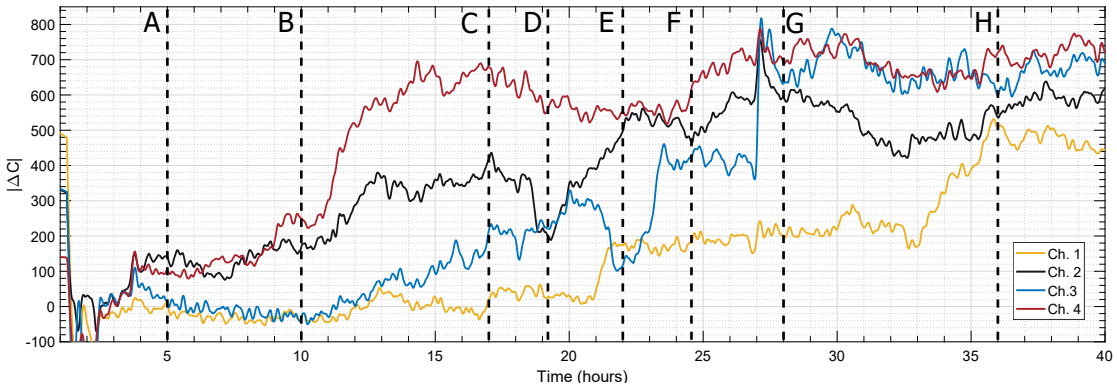

(b)

Figure 5.4: Correlation of capacitance measurements and time-lapse imaging of cells on the chip during cell-substrate binding. a) Images taken of four sensors at different time points. b) Corresponding sensor responses showing the measured capacitance changes over time. The letter markers indicate the time points corresponding to each frame. Video is available as supplementary material.

19 (image D) and 22 (image E). This was due to the cell on the top-right of the electrode, which traversed from the top of the electrode to the bottom over this time period, briefly increasing the capacitive coupling. Additionally, channel 1 showed a sharp increase in capacitance of ∼200 aF at 21 hours. This was due to the cell to the top-right of its electrodes, which moved downwards towards the center of the electrodes and remained there, as can be seen between images D and E. Channel

2 measured a brief 215 aF dip in capacitance at 19 hours. This was due to the cell on top of the electrodes (image C) undergoing cell division. The two resulting daughter cells (image D) covered approximately the same area of electrodes as the parent, but the daughter cells were probably not as well adhered, resulting in a drop in measured capacitance. Over the next several hours these cells started to grow and to bind to the substrate, resulting in the increase in measured capacitance.

Fig. 5.5 shows results from another experiment where cells were allowed to grow unhindered. The top panel shows time-lapse images of four electrodes taken during the experiment and the bottom panel shows the corresponding capacitance data. The dashed lines and letters indicate the time points for each image.

When cells are first seeded into the culture well, they float in solution before settling down in random locations on the CMOS chip. At this point they are initially round and are just beginning to adhere (image A). As time progresses the cells form stronger connections to the surface, flatten in shape and spread outward (images B and C). Channel 1 in Fig. 5.5a shows little change in capacitance until 32 hours into the experiment (image E) where most of the electrode area becomes covered with cells causing a peak of 600 aF. In the next five hours, the measured capacitance drops by 200 aF as the electrode coverage area reduces due to one of the cells dividing (image F). In another example, channel 2 shows a drop of 200 aF from 25 to 27 hours that is also caused by a dividing cell. Image C shows the parent cell and image D shows the two daughter cells. Channel 3 shows noticeable increase in coverage between images A and B, with the corresponding increase of 300 aF during this time. There is continued electrode coverage through 35 hours of growth followed by

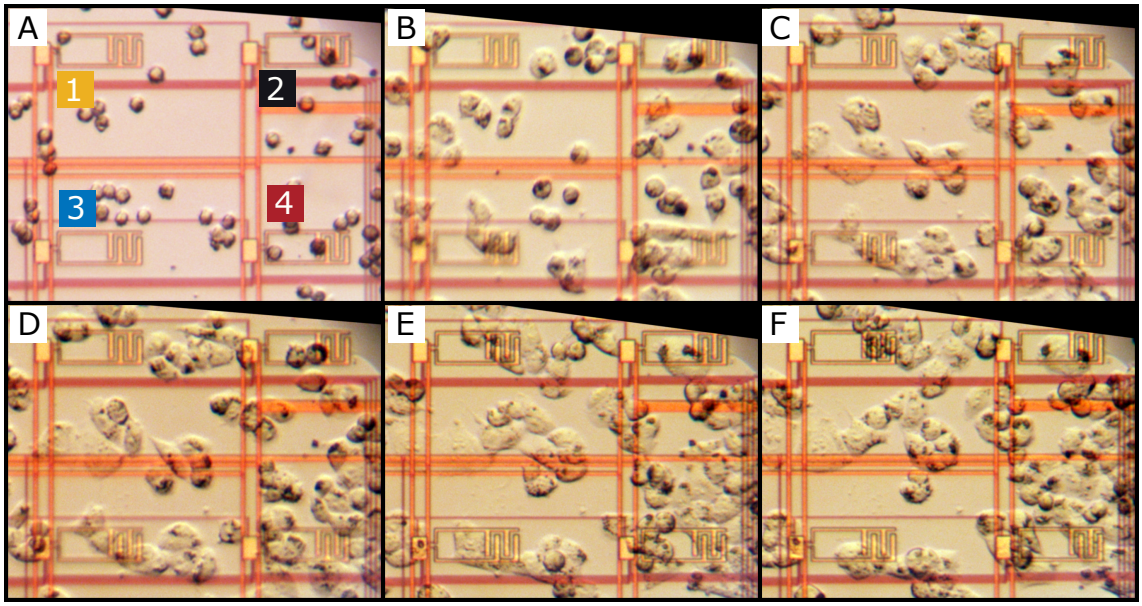

(a)

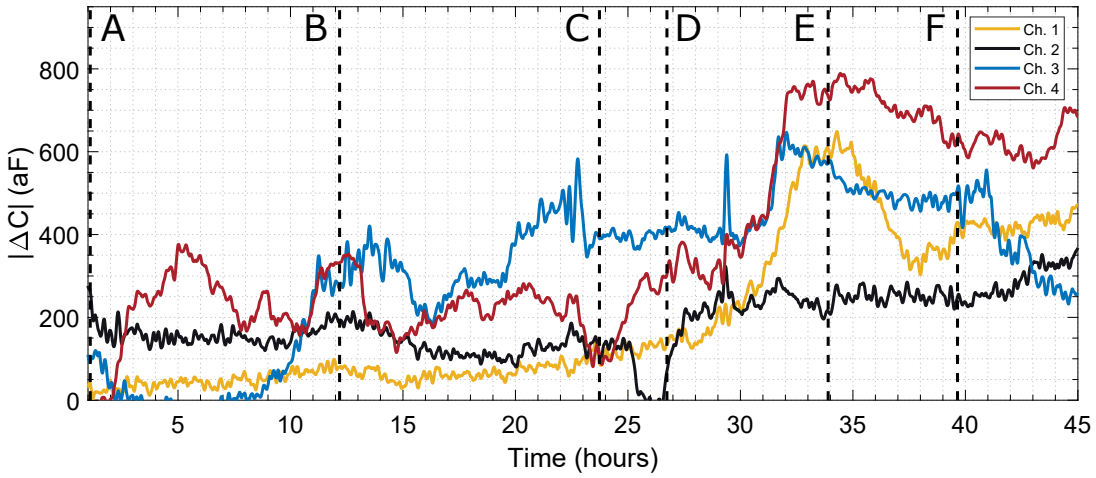

(b)

Figure 5.5: Correlation of capacitance measurements and time-lapse imaging of cells on the chip during cell-substrate binding. a) Images taken of four sensors at different time points. b) Corresponding sensor responses showing the measured capacitance changes over time. The letter markers indicate the time points corresponding to each frame. Video is available as supplementary material.

a decrease of roughly 200 aF as the cell shifts downwards. Sensor 4 shows examples of cells undergoing morphological changes. At 12 hours, a pair of cells stretches across all for fingers of the electrode, resulting in a bump in capacitance of 350 aF

(image B). Twelve hours later, the electrode area becomes relatively empty leading to a drop of 250 aF (image C). At 34 hours cells start to expand and adhere well across the electrodes, bringing the sensed capacitance to a peak of 750 aF (image E).

Repeat experiments were performed using the two cell lines and showed similar growth profiles. The maximum mean capacitance change measured by the sensor for electrodes fully covered by cells was 1 fF. This results in a coverage sensitivity of roughly 1.1 aF/μm^2.

5.5 Cell Segmentation

As a first step in validating capacitance measurements with ground truth images of cell coverage, we describe image processing techniques to automatically calculate sensor coverage area for each of the collected time-lapse images. It is then possible to correlate coverage estimates with capacitance measurements. The process of using image analysis techniques to detect cell shape and size is called cell segmentation.

Images of samples containing dissociated cells, or small fragments of tissues on glass slides (cytopathology samples) are generally more amenable to segmentation due to well-separated cell membranes and a clear background. On the other hand, samples that preserve whole tissues (histopathology samples) are much more complex, with cells of various sizes and shapes embedded amongst a noisy background. These types of samples however are often prepared with well-characterized stains

that can help to identify regions of interest such as cell nuclei and membranes [7].

In this work, cells are grown *in vitro* directly on top of the CMOS chip and normal reflected light microscopy is performed. As can be seen in the time-lapse images in Fig. 5.4a, cells appear as translucent, irregularly-shaped features that are primarily identifiable through the slight contrast differences along their membranes. It is also important to note that cells are unlabeled, i.e. no dyes or probes are added to enhance cell contrast. Another factor that exacerbates image processing challenges are the visible features of the chip itself, especially the underlying metal layers that are used for signal routing and electrode formation. These features appear very prominently in reflected light microscopy and easily obfuscate the outlines of cells that would normally be visible under a uniform background.

5.5.1 Background

Many different segmentation methodologies have been proposed, however these can generally be classified into a few categories: intensity thresholding, feature detection, morphological filtering, and region accumulation [88]. Image intensity thresholding is a basic strategy that assumes cells appear consistently darker or lighter compared to the image background. Thresholding the image using a global or adaptive value can then give an initial estimate of the cell shape and location. Edge detection and linear image filtering are examples of feature detection algorithms applied to cell images. They leverage prior knowledge of cell features. Morphological filtering uses mathematical morphology theory to filter images based on basic image

shapes, called structuring elements. These are shapes that are the basis for performing a dilation (enlarging features), erosion (shrinking features), or combinations of the two operations. If the locations of cell nuclei or cell centers are known, then one can iteratively grow regions surrounding that initial seed point to form a group of labeled pixels. Here, we perform cell segmentation using morphological filtering and thresholding methods.

5.5.2 Algorithm

5.5.2.1 Pre-processing

As mentioned previously, the visible features of the chip itself introduce a challenge in traditional segmentation approaches. Therefore, all images are first processed to reduce the intensity of these features. This is performed by converting images to grayscale and then normalizing all frames using a reference image consisting of a bare electrode. The first step in pre-processing the images is to register (align) each frame to the reference. This is required because the sensor surface may shift slightly over time under the microscope. An iterative intensity-based registration algorithm is used to perform the alignment. The next step is to perform the normalization using the reference image. As seen in the sample images in Fig. 5.5a, the central and outer regions of cells are brighter and darker compared to the background, respectively. To emphasize these two regions, the image normalization is performed in two parallel paths. First a direct subtraction and scaling is done directly on the frame and reference. Second, both images are complemented before

subtracting and scaling. The result of these two flows are images that emphasize the dark and bright portions of the cells as can be seen in Fig. 5.6b and c, respectively.

5.5.2.2 Cell Detection

These images are then binarized using an adaptive thresholding approach [89]. This results in preliminary binary masks that delineate cell coverage (Fig. 5.6d). The red and orange portions of the image correspond to the thresholded dark and bright regions, respectively. Next, morphological image processing is performed to denoise the mask based on expected models of cell shape and sensor surface features. The two basic morphological operations are erosions and dilations. The mask images are probed using a disk-shaped structuring element, to shrink or enlarge the base image. An erosion is performed using a structural element to filter out any false positives caused by features of the chip that were not removed during reference subtraction. This is evident, for example, in the false positives created by the

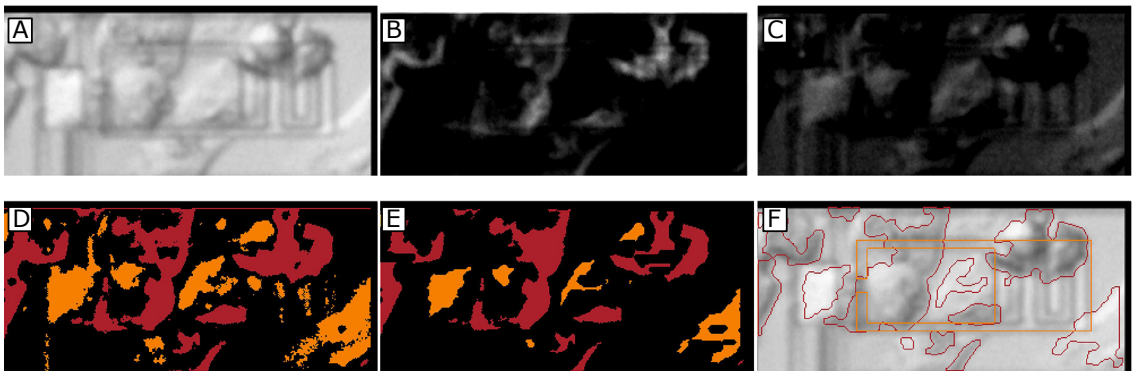

Figure 5.6: Images of intermediate steps in cell segmentation algorithm. a) Original image of cells over sensor electrode. b, c) Result of registering and subtraction of bare reference electrode for dark (b) and bright (c) emphasis. d) Output of two-level adaptive thresholding with orange and red regions corresponding to bright and dark levels, respectively. e) Mask after morphological filtering. f) Detected cell coverage regions and electrode area, marked in red and orange outlines, respectively.

interdigitated electrodes in Fig. 5.6d. Dilation is then performed to expand the mask area around edges that were not well defined after reference subtraction. The result of these operations on the bright and dark emphasized masks are then combined (Fig. 5.6e) and dilated once more. Finally, any remaining holes in the mask are filled. Fig. 5.6f shows the outline of the final mask (red) along with the outline of the electrode sensing area (orange). The overlap between the two regions is the final estimated coverage for each frame. Listing 1 and 2 outlines the image processing steps. The comment lines include letters in the parentheses that correspond to the sample images in Fig. 5.6.

Listing 1 Cell segmentation pseudocode

```
//register image (a)
x = registerIm(input,ref);
xc = complementIm(x);
refc = complementIm(ref);
darkIm = processIm(xc,refc);
if (doBrightIm) {
    brightIm = processIm(x,x0)
}
//combine and fill mask (f)
mask = darkIm | brightIm;
mask = dilate(mask, line0/90);
mask = erode(mask, disk2);
mask = fill_holes(mask);
```

Listing 2 Image processing pseudocode

```
function processIm(x,x0) {
    //subtract reference (b,c)
    xref = x-x0;
    //binarize image (d)
    mask = threshold(xref, 3 lvl, adaptive);
    //clean mask (e)
    mask_hz = erode(mask, horizontal lines);
    mask_hz = dilate(mask, line0/90);
    mask = mask & ~mask_hz;
    mask = erode(mask, disk1);
    mask = fill_holes(mask);
    return mask;
}
```

5.5.3 Results & Discussion

The cell coverage detection algorithm was then evaluated using a dataset of images generated through the imaging and cell culture protocols described in Sections 5.3.2 and 4.3, respectively. Three experiments were performed using the two cell lines (1 $\times$ A2780, 2 $\times$ CP70), and a subset of the data consisting of capacitance measurements from nine sensors and their corresponding time-lapse images (3196 frames) was used for analysis.

5.5.3.1 Sensor Correlation

The image processing was performed on each image in the dataset resulting in an estimate of cell coverage as a function of time. Fig. 5.7a shows examples of time series results of the segmentation. The red traces (scale on right axis) are the estimated electrode coverage area and the black traces (left axis) are the corresponding

capacitance measurements. Through multi-physics simulations [55] and observation of the time-lapse images and sensor data, we expect capacitance measurements to be proportional to the area coverage of the electrodes. Therefore, if a larger area of the electrodes is covered we expect a larger corresponding change in capacitance. As can be seen in Fig. 5.7a, there is indeed a clear qualitative correlation between coverage and capacitance. At the beginning of experiments when cells have just settled, they are at their smallest size leading to a low electrode area coverage and at the same time the capacitance is relatively low. In both examples, capacitance increases after 10 hours and there is a corresponding increase in coverage. Interestingly, decreases in capacitance are also correlated between the two curves. For example, the drop in capacitance between 21 and 23 hours for dataset 1 is reflected in the coverage estimate as well. It is important to note, however, that the capacitance and coverage scales are not expected to have one-to-one correspondence. Indeed, one expects the capacitance gain (capacitance per unit area) would vary from pixel to pixel due to process variations. To better quantify the capacitance-coverage relationship, we look at scatter plots of capacitance vs. coverage (Fig. 5.7b). As can be seen, there is a roughly linear relationship between the two variables ($r_{cov} = 0.93$ for both, Pearsons correlation coefficient). The majority of the data points follow the linear trend although several clusters of outliers exist. For example, the cluster of points in dataset 1 that lie below the best-fit line at $20-30$ hours is due to the over-reporting of the electrode coverage by the detection algorithm. The correlation coefficients have a mean of 0.80 and standard deviation of 0.12, across the nine datasets, each reflecting data collected from a single sensor over three experiments.

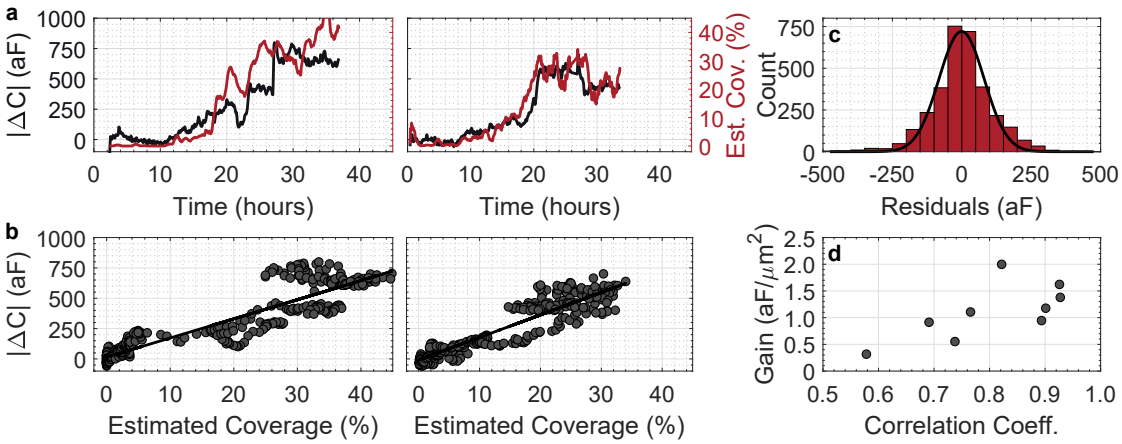

Figure 5.7: Correlation of measured capacitance and estimated cell coverage. a) Capacitance and coverage plotted as a function of time for two exemplar datasets. b) Scatter plots of capacitance vs. estimated coverage, with linear regression line, for the data in (a). c) Histogram of the difference between fit line and measured capacitance values for all datasets (N = 3196). d) Derived sensor gain vs. correlation coefficient.

A histogram showing the residuals between measured capacitance values and the linear best-fit lines is shown in Fig. 5.7c. The figure reflects data from all 3196 frames/datapoints. A Gaussian fit of the data ($R^2 = 0.97$) results in a distribution with a mean of -1 aF and standard deviation of 80 aF. Using a 2σ threshold to cover 95 % of the distribution, the error would be 1 ± 160 aF.

Several factors contribute to this relatively large error, with variability resulting from both the segmentation algorithm and also biological responses. First, the quoted error metric is calculated under the assumption that the coverage estimates from image processing provide ground-truth data, and that deviations from the best-fit linear line are the consequence of error in capacitance measurements. A more accurate figure could be obtained if each of the images in the dataset were manually processed to mark areas of cell coverage. This ground truth dataset could then be used to refine both sensor calibration and algorithms for estimating cell coverage.

Another source of variability is the quality of cell binding for given coverage area. Cells that are in their initial state of attachment (e.g. cells that have just been seeded into a well) primarily stick to the substrate through electrostatic interactions [26]. Over time, cells form a complex structure of cell adhesion molecules that bind them to the substrate, thus increasing the coupling strength. Therefore, given two cells that cover the same surface, the capacitive coupling of the two will be different depending on how well developed the bonding is. Since image processing treats area coverage equally, this binding quality is not considered.

5.5.3.2 Sensor Gain

Given the expected linear relationship between electrode coverage and capacitance, the slopes of the best-fit correlation lines calculated in Section 5.5.3.1) (and shown in Fig. 5.7b) are a measure of the sensors gain. Fig. 5.7d shows a scatter plot of the slope values as a function of rcov for each of the nine datasets. The slopes range from 0.32 to 2.00 aF/μm^2 with a mean of 1.11 $\pm$ 0.52 aF/μm^2. These values are of course highly dependent on the accuracy of coverage estimation. Indeed, datasets with higher rcov show a tighter distribution. If we focus on datasets with a good capacitance-coverage correlation ($r_{cov} > 0.85$), we see a mean sensor gain of 1.28 $\pm$ 0.29 aF/μm^2. This value is close to the initial estimate of 1.1 aF/μm^2 obtained using the mean maximum measured capacitance (Section 4.4). It is also with range of the sensitivity values in existing literature (see Table 8.1). The result can also be improved given a larger number of image and measurement datasets.

Further improvements of the cell segmentation algorithm can also be performed by leveraging machine learning or neural network structures to improve classification accuracy.

Chapter 6

Applications, Part 1: Mitotic Activity Detection

6.1 Preface

Here were present work towards using the capacitance sensor chip as a tool for cancer research applications: detecting cell mitotic activity. This is relevant in two respects: 1) mitotic activity in tissue is an important indicator in cancer prognosis, and 2) detection of mitosis events can be used as a marker for cell cycle-targeted therapy development.

This chapter includes excerpts of a manuscript in preparation with authors including myself, Sheung Lu, Dr. Marc Dandin, Dr. John Basile, Dr. Elisabeth Smela, and Dr. Pamela Abshire. My contributions include setting up and performing the experiments, image and data analysis for mitosis event detection, developing the automated detection algorithm, and most of the writing.

6.2 Introduction

6.2.1 Mitotic Counts

Histologic grading, the visual classification of cancer cells and tissues, is an important prognostic factor and indicator of metastatic risk in cancer patients. Counting cell divisions in particular is an important feature that has been linked

to grading. For example, Andreou *et al.* looked at primary, localized, high-grade soft tissue sarcomas and determined that mitotic count (along with the amount of viable tumour remaining post-treatment) strongly correlated with prognosis and could serve as the basis for designing personalized treatments [90].

Pathologists currently obtain mitotic counts manually by optical inspection through a high-powered microscope. Tissue samples are first affixed and stained. Then the number of cells undergoing mitosis is manually counted by identifying morphological features that match the latter part of the cell cycle (e.g. visible chromatid separation, lack of nuclear membrane, hyperchromatic appearance) [91]. Unfortunately, counting mitoses can be subjective and affected by fixation of the tumour tissues, the quality of the section or biopsy, and adequate selection of the most representative areas [92]. As such, it is a tedious and time-consuming task, and has limited reproducibility. Rapid counting also results in errors so multiple recounts are generally required [93]. Therefore a method of objectively quantifying cell proliferation and mitotic events, can be a great benefit for cancer prognosis.

Quantitative image analysis techniques have been developed to address some

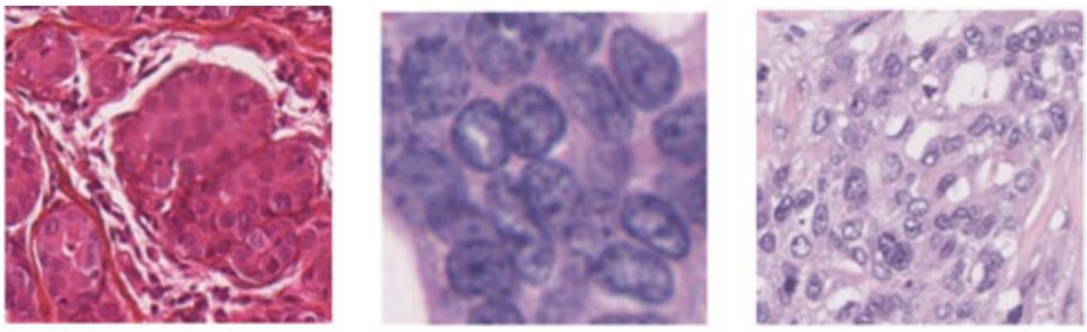

Figure 6.1: Example images of nuclei that are challenging to detect (figure taken directly from [7])

of these challenges. These systems analyse large datasets of stained tissue samples and perform mitosis detection through texture or colour-based feature analysis [94, 95, 96]. More recently, machine learning has been leveraged to undertake this task. They include conventional neural network methods that use manually-engineered feature descriptors for classification [97, 98], along with deep neural networks that are feature-agnostic [99, 100]. However, variations in images during sample staining, the large amount of visible objects, and the similar appearance of mitotic nuclei with non-mitotic structures, make image classification a difficult task [101]. Fig. 6.1 shows examples of nuclei that are challenging to detect.

6.2.2 The Cell Cycle

A second important application for mitosis detection is in the development of targeted chemotherapy regimens. Many modern chemotherapeutic regiments targeting cancer cells focus on disrupting the cell cycle, which is the process by which cells grow and multiply. The cell cycle is divided into different phases that mark cell transitions from resting behavior, to performing DNA synthesis and chromosome separation, and finally division [102]. Checkpoints exist within the cell cycle to ensure only healthy cells proliferate, while detection of defects will trigger a cell cycle arrest. This ensures that any flaws are not passed on to daughter cells when cells undergo division. Disruptions to the progression of this cycle that allow unchecked cell multiplication is a hallmark of cancer cells [103]. As such, modern advances in therapeutics have focused on targeting the cell cycle in cancer cells. Specifically,

anti-cancer drugs have been developed that focus on inhibiting cyclin-dependent kinases (CDKs), which are enzymes required for driving the cell forward through the different phases of the cycle. Furthermore targeting CDKs during certain phases of the cell cycle has shown promise in improving the efficacy of cancer treatment at low dosages that limit non-specific damaging effects on normal cells [103, 104, 105]. Therefore by careful administration of the drug during known phases of the cell cycle, one may be able to improve the efficacy of the drug treatment while reducing required dosages. A real-time cell viability monitor that can identify points in the cell cycle could thus be a useful tool in the screening process.

6.3 Detecting Morphology Changes

Here we propose an alternative approach to detect mitotic events: monitor changes in cell morphology through cell-substrate binding measurements. The basis for this approach is due to the acute changes in cell shape and size that occur during the final phase of the cell cycle, cytokinesis, when a cell divides. The parent cells membrane contracts, causing the cell to round and decrease its footprint over the substrate. A contractile furrow forms and pinches at the cells equator, eventually dividing the cell into two daughter cells [102]. These new cells then begin adhering and spreading out onto the substrate. These changes in morphology affect the capacitive coupling at the cell-substrate interface which can then be detected through capacitance measurement.

6.4 Mitosis detection algorithms

Two mitosis event detection algorithms were compared, one based on a moving average indicator, and the other based on template matching.

6.4.1 Kaufman Adaptive Moving Average

The Kaufman adaptive moving average (KAMA) algorithm [106], originally developed as a financial indicator, is used to generate a capacitance indicator curve. For each data point x_i, we find the absolute difference, d_i, with the capacitance value W points prior (x_{i-W}), where W is the length of the averaging window, as given by Equation 6.1. The volatility of measurements within this window, v_i, is computed by summing the difference between successive data points in the window, as given by Equation 6.2.

$$d_i = |x_i - x_{i-W}| \tag{6.1}$$

$$v_i = \sum_{n=1}^{W} (|x_{i-n+1} - x_{i-n}|) \tag{6.2}$$

The ratio of d_i and v_i is then scaled by parameters α and β, to generate a smoothing constant SC_i, as given by Equation 6.3. The smoothing constant is then used to scale the difference between the raw capacitance value and prior KAMA value, as given by Equation 6.4. The result is an exponentially weighted moving average indicator (MAI) that smooths over transient fluctuations in capacitance and tracks behind larger swings. This means that a crossover of the raw sensor output with the KAMA line (i.e. the data crosses below the KAMA line) is indicative of

a directional shift in the data. It follows that the opposite crossover (i.e. the data crosses back above the KAMA line) then indicates an end to the shift. This feature can be used to mark a mitosis event because during the division, the cells contract and are expected to cause a drop in capacitance as surface area coverage is reduced. This is followed by a recovery phase where the two new daughter cells re-adhere to the substrate. The time taken for a capacitance drop and recovery is dependent on cell morphology kinetics, therefore events detected through the KAMA-signal crossover points are thresholded using a maximum time, T_{max}, to filter out false positives.

$$SC_i = (\frac{d_i}{v_i}(\alpha - \beta) + \beta)^2 \tag{6.3}$$

$$y_i = y_{i-1} + SC_i(x_i - y_{i-1}) \tag{6.4}$$

6.4.2 Template Matching

Template matching (TPM) algorithms compare the entire recorded signal with a template that is representative of the signal being detected. The metric used to quantify this similarity can be computed in several different ways. Common measures include the Euclidian-distance, cross-correlation coefficient, and the sum of squared difference (SSD). Here the SSD is used to compute the similarity index between raw signal and template, as given by Equation 6.5.

$$SSD_j = \sum_{i=1}^{N}(x_{j,i} - t_i)^2 \tag{6.5}$$

where t is the template with length N, and x_j is the jth window of the raw data being compared to the template. If the template matches the window of the raw signal identically, then the SSD value will be zero; slight differences between data points will shift the SSD upwards. Therefore, after computation of the SSD metric, a threshold is applied to identify detected events. In this dataset, the template was created using the time-aligned median of five sample marked events.

6.5 Experimental Results

6.5.1 Mitotic Activity Detection

Fig. 6.2a shows examples of cells dividing at a single sensors electrodes. The bottom panel shows the measured capacitance over a period of 60 hours. The top panel shows three pairs of images of the sensor and surrounding area at specific time points indicated by the square and circle markers. In this example, three occurrences of division took place at the same sensor, each of which are highlighted in the capacitance time-series data. The square and circle symbols mark when images were taken and show cells before and after division occurs, respectively. During each division the parent cell begins to contract, reducing its surface area in contact with the electrode and causing a reduction in cell-substrate coupling. This effect can be seen in the sensor readings as the downtrend of > 50 aF that occurs over a period of roughly 60 minutes. The cell then divides into daughter cells, which then expand and settle over a larger area of the electrodes. This process in turn increases the measured capacitance. Fig. 6.2b shows manually verified mitosis

events for a single experiment for multiple sensors.

Analysis of the detected events can be performed to elicit cell division kinetics.

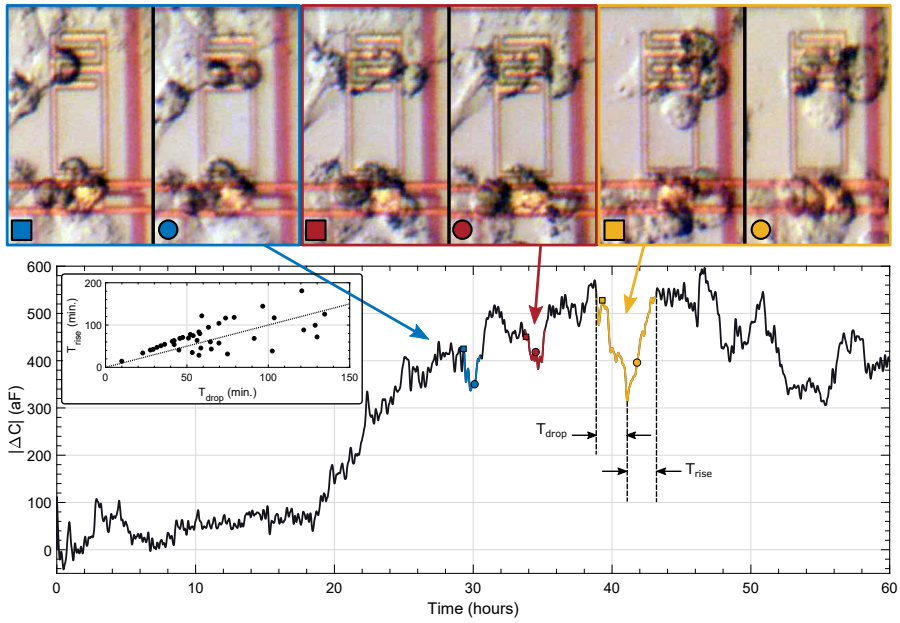

(a)

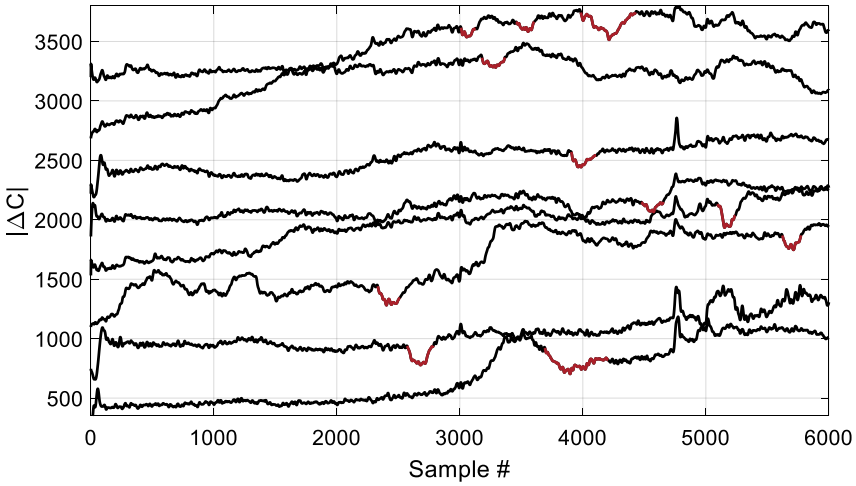

(b)

Figure 6.2: a) Top: Images taken of a sensor at different time points. Bottom: Corresponding sensor response showing the measured capacitance changes over time. The highlighted portions indicate division events marked by the detection algorithm. Inset: Distribution of the time taken from start of division event to reach minimum capacitance (T_{drop}) and time taken to recover (T_{rise}). $N = 41$ detected events. b) Examples of detection mitosis events from one experiment. Capacitance traces have been offset for plotting purposes. Video is available as supplementary material.

Using the measured data we extract the time taken from the detected start of an event to the time at which a minimum capacitance is detected within the events period (T_{drop}). This indicates the portion of the division cycle where the contractile ring causes the cell to shrink and round. The corresponding recovering time (T_{rise}) is the time for the daughter cells to adhere and re-spread causing a rebound in sensed capacitance. The inset of Fig. 6.2a shows a scatter plot comparing T_{drop} and T_{rise}. Each point corresponds to a division event that was automatically marked using the detection algorithm, and manually verified with time-lapse imaging ($N = 41$). The dotted line has a slope of 1, as a reference. The majority of the drop and recovery phases range between 20 and 100 minutes but interestingly show a roughly linear time correspondence with the recovery phase taken slightly longer than the corresponding drop phase. In fact, one might expect the recovery phase to take significantly longer since daughter cells are rounded immediately following mitosis and have to re-establish cell-substrate adhesion, a situation similar to cells making initial attachments to their substrate. However, recent research in cell-substrate adhesion during mitosis has revealed the existence of remnant adhesion molecules that aid in post-mitotic daughter cells to re-spread and anchor to the substrate[107, 108]. This may help explain the relatively quick recovery of the measured binding capacitance.

Each sensor electrode covers an area of 30×30 μm^2 which means a total sensing area of 0.0144 mm^2 across the array. A total of 41 manually verified mitotic events were detected across four experiments, resulting in a mean mitotic figure of 710 divisions/mm^2 across the four experiments. This figure is significantly higher

than typical counts of < 15 divisions/mm^2 [92, 109], primarily because typical image-based counting methods are based on analysing tissue samples extracted at a fixed point in time. Here the count index reflects divisions that occur across a period of three days and thus show a fuller picture of cancer cell activity. If the time period of 72 hours is taken into consideration, the scaled figure would be 9.9 divisions/mm^2/hr, which is within the typical range for histological grading.

6.5.2 Detection Algorithm Performance

In order to develop the sensor as a tool for counting mitotic figures, we evaluate the two detection algorithms for specificity and sensitivity. Receiver operating characteristic (ROC) curves were generated for each algorithm using the manually marked dataset as ground-truth. For the TPM algorithm, the SSD threshold was varied to generate the true positive rate (TPR) and false positive rate (FPR) of the detected events. For the MAI algorithm, the maximum time span between crossover points (T_{max}) is varied to generate the ROC points. Fig. 6.3 shows ROC curves for the two algorithms. The dotted line indicates the random guess boundary; better performing algorithms would be in the upper half of the boundary and ideally following along the y-axis (high TPR and low FPR) before saturating near a TPR of 1. At stringent threshold levels, the TPM algorithm outperforms MAI with a consistently better TPR. When the threshold is relaxed to allow more detections, MAI begins to outperform TPM, starting at an FPR of roughly 0.25.

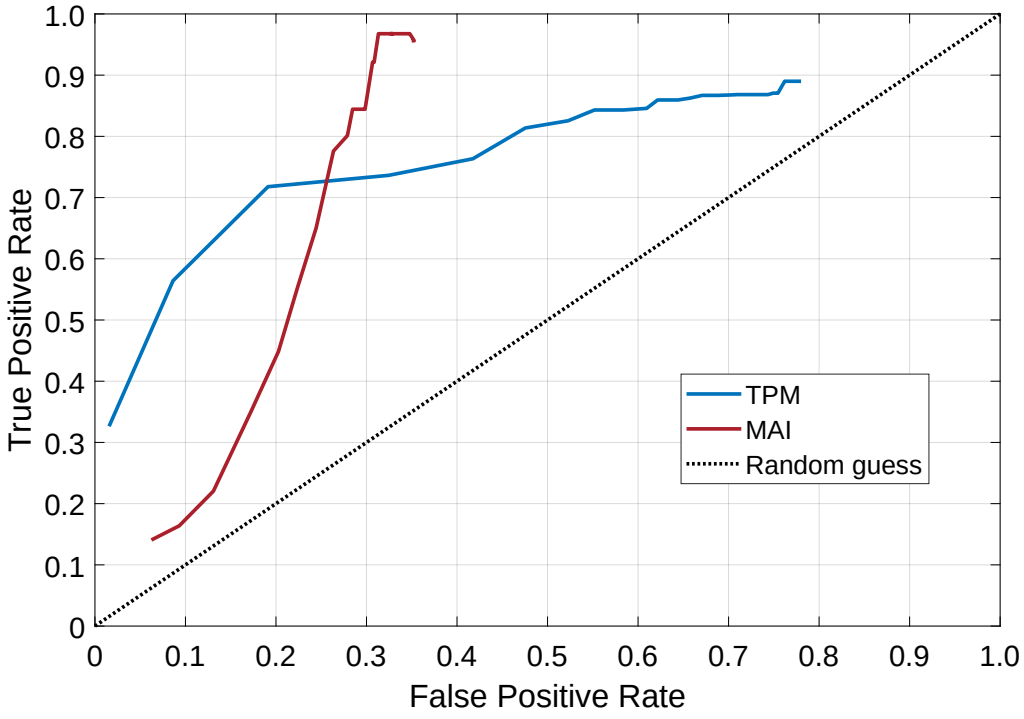

Figure 6.3: Receiver operating characteristic curve for cell detection algorithm. The two lines correspond to varied minimum capacitance changes and durations for mitotic events.

Chapter 7

Applications, Part 2: Drug Screening on Chip

7.1 Preface

Here we presnt work for using the capacitance sensor chip as a proof-of-concept tool for monitoring chemotherapeutic agent potency in cancer cells. Drug-sensitive and drug-resistive cells are cultured on the LoCMOS device and are exposed to cisplatin, a platinum-based cancer drug. Results show the ability to discriminate cell lines using capacitance sensor measurements. The data is then used to extract cell death kinetics.

This chapter includes excerpts of a manuscript that has been submitted to Biosensors and Bioelectronics, an article that was authored by myself, Sheung Lu, Dr. Marc Dandin, Dr. John Basile, Dr. Elisabeth Smela, and Dr. Pamela Abshire. My contributions include setting up and performing the experiments, data processing, analysis of cell death kinetics, and most of the writing.

7.2 Cell-Based Drug Screening Assays

Cell-based assays are a vital tool in the drug discovery process and can be used to quantify the cytotoxic effects of drugs on cells and identify new targets for drug development. As mentioned previously, most current cell-based screening

studies require the use of specialized laboratory equipment and reagents, and provide data through methods that require labeling such as fluorescent, bioluminescent, and colorometric methods. While these methods can provide high-throughput analysis through parallelization of experiments, they generally have high operational costs, can be labor intensive, require sub-sampling of analytes, and may lack specificity [110]. Furthermore most conventional methods provide data at sparse sampling points or are endpoint assays, and so do not provide information on the dynamics of cell growth.

Real-time monitoring of cell viability over the course of drug exposure and subsequent cell death may provide a more complete picture of the cytotoxic effects of drugs, enabling the development of a more precise drug dosage regimen. Indeed modern chemotherapeutic regimes generally involve the use of multiple drugs [111] administered sequentially or in an alternating fashion, with the aim of reducing drug resistance, reducing non-specific toxic effects, and maximizing overall efficacy. Computational models have also been developed to generate adaptive therapeutic [112] regimes or select optimum strategies to address issues of tumor heterogeneity [113]. Therefore the ability to perform continuous cell measurements in real-time would represent a great advance over current methods of determining drug cytotoxicity and cancer cell susceptibility, replacing current laboratory assays with a more rapid and more relevant alternative that could hasten the drug development process toward clinical implementation.

Most chemotherapeutic agents are designed to induce cell death through a process called apoptosis, or programmed cell death. This is a regulated process that

causes the nucleus to condense, organelles to pack together, and cell to shrink in overall area [20]. This change in morphology is thus an attractive candidate for observation through real-time cell-substrate capacitance measurements.

7.3 Cell Response to Chemotherapeutic Agents

Cisplatin, a widely used platinum-based chemotherapeutic drug, was used as the anti-cancer agent. The agent was obtained in dry powder form (BioVision) and prepared with DI water to create a 1 mM stock solution. The solution was stored at room temperature away from light. Human ovarian cancer cell lines A2780 and CP70 were prepared following the protocol described in Section 4.3. For treatment, cells were plated into the device and allowed to grow for 48 hours before the chemotherapeutic agent was administered directly into the cell growth well.

The top panel of Fig. 7.1 shows exemplar images of cells in the vicinity of two sensors through a drug administration experiment. The left-most image, taken at t = 26.8 hours shows cells growing normally. The 100 μM dose of cisplatin was administered at t = 53.5 hours, indicated by the red line, and the second image shows the surface 6 hours later. Cells still appear healthy although a downtrend in the measured binding capacitance can be observed in the sensor data traces. Roughly 4 hours later, a more noticeable change in morphology of the cells can be seen, both in the images and data. The bottom panel of Fig. 7.1 shows the corresponding data from each of the two sensors. Capacitance decreases of 230 aF and 440 aF are measured in channels 1 and 2, respectively. Images of the chip surface show that the

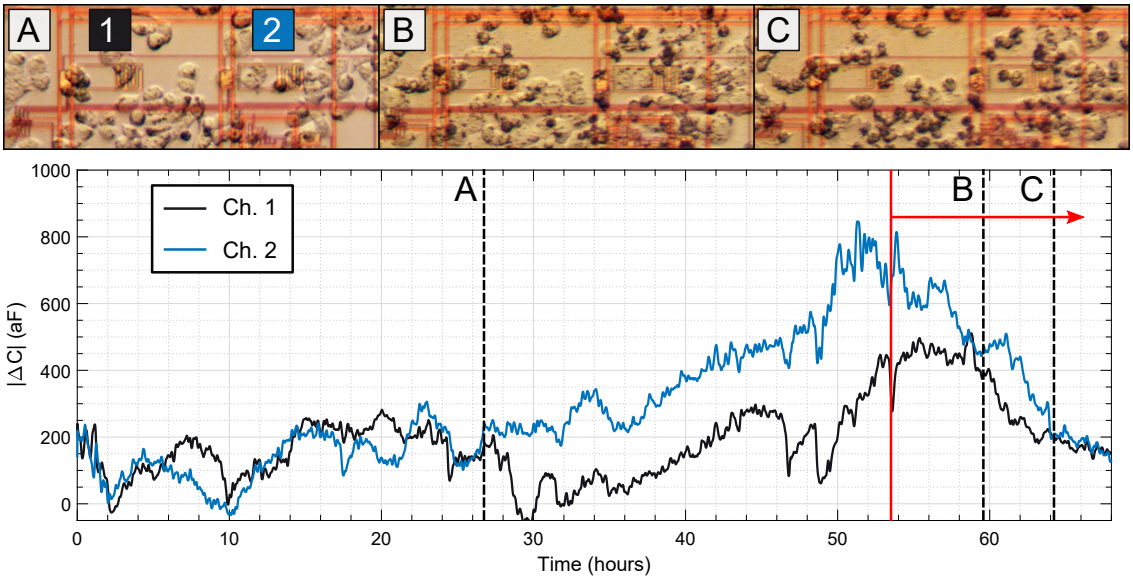

Figure 7.1: Top: Microscope images of the two sensors during a drug administration experiment. Bottom: Corresponding sensor measured capacitance changes over time. The cisplatin was added at t = 53.5 hours, indicated by the red line and arrow. The labels on the images correspond to the time points marked by the dashed vertical lines. Video is available as supplementary material.

cells appear noticeably shrunken and rounded, which is indicative of cell death [20]. This experiment shows the devices ability to track cell health in real-time through a drug-screening experiment.

We then investigated dose-dependent effects of cisplatin on the two cell lines. Each cell type was allowed to grow for at least 48 hours, after which different concentrations of cisplatin were applied. Control experiments were performed in which both cell lines were plated and allowed to proliferate unencumbered over the experimental period. Fig. 7.2 shows the time-series capacitance measurements of the device as a function of drug dose. Each trace shows the mean response of those sensors in the array that were visually observed to have cell coverage. Sensors that were void of cells, due to the random initial seeding, were omitted. The red and black lines correspond to the cisplatin-sensitive (A2780) and cisplatin-resistive (CP70) cell

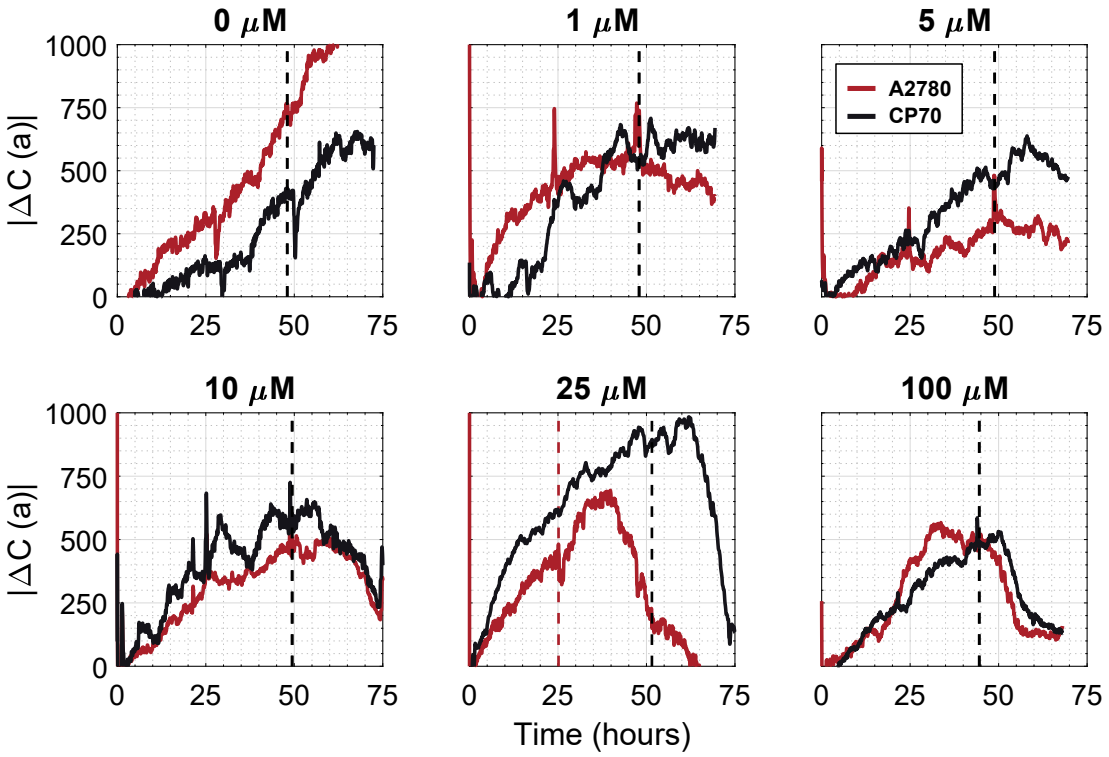

Figure 7.2: Mean capacitance sensor responses for various concentrations of applied drug. Each chart shows the response for two cell types, A2780 (drug-sensitive), and CP70 (drug-resistive). The dashed lines indicate when the drug was applied to the cell culture. In the control experiment both cell lines were viable through the experiment. Addition of 1 μM cisplatin showed an immediate effect on the capacitive coupling of A2780 cells while CP70 cells remained stable. Higher concentrations began to induce a response in CP70 cells as well.

lines, respectively. The dashed black lines indicate the time at which the drug was administered.

The time-series data shows how drug dosage affected cell viability. As expected, the control experiment showed a continual increase in measured capacitance as cells proliferated without damage. At the same time, for high dosages, both cell lines were observed to be adversely affect. As drug concentration was reduced from 100 μM, the net effect diminished. At a concentration of 1 μM, the resistant CP70 line was seen to be relatively unaffected by the drug whereas the sensitive A2780

line showed a downtrend. This observation was confirmed by imaging the surface after the experiment was completed. The difference between the two responses can be highlighted by looking at the net change in measured capacitance from the time of drug application and 24 hours later. The resulting chart is shown in Fig. 7.3. There was a net positive change in signal for the CP70 line for drug concentrations up to 5 μM, although the magnitude decreased with increasing concentration. At the same time, the A2780 line showed an immediate decrease in viability with a 1 μM cisplatin dosage. At a concentration of 10 M, both cell lines were affected, as mentioned previously.

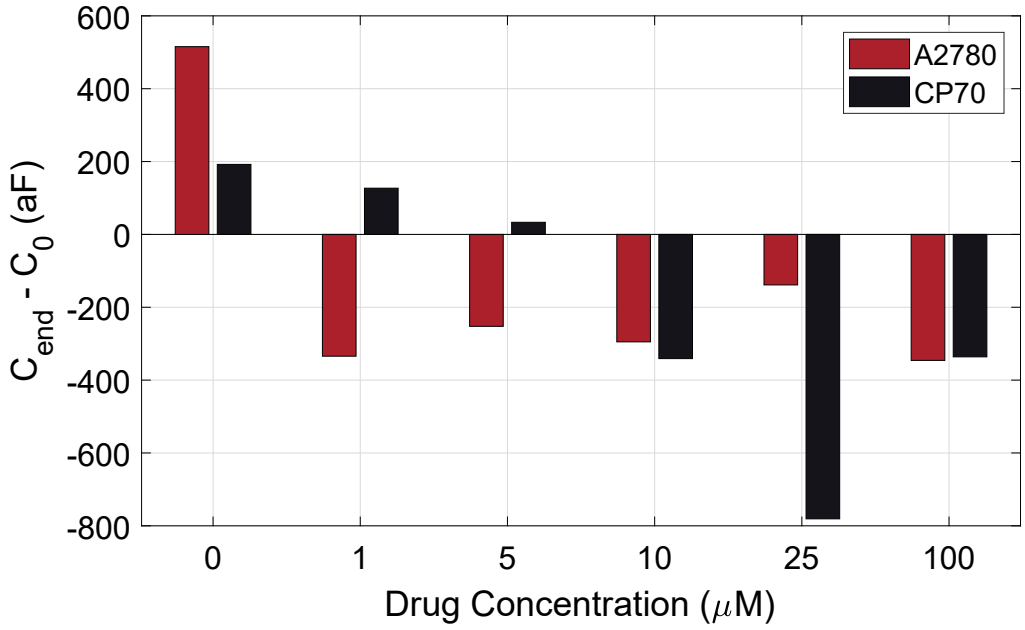

Figure 7.3: Measured difference in average capacitance from immediately after the drug was administered to 24 hours afterwards.

7.4 Cell Death Kinetics

We analyze the high-resolution data provided by the device to profile the temporal response of the cancer cells to cisplatin. The kinetics of cell death are characterized by the time delay between exposure to the drug and the onset of cell death (t_D), and the rate at which cell death occurs (r_D). The onset of cell death was extracted from the capacitance measurements by finding the time at which the peak capacitance value (C_D) occurs, after the application of the drug. The capacitance curves were then normalized to C_D and the data was fitted to an exponential decay model:

$$C(t) = \frac{\Delta C(t)}{C_D} = C_0 \exp(-r_D t) + C_B \tag{7.1}$$

where t (hr) is time, r_D is the decay time constant (hr^{-1}), C_0 and C_B are initial and baseline values, and $C(t)$ is the normalized capacitance as a function of time.

Cells were cultured as described previously and exposed to 25 and 100 μM dosages of cisplatin, concentrations that were previously confirmed to be lethal to both cell lines. Fig. 7.4a shows the normalized capacitance measurements of two sensors from experiments where A2780 and CP70 cell lines were exposed to 25 μM of cisplatin. For clarity, the measurements from the start of cell culture up to the time at which drug is administered are omitted. Additionally, the data is time-aligned such that the onset of cell death occurs at $t = 0$ hrs. Therefore t_D is the time span between the first data point and $t = 0$ hrs, as indicated by the horizontal arrows. Fig. 7.4b shows the corresponding plots for a dose level of 100 μM. The dashed

lines in both figures are the fitted exponential decay models for each trace. Fig. 7.4c shows the mean t_D for each dosage and cell line. As can be seen, there is a significant decrease in the time to onset of cell death when drug dosage is increased from 25 to 100 μM ($p = 0.003$ and $p = 0.004$ for A2780 and CP70 cells, respectively). Fig. 7.4d shows the mean r_D values. No significant difference in the decay time constant was seen as a function of drug concentration ($p > 0.05$). Interestingly, this parameter is higher for the resistant CP70 cell line compared to the sensitive A2780 line.

Drug delivery in these experiments involved dispensing microliter volumes of the drug into a relatively large well, so drug exposure relied primarily on diffusion

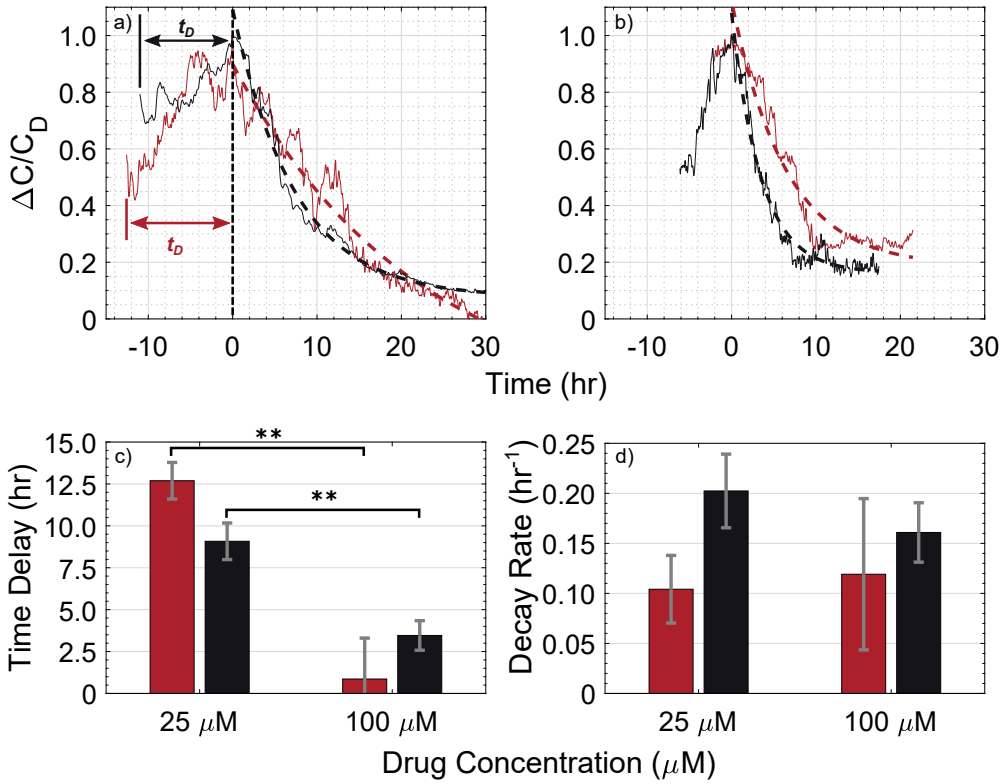

Figure 7.4: Normalized capacitance values vs. time for experiments where cells were exposed to drug concentrations of a) 25 μM and b) 100 μM. The bottom panel shows the mean extracted a) time delay and d) decay time constant for the set of experiments. ($**p < 0.01$)

through the cell media. As mentioned previously, microfluidics could be incorporated into future versions of the device in order to better control dosage. With channels running across the sensing area, one could precisely control flow rates to maintain a constant drug level. Additionally, exposure times could be controlled, allowing for evaluating different dosage regimens with multiple drug combinations. Furthermore, drug dispensing could be regulated by incorporating cell cycle marker detection, creating a feedback control loop for automated cell cycle-targeted drug screening therapies.

7.5 Summary

This chapter presented results of *in vitro* experiments to monitor chemotherapeutic agent potency in cancer cells in real time, using a CMOS capacitance biosensor. Experiments were performed to examine the effects of a chemotherapeutic agent on drug-sensitive and drug-resistant human ovarian cancer cell lines. The capacitance measurements were used to extract parameters of cell death kinetics and showed changes in the time to the onset of cell death as a function of drug concentration. Results additionally showed successful discrimination of the sensitive and resistant cell lines, and confirm the biosensor as a proof-of-concept tool that has potential to hasten the drug development process.

Chapter 8

Conclusions

8.1 Summary

In this dissertation, we presented a CMOS-based capacitance sensor for on-chip cell monitoring with high-resolution measurement capabilities to perform single cell analysis. The sensor was specifically designed with simplicity, robustness, and ease-of-use in mind. The chip uses the capacitance-to-frequency based sensing paradigm that alleviates the mismatch and baseline offset issues that affect other approaches, as discussed in Section 2.2.5. A more thorough validation of the sensor was then explored. We developed a platform to perform time-lapse microscopy of cells on the sensor surface over multiple days of experiments. The high-resolution images that the system provides, allows for validation of sensor responses and confirmed the sensor's capability to detect changes in individual cell morphology. Finally, we performed proof-of-concept drug screening experiments as a first step in validating the system for use in real-world applications. to characterize the potency of chemotherapeutic drugs on cells.

This chapter outlines some of the outcomes that this work has produced to advance the field of biological cell monitoring forward. A comparison of state of the art is presented, discussing traditional laboratory techniques, lab-on-CMOS approaches, and the improvements made in this research. A discussion of future extensions and

applications is then presented.

8.2 Comparison to State of the Art

8.2.1 Cell-based Assays

As discussed in Section 2.2.2, there are a number of methods currently used in industry for monitoring cells. These techniques are primarily based on optical detection methods and generally rely on labeling cells with a marker that is indicative of a characteristic of the cells. For instance Alamar Blue, a commonly-used reagent, contains a non-fluorescent compound called resazurin that is reduced through the metabolic activity of healthy cells to generate a fluorescent compound called resorufin [114]. Cells are first incubated with the reagent for 1 to 4 hours and then a spectrophotometer is used to quantify the fluorescence intensity, which is then correlated to cell viability [115]. A diagram showing the assay procedure is shown in Fig. 8.1.

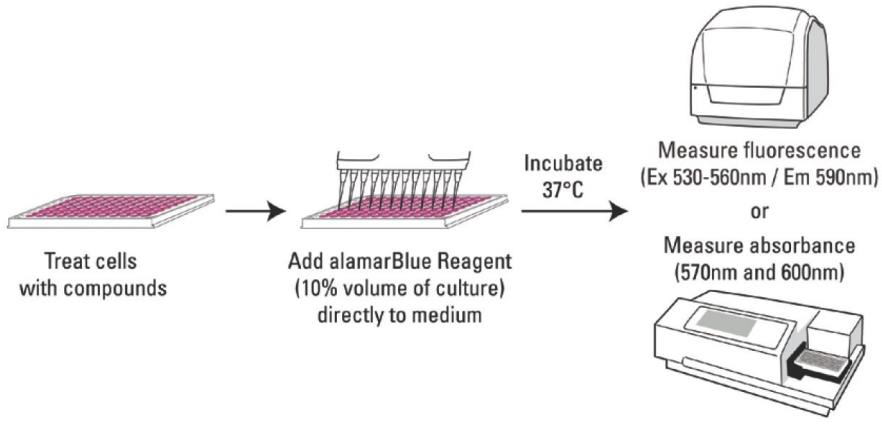

Figure 8.1: Alamar Blue assay procedure. Figure from [8]

While these types of methods can be performed in a high-throughput manner using multi-well plates, the quantification step can only be performed at discrete time points (generally at the end of an experiment — an endpoint assay) and so do not provide high temporal resolution data. This eliminates the opportunity to track fast changes and to determine temporal correlation between measurements. Furthermore, performing the assays themselves can be labor-intensive, time-consuming, and require access to large laboratory equipment. Therefore it is important to develop new techniques to perform these measurements.

8.2.2 CMOS Capacitance Sensors

Several CMOS capacitance sensors have been developed over the years for monitoring cells that have been tested in vitro. Prakash *et al.* implemented CS and differential CBCM designs for characterizing cell adhesion [18, 19, 9, 43, 45] and presented measurements of muscle cells and cancer cell lines. Ghafar-Zadeh *et al.* used a CBCM structure to monitor the growth of bacteria in medium [44]. Nabovati *et al.* used a differential CBCM structure for cell monitoring [25], extended the design to an 8×8 array [12], and more recently performed drug cytotoxicity experiments on chip [11]. Laborde *et al.* developed a 256×256 "nanocapacitor" array using the CBCM approach that was able to track changes in cell morphology in real-time [13, 116]. Couniot *et al.* developed a 16×16 array of CBCM sensors and a multi-electrode CTF oscillator sensor, both used for detecting bacterial cells [10, 48]. Section 2.2.5 presented discussion of trade-offs of the different architectures

used in these devices. Here we discuss the outcomes of this work with respect to these existing systems.

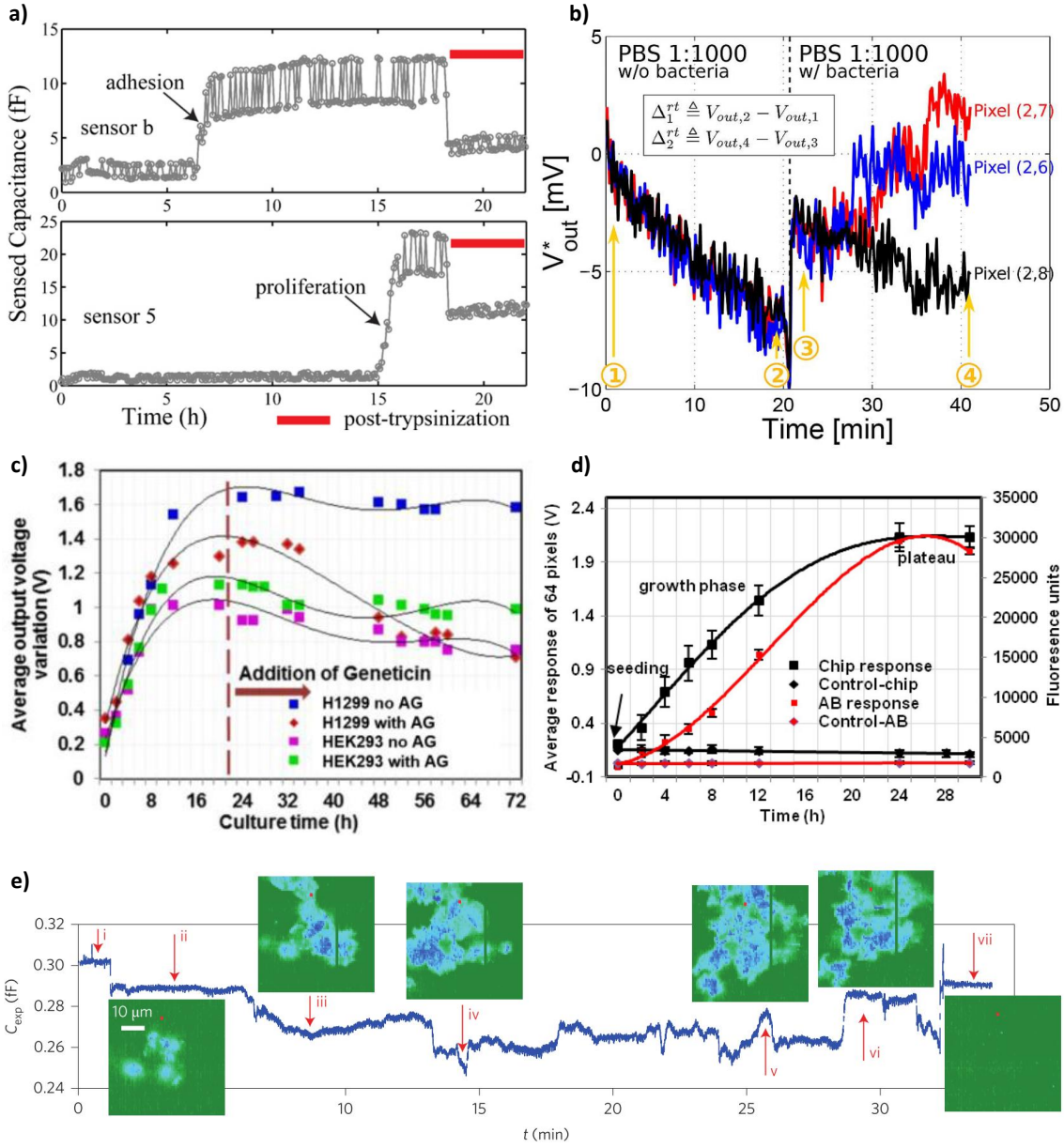

Figure 8.2: Example plots of data from CMOS-based capacitance sensors used for *in vitro* experiments. Images taken from a) Prakash *et al.* 2008 [9], b) Couniot *et al.* 2015 [10], c) Nabovati *et al.* 2018 [11], d) Nabovati *et al.* 2017 [12], e) Laborde *et al.* 2015 [13]

8.2.3 Capacitance Resolution

One of the key challenges in monitoring cells using a lab-on-CMOS platform is the sub-femtoFarad resolution required to detect changes in the cell-substrate capacitance. And as shown in this work, single cell analysis requires even higher resolution — <100 aF to detection mitosis events, for example. Several of the aforementioned research groups have presented *in vitro* measurements of the sensors, as can be seen in Fig. 8.2.

Panel (a) (Prakash *et al.*) shows capacitance measurements from two sensors during an experiment with MDA-MB-231 breast cancer cells. Cells were allowed to proliferate over a period of 17 hours and then were detached from the sensor surface (trypsinization) [9]. As can be seen there is a marked response once cells start to adhere well to the surface of the chip and a corresponding response when they are detached. However, the signal fluctuates by ∼5 fF which can make it difficult to see single cell events.

Panel (b) (Couniot *et al.*) shows measurements of three sensors as a 10 μL drop of solution containing *S. epidermidis* bacterial cells is pipetted onto the chip at $t = 20$ min. As can be seen there are different time evolutions of the three signals, and these are attributed to different numbers of bacterial cells at each location. The authors were able to quantify sensitivity using microscope images and obtained a figure of 2.2 mV/bacterium. However, due to reported baseline noise levels of 5 mV, the resolution of the sensor is limited to 450 aF. One thing to note is that the target application specifically involved bacteria detection, as opposed to animal cells which

are > 10 times larger in size.

Panels (c) and (d) (Nabovati *et al.*) show mean sensor responses in a cell proliferation experiment (d) and cytotoxicity assay (c). The proliferation experiment showed an increase in output voltage that was positively correlated with fluorescense measurements, along with corresponding negative controls. The cytotoxicity assay involved application of Geneticin, which is a protein synthesis blocking compound, to a Geneticin-resistant (Hek293) and sensitive (H1299) cell line. Reported results showed decreases in the growth rate of H1299 cells, but no significant effects on Hek293 cells. As can be seen the overall population changes can be tracked, but no results were reported on individual sensors which would be required for higher resolution, single-cell analysis.

Panel (e) (Laborde *et al.*) shows the capacitance measurements from a single sensor throughout a cell proliferation experiment, along with a spatial map of responses from the entire 256×256 array at certain time points. Given the $\sim 1\mu$m spatial resolution of the sensors, the authors were able to monitor a single cell from multiple sites with a reported 1 aF capacitance resolution. These results are indeed the best reported figures for CMOS capacitance sensors, and it would be exciting to see additional *in vitro* experiments reported with the device. The main drawback, however, are the complex series of post-processing steps needed to realize the input electrodes array, and the hardware required for readout (discussed in Section 8.2.4).

In this work we have shown the sensor's ability to not only track global cell proliferation, but to also detect single-cell binding events, track cell morphology changes, identify cell division events, and monitor cell motility. These observations

were corroborated with time-lapse ground-truth images of the sensor surface, which has not been previously performed.

8.2.4 System Complexity

One of the major focuses of this work is to develop a CMOS sensor with a simple interface and minimal readout requirements. The minimal electrical connection requirements are needed to facilitate packaging the CMOS chips for fluidic interfaces, which itself is a non-trivial challenge. The number of I/O connections required depends on several factors including external bias requirements, signals for chip control, and the readout interface. In this work we reduced the external I/O requirements to allow full chip control using eight bondpads, which included a test pad. This figure could be iteratively reduced by removing the test pad, implementing an on-chip clock generator, and simplifying the serial readout protocol. As a comparison, the other prior work had no strict focus on minimizing wiring requirements. Instead they relied on wire-bonding, and passivation using an epoxy [11, 10] or polydimethylsiloxane (PDMS) [13, 116] to provide adequate packaging yield. While this may be sufficient to perform preliminary biological experiments, reducing the number of possible failure points in packaging by minimizing electrical connections can be important for mass production applications.

Another important consideration is signal digitization. For traditional CS or CBCM sensors, the output is an analog voltage and so must either be buffered off-chip to an external ADC or converted on-chip. The work presented in [43] and [10]

used off-chip ADCs, which simplified the design but provides a path for the addition of noise into the analog signals. The work presented in [11] and [13] implemented on-chip $\Sigma\Delta$ and cyclic ADCs, respectively. In these systems external hardware (FPGA, digital pulse generator) was required to provide required clocking signals and array readout controls.

In this work, the CTF mechanism is inherently suited for digitization because the output signal is in a digital format. An on-chip counter is used for digitization along with a two-wire serial readout which greatly reduces system complexity and wiring requirements. We also presented system-level architecture improvements to provide a more portable and flexible biosensor by implementing: 1) a customizable integration time to allow for sensing of a large range of analytes, 2) programmable I2C addresses that allows multiple peripherals to run concurrently on the same bus, and 3) spatial scanning of the array controlled with selectable activation/deactivation of individual pixels.

Finally, post-processing requirements are also an important factor in system complexity. In [10] the sensor electrodes were void of the foundry-provided passivation layer, and a thinner 25 nm layer of aluminium oxide was deposited using plasma-enhanced atomic layer deposition. In [12], a thin layer of PDMS was spin-coated onto the chip surface to act as the electrode passivation layer. In [11], a polyelectrolyte multilayer (PEM) film was built up through several incubation and rinsing steps. In [13, 116], the sensor sites themselves are single vias (from the standard CMOS process), and so the chips had to undergo significant processing to build up these vias into "nanoelectrodes". This required several deposition, etching,

and polishing steps [116]. In this work and in [43], no post-processing of the CMOS ICs was necessary, making device integration much simpler and cheaper.

8.2.5 Temporal Resolution and Hardware Interface

The ability to make real-time capacitance measurements throughout multi-day biological experiments in the cell culture environment is critical in order to make a case for using CMOS sensors in lieu of conventional biological assays. Most of the state of the art work presented in Fig. 8.2 meet the sub-minute temporal resolution needed to track cell morphological changes. However in the work that presented experiments where cytotoxic effects of drugs were examined, the measurements are relatively sparse (panel (c), [11]). This may be attributed to the supervised manner in which data had to be collected.

While most of the state of the art capacitance sensor designs operate using the CS, CBCM, or CTF mechanisms, the hardware interfaces needed for chip read-out vary quite widely. The chips may require equipment such as data acquisition cards, FPGAs, source-meters, and digital oscilloscopes. These types of hardware can be cumbersome to transport and maintain in non-laboratory settings, making these systems susceptible to increased noise and interference in clinical settings and ill-suited for applications requiring small form factor devices with simple readout interfaces. In contrast, the design presented here requires only a microcontroller, making it suitable for applications outside the traditional laboratory setting. Table 8.1 presents a summary of existing work.*

*ΔC_{Sensed}: the peak change in capacitance after addition of cells DAC - Digital to analog

converter, DAQ - Data acquisition, DDS - Direct digital synthesizer, DLA - Digital logic analyzer, DO - Digital oscilloscope, FPGA - Field programmable gate array, PC - Personal computer, SM - Source-Meter, μC - Microcontroller

	[18, 19, 9, 43]	[11, 12]	[10]	[116, 13]	[48]	This work.
Method	CS	CBCM	CS	CBCM	CTF	CTF
Tech. (μm)	0.5	0.35	0.25	0.09	0.25	0.35
Array Size	28	8×8	16×16	256×256	1	4×4,4×8
Biospecies	MDA-MB-231 breast cancer	HEK293 kidney, H1299 lung cancer	*S. epidermidis*	BEAS, THP1, MCF7 cancer	*S. epidermidis*	A2780, CP70 ovarian cancer
Readout System	DAQ Card + PC	FPGA + PC	DO + DLA + PC + SM + DC Supply	FPGA + DDS + DAC	μC, DO	μC
Samp. Rate	1 kHz	1 - 100 kHz	37 frames/s	4.5 frames/s	-	0.18 - 45 Hz
ADC	Off-chip	Sigma-Delta	Off-chip	Cyclic	Off-chip	Counter
Sensitivity (mV/fF)	-	320 mV/fF	55 mV/fF	-	-	590 kHz/fF
Res. (af)	135	10	450	1	-	16
Electrode Size (μm^2)	20^2, 30^2, 40^2	50^2	14×16	$\pi 0.09^2$	100^2, 200^2	30^2
ΔC_{Sensed}*	8,12,25 fF	6.6 fF (200 kCells/ml)	310 aF (5 cells at 62 aF/cell)	50 aF	53, 445 aF	1 fF
ΔC_{Sensed}/**Area** (**af**/μm^2)	13 - 20	2.63	1.38	1960	5.3, 11.1	1.10, 1.28

Table 8.1: Biosensors from State of Art

8.2.6 Imaging on CMOS ICs

Imaging cells on chip concurrently with data recording is an important method of validating sensor measurements. Both fluorescence-based [85, 86, 84] and reflective [11, 37] microscopy have been used in prior work to image cells on top of CMOS chips. However the imaging was done at discrete times using standard microscopy and did not achieve the temporal resolution to correlate with real-time cell morphology changes. Furthermore, imaging was performed outside the incubator, which meant measurements had to be interrupted and the cells had to be removed from the controlled culture environment.

In this work the packaged devices were modified to include two wells, one for cell culture and imaging, and the other to allow gas exchange and maintenance of pH levels in media. The in-incubator assembly allowed for high-resolution imaging with the ability to discriminate individual cells in different phases of growth and death. To our knowledge, this is the first time that a CMOS-based sensor has been used and validated concurrently with time-lapse images of the sensor surface.

8.3 Future Work

8.3.1 Increased Spatial Density

A research track that can be extended from this dissertation is an increase in the spatial density of sensors, i.e. a high-density capacitance sensor array. As discussed in Section 3.6, the generation 1 chip consisted of a 4×4 array of pixels

arranged with an X and Y pitch of 196 μm and 186 μm, respectively, and covering an area of an area of 618 $\times$ 588 μm^2. The electrodes themselves are 30 $\times$ 30 μm^2 in size and so the actual sensing area covered by the electrodes is roughly 120 $\times$ 120 μm^2, meaning a fill factor of 4.0 %.

As an immediate goal, the area occupied by each sensor could first be minimized. The presented capacitance sensor consists of the input inter-digitated electrodes and requisite CTF circuitry. Shielding is required to protect the circuitry from ambient light and so one layer of metal is typically dedicated to creating a light shield. In the fabricated chips (which used a 3 metal CMOS process) this was done with M3. That means the area of each sensor is now expanded to include both the electrodes and circuitry. If a process node with more metal layers is available, however, the circuitry itself could be situated underneath the electrodes, with shielding created using a lower metal layer. This would allow bringing electrodes from multiple sensors as close together as possible. One limitation to this would be the fringing effects that would occur from the top-metal layers between sensors that are nearby.

An arrangement of sensors with a high spatial density will allow the creation of larger arrays. An important consideration now would be the readout architecture. Each sensor in the array is scanned sequentially, with a finite amount of time required for each sampling, leading to a linear increase in overall sampling time as the number of sensors increases. The generation 2 and 3 chips developed in this work aimed to address this by including parallel readout of sensors, and random-access selection of sensors, respectively. Additionally, the programmable integration time could be

used to trade off resolution for sampling speed.

8.3.2 Microfluidic Integration

As in many LoC systems, microlfuidic integration is a natural extension to the platform that could expand the capabilities of the sensor for use in scientifically relevant experiments. For instance, microfluidic channels could be fabricated on top of the sensing array to generate a linear or logarithmic gradient of dilutions of chemotherapeutic agents [117, 118]. The capacitance sensor could then be used to explore cytotoxic effects to cells in a high-throughput manner. The drug administration profile could also be given a temporal characteristic (e.g. pulsing or ramping) to investigate effects on cells that would not be possible with traditional laboratory-based cytotoxicity assays. In addition, multiple microfluidic channels could be incorporated to expose cells to a multi-drug dose regimen.

8.3.3 Closed-loop Feedback

Another extension related to microfluidic integration would be to incorporate feedback controls to perform automated drug dispensing, as seen in Fig. 8.3. For instance the capacitance measurements could be automatically analyzed to track proliferation, and once a threshold level is reached, a cytotoxic agent could be dispensed into the culture area through a perfusion system. Furthermore, drug dispensing could be regulated by incorporating cell cycle marker detection in order to perform automated cell cycle-targeted drug screening therapies.

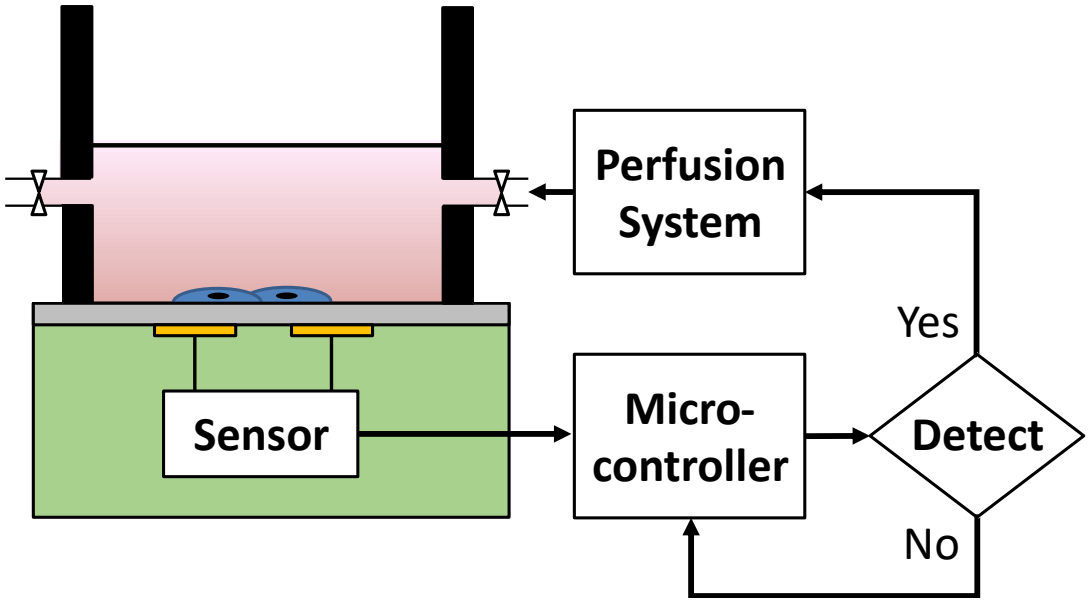

Figure 8.3: Block diagram for a feedback control loop to perform automated drug dispensement.

8.3.4 Sensitivity Improvement

As discussed in Section 3.1, the sensed capacitance at the input electrodes is the series combination of the passivation layer capacitance (C_{PSV}) and the input capacitance of interest (C_{IN}), as given by the following equation:

$$C_{sense} \cong C_0 + \frac{3C_{PSV}C_{IN}}{C_{PSV} + 2C_{IN}} \tag{8.1}$$

where C_0 is the sum of the parasitics giving rise to the baseline capacitance level. Therefore, if C_{PSV} is much larger than C_{IN}, then its contribution to the sensed capacitance will be diminished. In the ideal case where $C_{PSV} \gg C_{IN}$, then the second term of Equation 8.1 reduces to $3C_{IN}$.

One way to increase C_{PSV} is to thin the passivation layer. This could be performed using standard wet or dry etching of the layer, although care must be

taken to stop before the metal electrodes are exposed. To analyze this effect, an FEM model was built and simulated using the structure presented in Section 3.2. Fig. 8.4 shows FEM simulation results of sensed capacitance as a function of cell radius. Panels (a) shows the change in capacitance for a passivation thickness of 1.6 μm, and panel (b) shows the result when the thickness is reduced to 0.8 μm. As can be seen, there is a larger change in capacitance as cell-substrate coupling increases with a thinner passivation layer ($\sim$500 aF vs. $\sim$1000 aF). A linear fit of the data points results in a slope of -23 aF/μm and -59 aF/μm for the two cases, respectively.

Another way to increase C_{PSV} is to increase the dielectric constant of the passivation layer. This can be achieved by first opening holes over the electrodes, either through post-processing or through the CMOS foundry glass cut option, and then depositing a thin film of a high-K dielectric such as hafnium oxide.

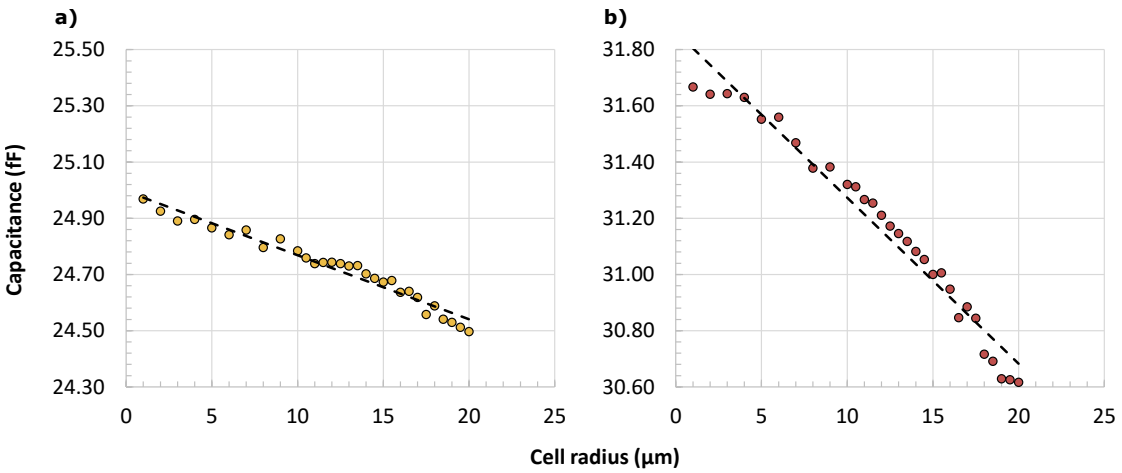

Figure 8.4: FEM simulation results showing the effect of passivation layer thinning on sensed capacitance. The electrode and cell structure presented in Section 3.2 was simulated as cell radius was increased with a passivation thickness of a) 1.6 μm, and (b) 0.8 μm.

8.3.5 Surface Functionalization

The presented CMOS sensor was designed to monitor cell-phenomena through the dielectric changes that they produce at the cell-substrate interface. However, this sensing mechanism can be generalized using labels to detect other biomarkers in an unknown sample solution. For instance, the sensor surface could be functionalized with molecules that are specific towards a target biomarker. When the surface is then exposed to the sample to be interrogated, biomarker molecules in the sample are captured and immobilized close to the sensor electrodes. This could then modulate the dielectric properties at the sensor surface, which can then be detected as a change in capacitance. Therefore, this type of lab-on-CMOS sensor could potentially be used for detection of affinity-based binding of other biomarkers, not just for cell-based assays.

8.4 Applications

8.4.1 Drug Development - Electronic Multi-well Plate

Cell-based assays are the standard diagnostic tools used in the drug development process. In contrast to biochemical assays, cell-based assays offer a more complex model for study that can generate more biologically-relevant information to predict the response of an organism to a particular substance.

Researchers currently perform cell-based assays in multi-well plates that can include 6, 12, 24, 48, or 96 culture wells on one platform to perform multiple ex-

periments in parallel. The type of screening assay depends on a number of factors including the cell type being used, the parameter being measured, chemistry limitations, and the exposure/measurement times involved. However, the process generally works as follows: 1) seed cells into the well plate, 2) add the test agent after a certain growth period, 3) allow any agent-induced effects to occur (several hours to days), 4) add a reagent or marker, 5) measure the response.

The last step is typically done using a multi-well plate reader that can operate using one of several detection methods, including colorimetric, fluorometric, and bioluminsecent mechanisms. However, as discussed in Section 2.2.2, these detection methods are end-point assays. Parallel experiments are needed to obtain a temporal sequence of discrete sample points, and temporal accuracy would be limited by the variability across samples and the sampling technique. Much richer information about the dynamics of cell growth would be available from a real-time measurement methodology.

Therefore the sensor presented in this work could be used as an alternative to traditional multi-well assays. Fig. 8.5 shows a diagram of an "electronic multi-well plate" that can be created using the lab-on-CMOS capacitance sensor chip. Starting with a standard-sized well, a hole can be laser-cut into the bottom of the well to create an opening that is sized to the chip's sensing array area. The chip is then attached to the underside of the well and sealed with a passivation material such as a biocompatible silicone or epoxy. The electronic connections to the chip are made underneath the plate and chips across a single row are all connected together. Multiple rows can then be connected together a single bus line that goes

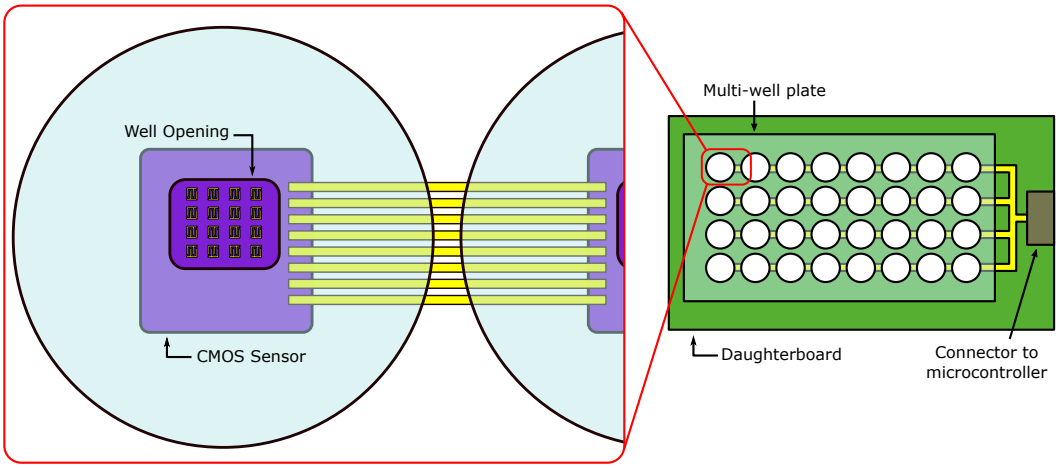

Figure 8.5: Schematic of an "electronic multi-well plate". Each well contains a chip with its sensing area exposed to the cell culture. Electronic connections are made underneath the well plate across columns and rows on a daughterboard. The final routing is wired to a connector that can then be read using a microcontroller.

to a connector port on a daughterboard. This is where the microcontroller readout board is connected.

With this system, researchers can perform the same high-throughput parallel experiments currently performed but glean much more temporally-intensive data due to the real-time measurement capabilities of the capacitance sensor. Furthermore, this obviates the existing need to perform parallel experiments to obtain the temporal profile of cellular responses. A single experiment with the chip/well could replace the multiple experiments required quantify at different time points; for instance if response data is required every hour, this is a 24× reduction over a single day.

8.4.2 Point-of-care Diagnostics and Personalized Medicine

As described previously, the capacitance sensor has potential to be used for detection of affinity-based binding of other biomarkers. This can be explored by performing surface functionalization of the sensor electrodes to target specific analytes. This could then have potential use in point-of-care diagnostic applications, such as at doctor's offices where samples from patients can be analyzed in a high-throughput manner.

The presented cell monitoring sensor could further be used in the emerging field of personalized medicine, where different treatment programs are developed for different patients in order to maximize drug efficacy while minimizing other toxic effects. For instance, tumor cells from a patient can be harvested and cultured on the device, which could then be implanted back in to the patient's body. The chip could then provide real-time viability information about the cancer cells within the patient's body, while they undergo chemotherapeutic treatment. The treatment could then be adjusted for the individual to increase drug efficacy and safety, and enhance patient outcomes.

8.5 Publication Record

8.5.1 Refereed Journal Articles

1. **B. Senevirathna**, S. Lu, M. P. Dandin, J. Basile, E. Smela, and P. A. Abshire, "Real-Time Measurements of Cell Proliferation Using a Lab-on-CMOS Capacitance Sensor Array," *IEEE Trans. Biomed. Circuits Syst.*, vol. 12, no. 3, pp. 510-520, 2018.

2. **B. Senevirathna**, S. Lu, M. P. Dandin, E. Smela, and P. A. Abshire, "Correlation of Capacitance and Microscopy Measurements Using Image Processing for a Lab-on-CMOS Microsystem," *IEEE Trans. Biomed. Circuits Syst.*, 2019. [Accepted]

3. **B. Senevirathna**, S. Lu, M. P. Dandin, J. Basile, E. Smela, and P. A. Abshire, "High resolution monitoring of chemotherapeutic agent potency in cancer cells using a CMOS capacitance biosensor," *Biosensors and Bioelectronics*, 2019. [Accepted]

4. J. Kilpijärvi, N. Halonen, M. Sobocinski, A. Hassinen, **B. Senevirathna**, K. Uvdal, P. Abshire, E. Smela, S. Kellokumpu, J. Juuti and A. Lloyd Spetz, "LTCC Packaged Ring Oscillator Based Sensor for Evaluation of Cell Proliferation," *Sensors*, vol. 18, no. 10, p. 3346, 2018.

8.5.2 Journal Articles in Preparation

1. **B. Senevirathna**, S. Lu, M. P. Dandin, J. Basile, E. Smela, and P. A. Abshire, "Quantifying mitotic activity for cancer prognosis using a CMOS biosensor," *Lab Chip*, 2019. [In preparation]

8.5.3 Refereed Conference Proceedings

1. **B. Senevirathna**, S. Lu, N. Renegar, M. Dandin, E. Smela, and P. Abshire, "System on a Chip for Automated Cell Assays using a Lab-on-CMOS Platform," *IEEE Int. Symp. Circ. Syst.*, 2019.

2. S. Lu, **B. Senevirathna**, M. Dandin, E. Smela, and P. Abshire, "System Integration of IC chips for Lab-on-CMOS Applications," *IEEE Int. Symp. Circ. Syst.*, 2018.

3. **B. Senevirathna**, S. Lu, and P. Abshire, "Characterization of a High Dynamic Range Lab-on-CMOS Capacitance Sensor Array," *IEEE Int. Symp. Circ. Syst.*, 2017.

4. **B. Senevirathna**, A. Castro, M. Dandin, E. Smela, and P. Abshire, "Lab-on-CMOS Capacitance Sensor Array for Real-Time Cell Viability Measurements with I2C Readout," *IEEE Int. Symp. Circ. Syst.*, 2016.

5. **B. Senevirathna**, A. Castro, T. Datta-Chaudhuri, E. Smela, and P. Abshire, "Characterization of an Active Micro-Electrode Array with Spike Detection and Asynchronous Readout," *IEEE Int. Midwest Symp. Circ. Syst.*, 2017.

6. T. Datta-Chaudhuri, **B. Senevirathna**, A. Castro, E. Smela, and P. Abshire, "An active micro-electrode array with spike detection and asynchronous readout," *IEEE Biomed. Circ. Syst. Conf.*, 2014.

7. **B. Senevirathna**, and P. Abshire, "Spatio-temporal compressed sensing for real-time wireless EEG monitoring," *IEEE Int. Symp. Circ. Syst.*, 2018.

8. **B. Senevirathna**, and P. Abshire, "Power Analysis of a Mobile EEG System with Compressed Sensing," *IEEE Biomed. Circ. Syst. Conf.*, 2017.

9. **B. Senevirathna**, L. Berman, N. Bertoni, F. Pareschi, M. Mangia, R. Rovatti, G. Setti, J. Simon, and P. Abshire, "Low cost mobile EEG for characterization of cortical auditory responses," *IEEE Int. Symp. Circ. Syst.*, 2016.

10. N. Bertoni, **B. Senevirathna**, F. Pareschi, M. Mangia, R. Rovatti, P. Abshire, J. Z. Simon, and G. Setti, "Low-power EEG monitor based on compressed sensing with compressed domain noise rejection," *IEEE Int. Symp. Circ. Syst.*, 2016.

Appendix A

Appendix

A.1 Sensor Design Details

The analog voltage used to bias the oscillators is created using an on-chip Beta-multiplier reference circuit (Fig. A.1, [119]). Transistors M1-4 and R form the base Beta-multiplier circuit. M5-8 form a simple amplifier to provide feedback to increase the output resistance of M4. M9-14 form a cascoded current source to generate the required bias level. MS1-S3 form a start-up circuit.

The on-chip control logic was designed to sequentially cycle through all channels in the capacitance sensor array. Fig. A.2 shows a diagram of the finite-state machine implemented on chip generation 3. When the reset signal is pulsed, the chip

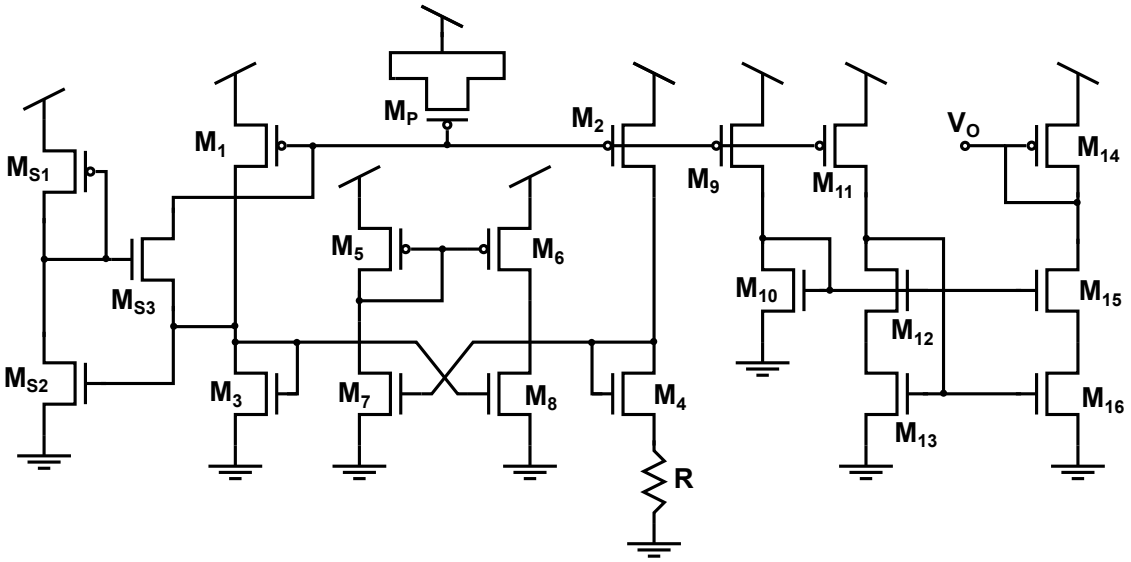

Figure A.1: Circuit schematic of on-chip bias generator.

goes to the IDLE state and INIT states that initialize the internal logic registers. The integration time and active pixel registers are programmed through I^2C. The logic then begins cycling through each pixel in the array. In the the CHECK_PX state where the current pixel is checked to see whether it is active, if not the pixel is skipped (SKIP state).

If the pixel is active, the logic goes into the SCAN state where the oscillator is enabled through row/column decoders and the counter is activated. After the integration time is reached, the logic goes into COLLECT which flags the DRDY signal and loads the counter value into the I2C data registers. An additional CLEAR state is used to allow for data latching and resetting the active pixel tracker. The chip then goes into the TX_WAIT state where it sits idle until an I2C read cycle is performed, after which it moves to the next pixel.

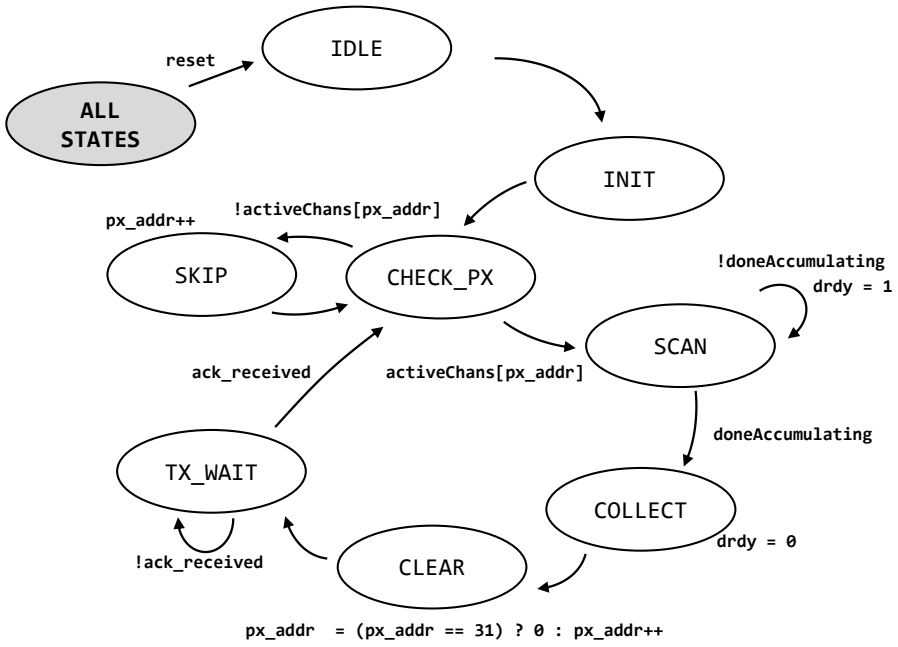

Figure A.2: Finite-state machine diagram of on-chip logic.

Fig. A.3 shows simulation results of the readout timing for a single pixel (the timing has been scaled down for simulation purposes). Each sensor is activated and allowed to start up for a fixed length of time (200 ns), after which the counter is allowed to increment. After the integration time (1 μs), the counter data is latched into the I^{2}C data registers, and the data ready signal is flagged to trigger a read through the microcontroller.

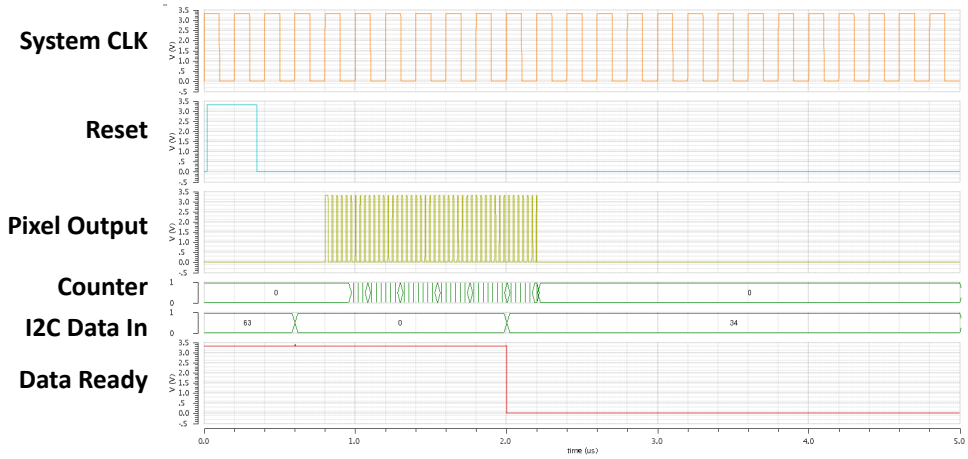

(a)

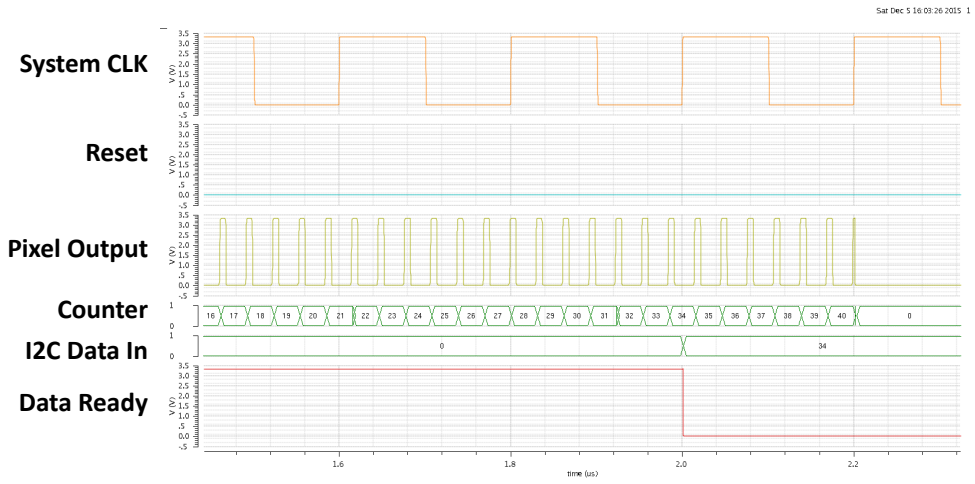

(b)

Figure A.3: Simulation results of logic for readout of one pixel (accumulation time shortened to 1 μs for simulation purposes. The figure depicts a a) full view, and b) zoomed-in view.

A.2 Sample Data

This section presents a few additional examples of data from *in vitro* experiments. Contact Bathiya Senevirathna (bsenevir@umd.edu) or Pamela Abshire (pabshrie@umd.edu) for full dataset, or visit our website (isr.umd.edu/IBIS).

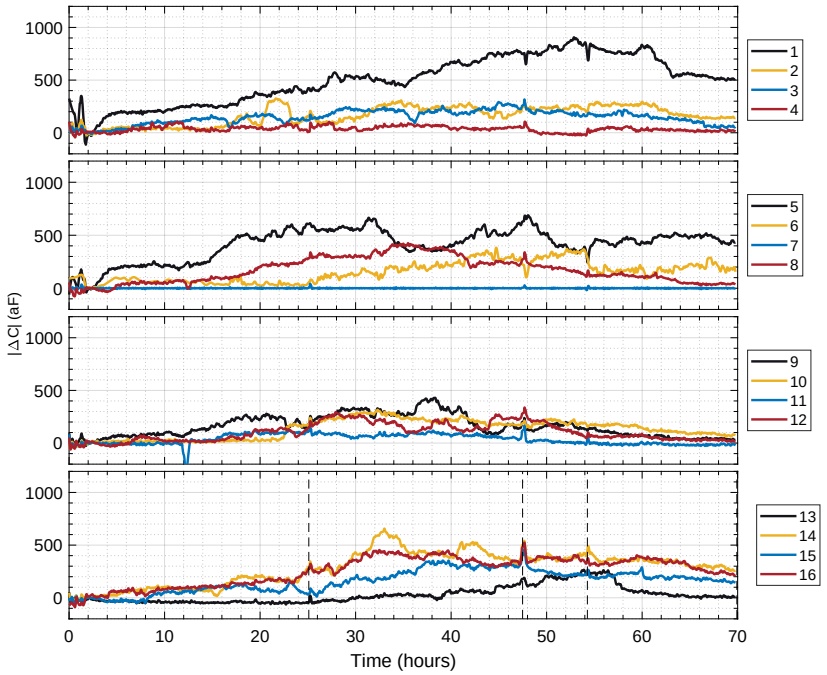

(a)

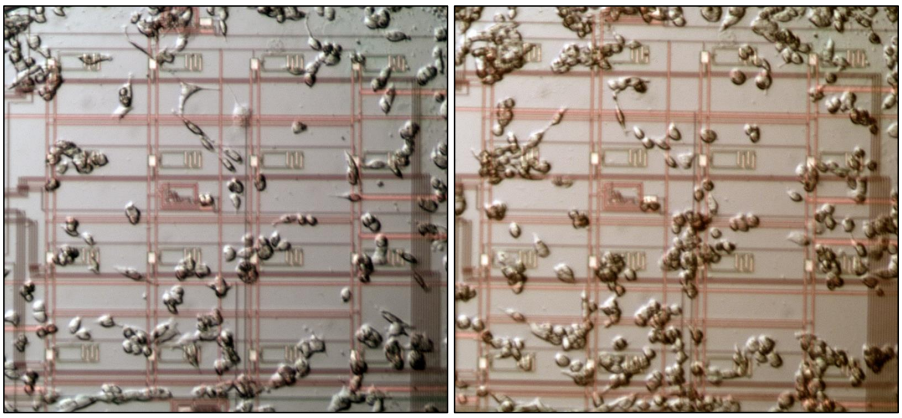

(b) left (c) right

Figure A.4: a) Response curves of the chip as CP70 cells adhere and proliferate across the sensor array. The first two vertical black lines at t = 25 hours and t = 47 hours indicate times when data recording was paused for imaging. Right panel shows image of surface of chip after b) 25 hours, and c) 47 hours.

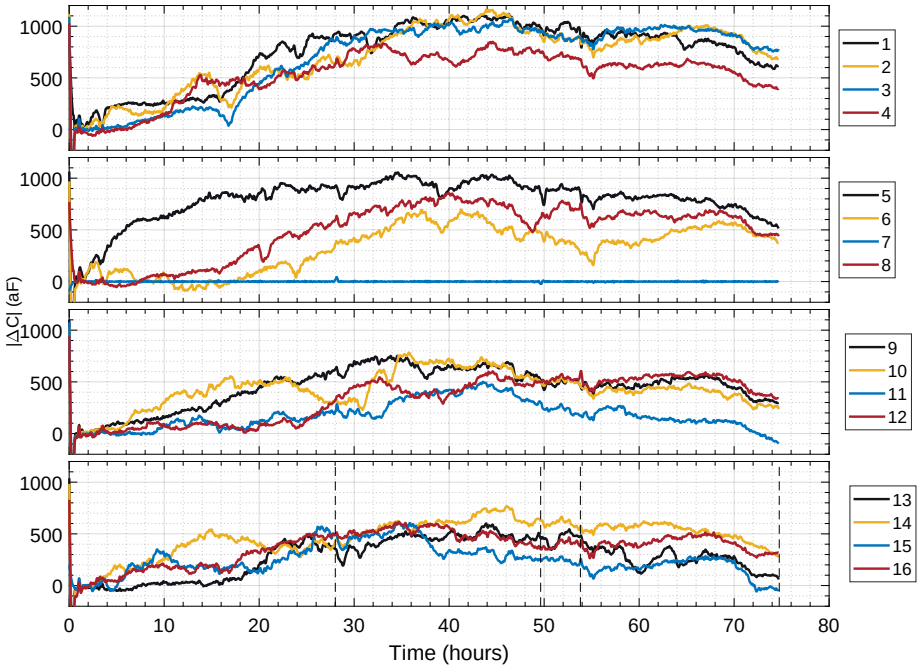

(a)

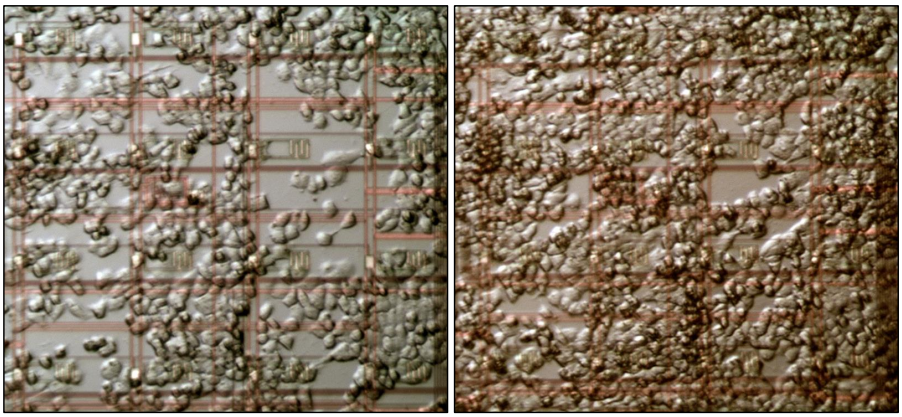

(b) left (c) right

Figure A.5: a) Response curves of the chip as A2780 cells adhere and proliferate across the sensor array. The first two vertical black lines at t = 28 hours and t = 49.5 hours indicate times when data recording was paused for imaging. Right panel shows image of surface of chip after b) 28 hours, and c) 49.5 hours.

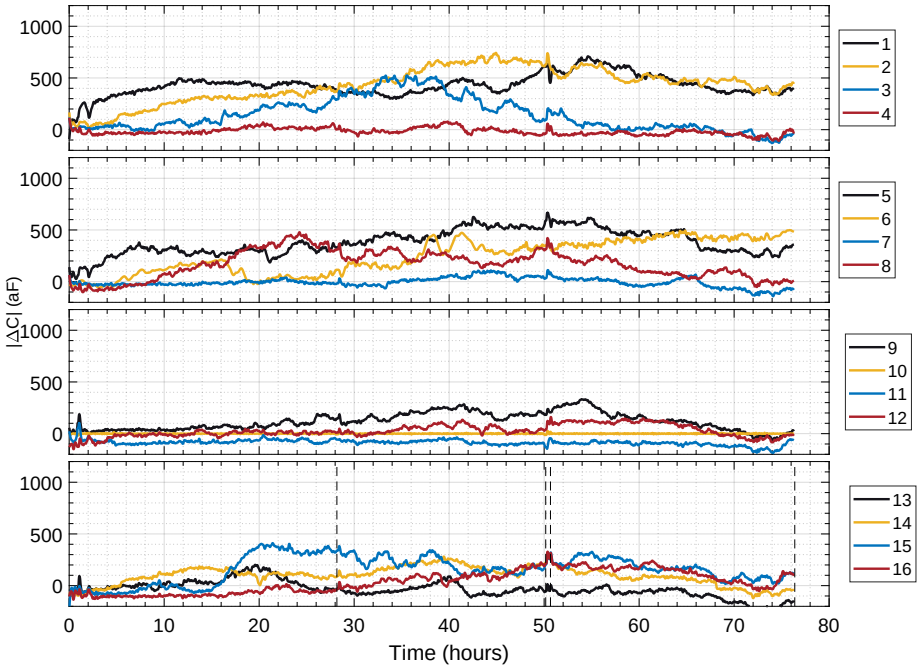

(a)

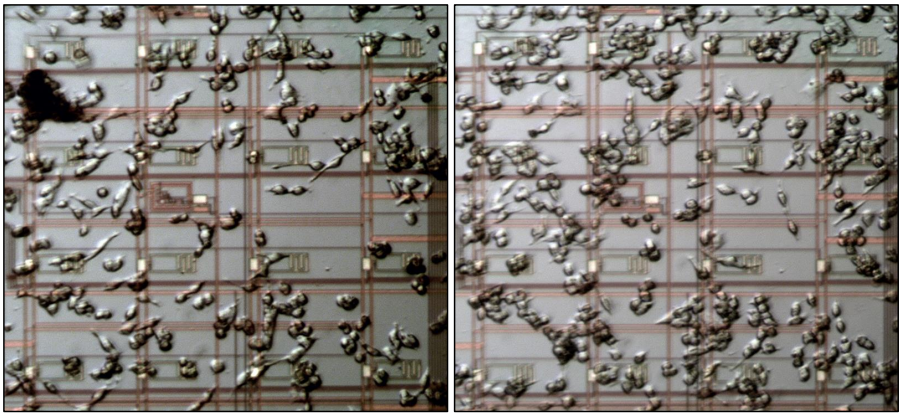

(b) left (c) right

Figure A.6: a) Response curves of the chip as CP70 cells adhere and proliferate across the sensor array. The first two vertical black lines at t = 28 hours and t = 48 hours indicate times when data recording was paused for imaging. Right panel shows image of surface of chip after b) 28 hours, and c) 48 hours.

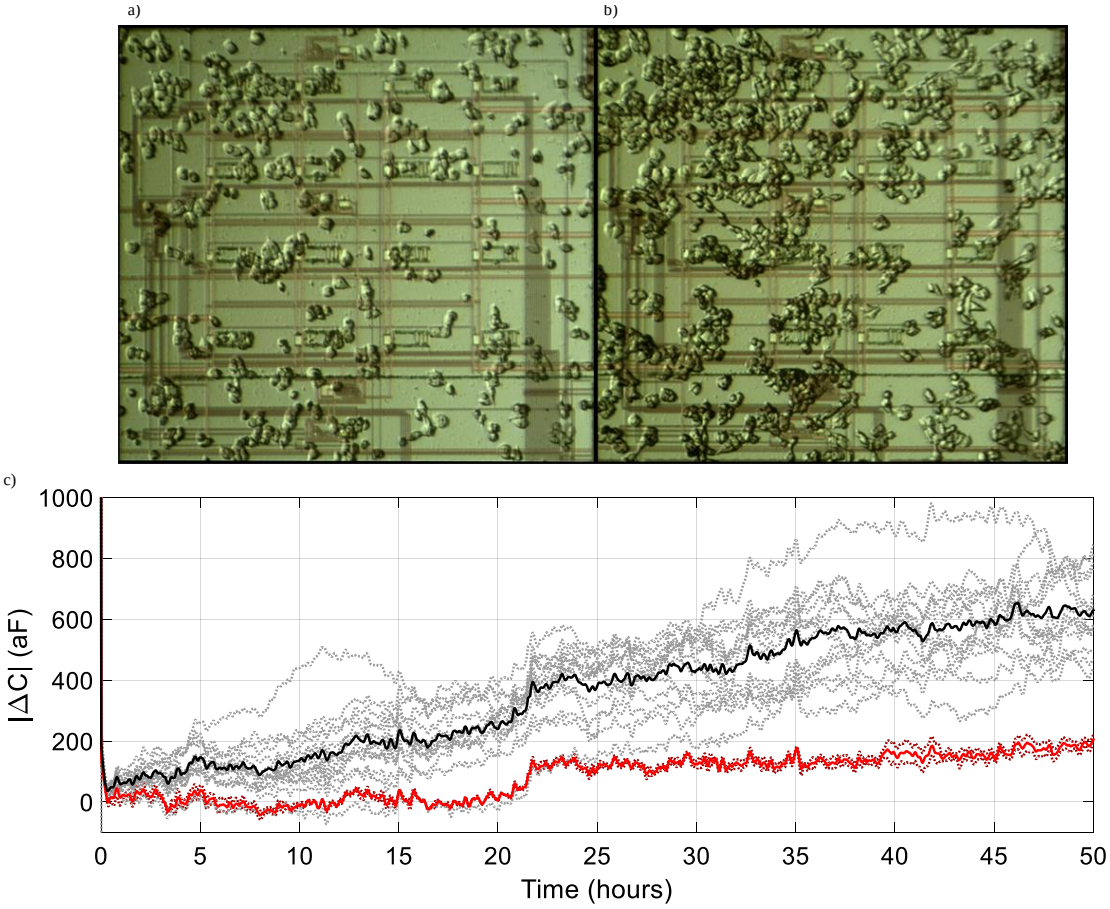

Figure A.7: Results of experiment on Device 1 with A2780 cells. Microscope image of chip surface after a) 21.5 hours and b) 46 hours of incubation. c) Response curves where sensors with and without cell coverage are grouped together. Two sensors observed to have no coverage at the two time intervals (2,4) and (4,3) are shown in dotted red, with their mean as a solid line. The other sensors are shown in dotted black, with mean as a solid line.

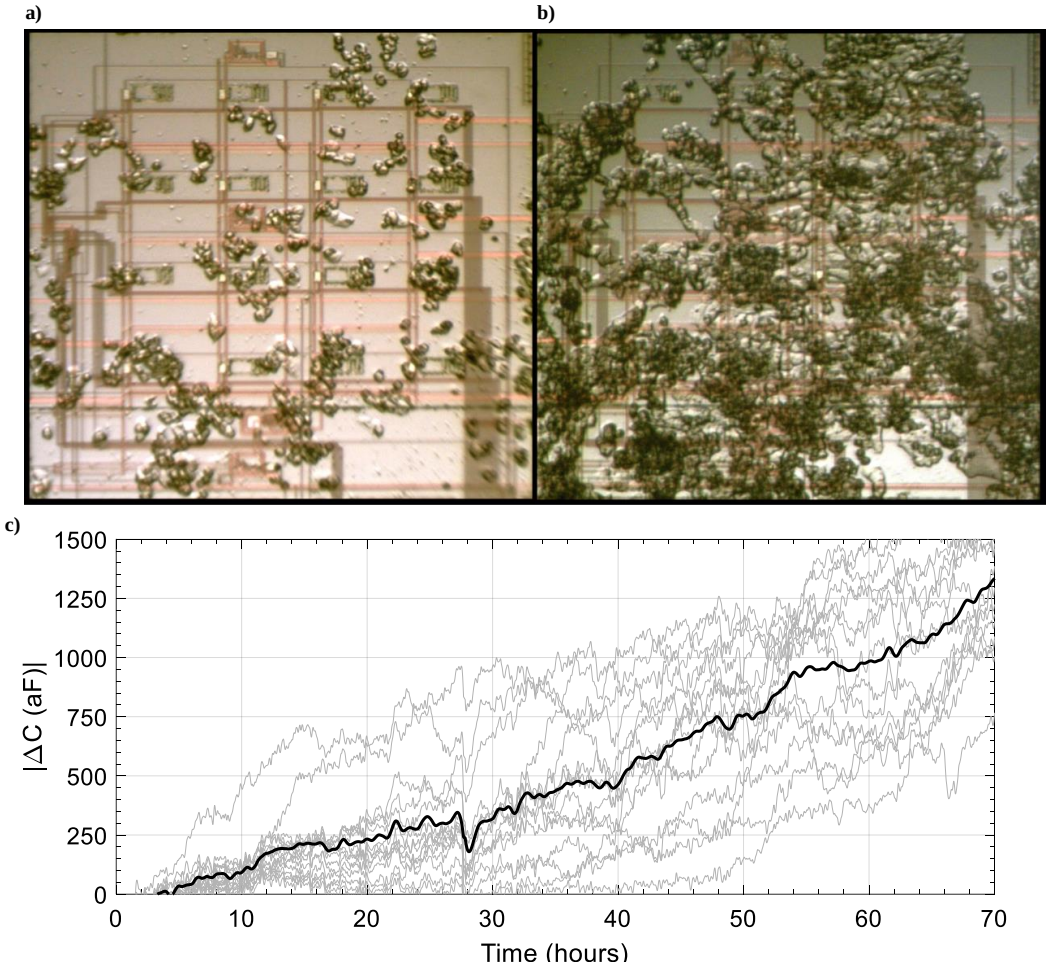

Figure A.8: Results of experiment with A2780 cells. Microscope image of chip surface after a) 27 hours and b) 70 hours of incubation. c) Response curves of sensors with cell coverage in gray, with the mean as a solid black line.

Bibliography

[1] Jeong-Woo Lee, Dong-Jin Min, Jiyoun Kim, and Wonchan Kim. A 600-dpi capacitive fingerprint sensor chip and image-synthesis technique. *IEEE Journal of Solid-State Circuits*, 34(4):469–475, 1999.

[2] J C Chen, D Sylvester, and Chenming Hu. An on-chip, interconnect capacitance characterization method with sub-femto-farad resolution. *IEEE Transactions on Semiconductor Manufacturing*, 11(2):204–210, may 1998.

[3] Michael S.C. Lu, Yi Chung Chen, and Po Chiun Huang. 5x5 CMOS capacitive sensor array for detection of the neurotransmitter dopamine. *Biosensors and Bioelectronics*, 26(3):1093–1097, 2010.

[4] Harvey Lodish, Arnold Berk, S. Lawrence Zipursky, Paul Matsudaira, David Baltimore, and James E. Darnell. *Molecular Cell Biology*. W.H. Freeman, New York, 4 edition, 2000.

[5] I Giaever and C R Keese. Micromotion of mammalian cells measured electrically. *Proceedings of the National Academy of Sciences of the United States of America*, 88(17):7896–7900, 1991.

[6] Timir Datta-Chaudhuri, Elisabeth Smela, and Pamela A. Abshire. System-on-Chip Considerations for Heterogeneous Integration of CMOS and Fluidic Bio-Interfaces. *IEEE Transactions on Biomedical Circuits and Systems*, 10(6):1129–1142, 2016.

[7] Humayun Irshad, Antoine Veillard, Ludovic Roux, and Daniel Racoceanu. Methods for nuclei detection, segmentation, and classification in digital histopathology: A review-current status and future potential. *IEEE Reviews in Biomedical Engineering*, 7:97–114, 2014.

[8] Thermo Scientific. alamarBlue Cell Viability Assay Reagent. Technical report, 2012.

[9] Somashekar Bangalore Prakash and Pamela Abshire. Tracking cancer cell proliferation on a CMOS capacitance sensor chip. *Biosensors and Bioelectronics*, 23(10):1449–1457, 2008.

[10] Numa Couniot, Laurent A Francis, and Denis Flandre. A 16x16 CMOS Capacitive Biosensor Array Towards Detection of Single Bacterial Cell. *IEEE Transactions on Biomedical Circuits and Systems*, 10(2):364–374, 2016.

[11] Ghazal Nabovati, Ebrahim Ghafar-Zadeh, Antoine Letourneau, and Mohamad Sawan. Smart Cell Culture Monitoring and Drug Test Platform Using CMOS Capacitive Sensor Array. *IEEE Transactions on Biomedical Engineering*, 66(4), 2019.

[12] Ghazal Nabovati, Ebrahim Ghafar-zadeh, Antoine Letourneau, and Mohamad Sawan. Towards High Throughput Cell Growth Screening: A New CMOS 8 x 8 Biosensor Array for Life Science Applications. *IEEE Transactions on Biomedical Circuits and Systems*, 11(2):380–391, 2017.

[13] C. Laborde, F. Pittino, H. A. Verhoeven, S. G. Lemay, L. Selmi, M. A. Jongsma, and F. P. Widdershoven. Real-time imaging of microparticles and living cells with CMOS nanocapacitor arrays. *Nature Nanotechnology*, 10(9):791–795, 2015.

[14] Sigma-Aldrich. Cell Viability and Proliferation Assays, 2019.

[15] D. L. Coutu and T. Schroeder. Probing cellular processes by long-term live imaging - historic problems and current solutions. *Journal of Cell Science*, 126(17):3805–3815, 2013.

[16] Yehya H. Ghallab and Yehea Ismail. CMOS based lab-on-a-chip: Applications, challenges and future trends. *IEEE Circuits and Systems Magazine*, 14(2):27–47, 2014.

[17] Ka Meng Lei, Pui In Mak, Man Kay Law, and Rui P. Martins. CMOS biosensors for: In vitro diagnosis-transducing mechanisms and applications. *Lab on a Chip*, 16(19):3664–3681, 2016.

[18] Somashekar Bangalore Prakash and Pamela Abshire. A CMOS capacitance sensor that monitors cell viability. *IEEE Sensors*, 2005:1177–1180, 2005.

[19] Somashekar Bangalore Prakash, Pamela Abshire, Mario Urdaneta, and Elisabeth Smela. A CMOS capacitance sensor for cell adhesion characterization. In *IEEE International Symposium on Circuits and Systems*, pages 3495–3498, 2005.

[20] Elmore Susan. Apoptosis: A Reveiw of Programmed Cell Death. *Toxicologic Pathology*, 35(4):496–516, 2007.

[21] D Sylvester, J C Chen, and Chenming Hu. Investigation of interconnect capacitance characterization using charge-based capacitance measurement (CBCM) technique and three-dimensional simulation. *IEEE Journal of Solid-State Circuits*, 33(3):449–453, mar 1998.

[22] M Tartagni and R Guerrieri. A fingerprint sensor based on the feedback capacitive sensing scheme. *IEEE Journal of Solid-State Circuits*, 33(1):133–142, jan 1998.

[23] Somashekar Bangalore Prakash and Pamela Abshire. A fully differential rail-to-rail CMOS capacitance sensor with floating-gate trimming for mismatch compensation. *IEEE Transactions on Circuits and Systems I: Regular Papers*, 56(5):975–986, 2009.

[24] Ebrahim Ghafar-Zadeh and Mohamad Sawan. Charge-based capacitive sensor array for CMOS-based laboratory-on-chip applications. *IEEE Sensors Journal*, 8(3-4):325–332, 2008.

[25] Ghazal Nabovati, Ebrahim Ghafar-Zadeh, Maryam Mirzaei, Giancarlo Ayala-Charca, Falah Awwad, and Mohamad Sawan. A New Fully Differential CMOS Capacitance to Digital Converter for Lab-on-Chip Applications. *IEEE Transactions on Biomedical Circuits and Systems*, 9(3):353–361, 2014.

[26] Amelia Ahmad Khalili and Mohd Ridzuan Ahmad. A Review of cell adhesion studies for biomedical and biological applications. *International Journal of Molecular Sciences*, 16(8):18149–18184, 2015.

[27] Micah Dembo and Yu-Li Wang. Stresses at the Cell-to-Substrate Interface during Locomotion of Fibroblasts. *Biophysical Journal*, 76(4):2307–2316, 1999.

[28] V K Gupta, Ihab A Sraj, Konstantinos Konstantopoulos, and Charles D Eggleton. Multi-scale simulation of L-selectin–PSGL-1-dependent homotypic leukocyte binding and rupture. *Biomechanics and Modeling in Mechanobiology*, 9(5):613–627, oct 2010.

[29] Kevin V Christ, Kyle B Williamson, Kristyn S Masters, and Kevin T Turner. Measurement of single-cell adhesion strength using a microfluidic assay. *Biomedical Microdevices*, 12(3):443–455, jun 2010.

[30] A Rollan, D McCormack, L McHale, H McCormack, and A P McHale. A rapid in situ, colorimetric assay for the determination of mammalian cell viability in alginate-immobilized and encapsulated systems. *Bioprocess Engineering*, 15(1):47–49, jun 1996.

[31] Anja Schreer, Cheryl Tinson, James P Sherry, and Kristin Schirmer. Application of Alamar blue/5-carboxyfluorescein diacetate acetoxymethyl ester as a noninvasive cell viability assay in primary hepatocytes from rainbow trout. *Analytical Biochemistry*, 344(1):76–85, 2005.

[32] R A Hoebe, C H Van Oven, T W J Gadella, P B Dhonukshe, C J F Van Noorden, and E M M Manders. Controlled light-exposure microscopy reduces photobleaching and phototoxicity in fluorescence live-cell imaging. *Nat Biotech*, 25(2):249–253, feb 2007.

[33] Lavanya Balasubramanian, Kay-Pong Yip, Tai-Hsin Hsu, and Chun-Min Lo. Impedance analysis of renal vascular smooth muscle cells. *American journal of physiology. Cell physiology*, 295:C954–C965, 2008.

[34] J Wegener, a Janshoff, and H J Galla. Cell adhesion monitoring using a quartz crystal microbalance: comparative analysis of different mammalian cell lines. *European biophysics journal : EBJ*, 28(1):26–37, 1999.

[35] Michael Saitakis and Electra Gizeli. Acoustic sensors as a biophysical tool for probing cell attachment and cell/surface interactions. *Cellular and Molecular Life Sciences*, 69(3):357–371, 2012.

[36] M.L. Pourciel-Gouzy, W. Sant, I. Humenyuk, L. Malaquin, X. Dollat, and P. Temple-Boyer. Development of pH-ISFET sensors for the detection of bacterial activity. *Sensors and Actuators B: Chemical*, 103(1-2):247–251, 2004.

[37] Kiichi Niitsu, Shoko Ota, Kohei Gamo, Hiroki Kondo, Masaru Hori, and Kazuo Nakazato. Development of Microelectrode Arrays Using Electroless Plating for CMOS-Based Direct Counting of Bacterial and HeLa Cells. *IEEE Transactions on Biomedical Circuits and Systems*, 9(5):607–619, 2015.

[38] Ivar Giaever and Charles Richard Keese. Monitoring fibroblast behavior in tissue culture with an applied electric field. *Proceedings of the National Academy of Sciences of the United States of America*, 81(12):3761–3764, 1984.

[39] I Giaever and C R Keese. A morphological biosensor for mammalian cells. *Nature*, 366(6455):591–592, 1993.

[40] Ivar Giaever and Charles R Keese. Use of Electric Fields to Monitor the Dynamical Aspect of Cell Behavior in Tissue Culture. *IEEE Transactions on Biomedical Engineering*, BME-33(2):242–247, 1986.

[41] Daniel Opp, Brian Wafula, Jennifer Lim, Eric Huang, Jun-Chih Lo, and Chun-Min Lo. Use of electric cellsubstrate impedance sensing to assess in vitro cytotoxicity. *Biosensors and Bioelectronics*, 24(8):2625–2629, 2009.

[42] Diane S Allen-Gipson, Matthew C Zimmerman, Hui Zhang, Glenda Castellanos, Jennifer K O'Malley, Horacio Alvarez-Ramirez, Kusum Kharbanda, Joseph H Sisson, and Todd A Wyatt. Smoke Extract Impairs Adenosine Wound Healing. Implications of Smoke-Generated Reactive Oxygen Species. *American Journal of Respiratory Cell and Molecular Biology*, 48(5):665–673, 2013.

[43] S. B. Prakash and P. Abshire. On-chip capacitance sensing for cell monitoring applications. *IEEE Sensors Journal*, 7(3):440–447, 2007.

[44] Ebrahim Ghafar-Zadeh, Mohamad Sawan, Vamsy P. Chodavarapu, and Tahereh Hosseini-Nia. Bacteria growth monitoring through a differential CMOS capacitive sensor. *IEEE Transactions on Biomedical Circuits and Systems*, 4(4):232–238, 2010.

[45] Somashekar Bangalore Prakash and Pamela Abshire. A fully differential rail-to-rail capacitance measurement circuit for integrated cell sensing. *Proceedings of IEEE Sensors*, pages 1444–1447, 2007.

[46] Somashekar Bangalore Prakash and Pamela Abshire. A fully differential CMOS capacitance sensor design, testing and array architecture. *Proceedings - IEEE International Symposium on Circuits and Systems*, pages 165–168, 2008.

[47] Timir Datta, Emily Naviasky, and Pamela Abshire. Floating-gate Capacitance Sensor Array for Cell Viability Monitoring. *IEEE Biomedical Circuits and Systems Conference (BioCAS)*, pages 65–68, 2013.

[48] Numa Couniot, David Bol, Olivier Poncelet, Laurent A Francis, and Denis Flandre. A Capacitance-to-Frequency Converter With On-Chip Passivated Microelectrodes for Bacteria Detection in Saline Buffers Up to 575 MHz. *IEEE Transactions on Circuits and Systems II: Express Briefs*, 62(2):159–163, 2015.

[49] Alessia Damilano, Marco Crepaldi, Paolo Motto Ros, and Danilo Demarchi. A 130 nm event-driven voltage and temperature insensitive capacitive ROC. In *7th Euromicro Conference on Digital System Design, DSD 2014*, pages 663–666, 2014.

[50] Timir Datta-Chaudhuri, Pamela Abshire, and Elisabeth Smela. Packaging commercial CMOS chips for lab on a chip integration. *Lab on a chip*, 14(10):1753–66, 2014.

[51] Emily Naviasky, Timir Datta-Chaudhuri, and Pamela Abshire. High resolution capacitance sensor array for real-time monitoring of cell viability. *IEEE International Symposium on Circuits and Systems*, pages 634–637, 2014.

[52] Inc Applied BioPhysics. ECIS - Applied Biophysics, 2017.

[53] V. Tsouti, C. Boutopoulos, I. Zergioti, and S. Chatzandroulis. Capacitive microsystems for biological sensing. *Biosensors and Bioelectronics*, 27(1):1–11, 2011.

[54] N. Couniot, A. Afzalian, N. Van Overstraeten-Schlögel, L. A. Francis, and D. Flandre. Capacitive biosensing of bacterial cells: Analytical model and numerical simulations. *Sensors and Actuators, B: Chemical*, 211:428–438, 2015.

[55] Bathiya Senevirathna, Alexander Castro, Marc Dandin, Elisabeth Smela, and Pamela Abshire. Lab-on-CMOS Capacitance Sensor Array for Real- Time Cell Viability Measurements with I2C Readout. *IEEE International Symposium on Circuits and Systems*, pages 2863–2866, 2016.

[56] Bathiya Senevirathna, Sheung Lu, and Pamela Abshire. Characterization of a High Dynamic Range Lab-on-CMOS Capacitance Sensor Array. *IEEE International Symposium on Circuits and Systems (ISCAS)*, pages 1–4, 2017.

[57] Bathiya Prashan Senevirathna, Sheung Lu, Marc P. Dandin, John Basile, Elisabeth Smela, and Pamela A. Abshire. Real-Time Measurements of Cell Proliferation Using a Lab-on-CMOS Capacitance Sensor Array. *IEEE Transactions on Biomedical Circuits and Systems*, 12(3):510–520, 2018.

[58] Boris Andreev, Edward L Titlebaum, and EBY G Friedman. Sizing CMOS Inverters with Miller Effect and Threshold Voltage Variations. *Journal of Circuits, Systems, and Computers, World Scientific*, 15(3):437–454, 2006.

[59] Asad A. Abidi. Phase noise and jitter in CMOS ring oscillators. *IEEE Journal of Solid-State Circuits*, 41(8):1803–1816, 2006.

[60] Yu Shiang Lin, Dennis Sylvester, and David Blaauw. An ultra low power 1V, 220nW temperature sensor for passive wireless applications. In *Proceedings of the Custom Integrated Circuits Conference*, pages 507–510, 2008.

[61] Steve Fielding. I2C Slave - Minimalist I2C slave IP core that provides the basic framework for the implementation of custom I2C slave devices, 2013.

[62] University of Washington. Dielectric constants of common solvents.

[63] Tsung Hsueh Lee and Pamela A. Abshire. Frequency-Boost Jitter Reduction for Voltage-Controlled Ring Oscillators. *IEEE Transactions on Very Large Scale Integration (VLSI) Systems*, 24(10):3156–3168, 2016.

[64] Thermo Scientific. Thermo Scientific Forma Series 3 Water Jacketed CO2 Incubator, 2015.

[65] Microchip. MCP1703 Datasheet, 2010.

[66] Sheung Lu, Bathiya Senevirathna, Marc Dandin, Elisabeth Smela, and Pamela Abshire. System Integration of IC chips for Lab-on-CMOS Applications. *2018 IEEE International Symposium on Circuits and Systems (ISCAS)*, pages 2–6, 2018.

[67] Niina Halonen, Joni Kilpijärvi, Maciej Sobocinski, Timir Datta-Chaudhuri, Antti Hassinen, Someshekar B. Prakash, Peter Möller, Pamela Abshire, Sakari Kellokumpu, and Anita Lloyd Spetz. Low temperature co-fired ceramic packaging of CMOS capacitive sensor chip towards cell viability monitoring. *Beilstein Journal of Nanotechnology*, 7(1):1871–1877, 2016.

[68] Joni Kilpijärvi, Niina Halonen, Maciej Sobocinski, Antti Hassinen, Bathiya Senevirathna, Kajsa Uvdal, Pamela Abshire, Elisabeth Smela, Sakari Kellokumpu, Jari Juuti, and Anita Lloyd Spetz. LTCC Packaged Ring Oscillator Based Sensor for Evaluation of Cell Proliferation. *Sensors*, 18(10):3346, 2018.

[69] Ryan J Petrie, Andrew D Doyle, and Kenneth M Yamada. Random versus directionally persistent cell migration. *Nature reviews. Molecular cell biology*, 10(8):538–549, 2009.

[70] Richard Kasprowicz, Rakesh Suman, and Peter O'Toole. Characterising live cell behaviour: Traditional label-free and quantitative phase imaging approaches. *International Journal of Biochemistry and Cell Biology*, 84:89–95, 2017.

[71] Fuyong Xing and Lin Yang. Robust nucleus/cell detection and segmentation in digital pathology and microscopy images: A comprehensive review. *IEEE Reviews in Biomedical Engineering*, 9:234–263, 2016.

[72] Leica Microsystems. Immersion Objectives: Using Oil, Glycerol, or Water to Overcome some of the Limits of Resolution, 2017.

[73] Rachel Bareither and David Pollard. A review of advanced small-scale parallel bioreactor technology for accelerated process development: Current state and future need. *Biotechnology Progress*, 27(1):2–14, 2011.

[74] Di Jin, Dennis Wong, Junxiang Li, Zhang Luo, Yiran Guo, Bifeng Liu, Qiong Wu, Chih-Ming Ho, and Peng Fei. Compact Wireless Microscope for In-Situ Time Course Study of Large Scale Cell Dynamics within an Incubator. *Scientific Reports*, 5(1):18483, 2016.

[75] Nikon Instruments Inc. Nikon BioStation IM-Q, 2017.

[76] World Precision Instruments. Microscope Environmental Chamber, Heat and CO2 controller, 2017.

[77] GE Healthcare Life Sciences. Cytell Cell Imaging System, 2017.

[78] Leica Microsystems. Inverted Microscope Platform Leica DMi8, 2017.

[79] Marco Ballini, Jan Muller, Paolo Livi, Yihui Chen, Urs Frey, Alexander Stettler, Amir Shadmani, Vijay Viswam, Ian Lloyd Jones, David Jackel, Milos Radivojevic, Marta K. Lewandowska, Wei Gong, Michele Fiscella, Douglas J. Bakkum, Flavio Heer, and Andreas Hierlemann. A 1024-channel CMOS microelectrode array with 26,400 electrodes for recording and stimulation of electrogenic cells in vitro. *IEEE Journal of Solid-State Circuits*, 49(11):2705–2719, 2014.

[80] Jelena Dragas, Vijay Viswam, Amir Shadmani, Yihui Chen, Raziyeh Bounik, Alexander Stettler, Milos Radivojevic, Sydney Geissler, Marie Engelene J. Obien, Jan Müller, and Andreas Hierlemann. In Vitro Multi-Functional Microelectrode Array Featuring 59 760 Electrodes, 2048 Electrophysiology Channels, Stimulation, Impedance Measurement, and Neurotransmitter Detection Channels. *IEEE Journal of Solid-State Circuits*, 52(6):1576–1590, 2017.

[81] A. Lambacher, M. Jenkner, M. Merz, B. Eversmann, R. A. Kaul, F. Hofmann, R. Thewes, and P. Fromherz. Electrical imaging of neuronal activity by multi-transistor-array (MTA) recording at 7.8 μm resolution. *Applied Physics A: Materials Science and Processing*, 79(7):1607–1611, 2004.

[82] K. Imfeld, A. Garenne, S. Neukom, A. Maccione, S. Martinoia, M. Koudelka-Hep, and L. Berdondini. High-resolution MEA platform for in-vitro electrogenic cell networks imaging. *IEEE Engineering in Medicine and Biology - Proceedings*, pages 6085–6088, 2007.

[83] Jong Seok Park, Moez Karim Aziz, Sensen Li, Taiyun Chi, Sandra Ivonne Grijalva, Jung Hoon Sung, Hee Cheol Cho, and Hua Wang. 1024-Pixel CMOS Multimodality Joint Cellular Sensor/Stimulator Array for Real-Time Holistic Cellular Characterization and Cell-Based Drug Screening. *IEEE Transactions on Biomedical Circuits and Systems*, 12(1):80–94, 2018.

[84] Taiyun Chi, Jong Seok Park, Jessica Butts, Tracy Hookway, Amy Su, Chengjie Zhu, Mark Styczynski, Todd McDevitt, and Hua Wang. A multimodality CMOS sensor array for cell-based assay and drug screening. *IEEE Transactions on Biomedical Circuits and Systems*, 9(6):801–814, 2015.

[85] Jong Seok Park, Sandra I Grijalva, Moez K Aziz, Taiyun Chi, Sensen Li, Michael N Sayegh, Adam Wang, Hee Cheol Cho, and Hua Wang. Multiparametric cell profiling with a CMOS quad-modality cellular interfacing array for label-free fully automated drug screening. *Lab on a Chip*, 18(19):3037–3050, 2018.

[86] Carolina Mora Lopez, Ho Sung Chun, Shiwei Wang, Laurent Berti, Jan Putzeys, Carl Van Den Bulcke, Jan Willem Weijers, Andrea Firrincieli, Veerle Reumers, Dries Braeken, and Nick Van Helleputte. A multimodal CMOS MEA for high-throughput intracellular action potential measurements and impedance spectroscopy in drug-screening applications. *IEEE Journal of Solid-State Circuits*, 53(11):3076–3086, 2018.

[87] Jeffrey Abbott, Tianyang Ye, Ling Qin, Marsela Jorgolli, Rona S. Gertner, Donhee Ham, and Hongkun Park. CMOS nanoelectrode array for all-electrical intracellular electrophysiological imaging. *Nature Nanotechnology*, 12(5):460–466, 2017.

[88] Erik Meijering. Cell Segmentation: 50 Years Down the Road. *IEEE Signal Processing Magazine*, 29(5):140–145, 2012.

[89] Nobuyuki Otsu. A Threshold Selection Method from Gray-Level Histograms. *IEEE Transactions on Systems, Man, and Cybernetics*, 9(1):62–66, 1979.

[90] D Andreou, P Reichardt, M Werner, M Schuler, B Jobke, D Pink, G Gosheger, F Traub, and P U Tunn. Prognostic relevance of the mitotic count and the amount of viable tumour after neoadjuvant chemotherapy for primary, localised, high-grade soft tissue sarcoma. *British Journal of Cancer*, 112(3):455–460, 2014.

[91] Mitko Veta, Paul J. Van Diest, Mehdi Jiwa, Shaimaa Al-Janabi, and Josien P.W. Pluim. Mitosis counting in breast cancer: Object-level interobserver agreement and comparison to an automatic method. *PLoS ONE*, 11(8):1–8, 2016.

[92] Michael Bonert and Angela J. Tate. Mitotic counts in breast cancer should be standardized with a uniform sample area. *BioMedical Engineering Online*, 16(1):1–8, 2017.

[93] Jean-michel Coindre. Grading of soft tissue sarcomas. *Archives of pathology & laboratory medicine*, 130(10):1448–1453, 2006.

[94] Humayun Irshad, Sepehr Jalali, Ludovic Roux, Daniel Racoceanu, Lim Joo Hwee, Gilles Le Naour, and Frédérique Capron. Automated mitosis detection using texture, SIFT features and HMAX biologically inspired approach. *Journal of Pathology Informatics*, 4(2):12, 2013.

[95] Seungil Huh, Dai Fei Elmer Ker, Ryoma Bise, Mei Chen, and Takeo Kanade. Automated Mitosis Detection of Stem Cell Populations in Phase-Contrast Microscopy Images. *IEEE Transactions on Medical Imaging*, 30(3):586–596, 2010.

[96] Antoine Veillard, Maria S Kulikova, and Daniel Racoceanu. Cell nuclei extraction from breast cancer histopathologyimages using colour, texture, scale and shape information. *Diagnostic Pathology*, 8(S1):8–10, 2013.

[97] Christopher Malon, Elena Brachtel, Eric Cosatto, Hans Peter Graf, Atsushi Kurata, Masahiko Kuroda, John S. Meyer, Akira Saito, Shulin Wu, and Yukako Yagi. Mitotic figure recognition: Agreement among pathologists and computerized detector. *Analytical Cellular Pathology*, 35(2):97–100, 2012.

[98] Ashkan Tashk, Mohammad Sadegh Helfroush, Habibollah Danyali, and Mojgan Akbarzadeh. An automatic mitosis detection method for breast cancer histopathology slide images based on objective and pixel-wise textural features classification. *Conference on Information and Knowledge Technology (ITK)*, pages 406–410, 2013.

[99] Dan C Cirean, Alessandro Giusti, Luca M Gambardella, and Jürgen Schmidhuber. Mitosis Detection in Breast Cancer Histology Images with Deep Neural Networks BT - Medical Image Computing and Computer-Assisted Intervention MICCAI 2013. *Proceedings of Medical Image Computing and Computer-Assisted Intervention (MICCAI)*, pages 411–418, 2013.

[100] Monjoy Saha, Chandan Chakraborty, and Daniel Racoceanu. Efficient deep learning model for mitosis detection using breast histopathology images. *Computerized Medical Imaging and Graphics*, 64(March 2017):29–40, 2018.

[101] Alessandro Giusti, Claudio Caccia, Dan C. Ciresari, Jurgen Schmidhuber, and Luca M. Gambardella. A comparison of algorithms and humans for mitosis detection. *2014 IEEE 11th International Symposium on Biomedical Imaging (ISBI)*, pages 1360–1363, 2014.

[102] David O. Morgan. *The Cell Cycle: Principles of Control*. New Science Press, London, 2007.

[103] M.A. Dickson and G.K. Schwartz. Development of cell-cycle inhibitors for cancer therapy. *Current Onocology*, 16(2):36–43, 2009.

[104] Carmen Dominguez-Brauer, Kelsie L. Thu, Jacqueline M. Mason, Heiko Blaser, Mark R. Bray, and Tak W. Mak. Targeting Mitosis in Cancer: Emerging Strategies. *Molecular Cell*, 60(4):524–536, 2015.

[105] Charles J. Sherr and Jiri Bartek. Cell CycleTargeted Cancer Therapies. *Annual Review of Cancer Biology*, 1(1):41–57, 2016.

[106] Perry J Kaufman. *Trading Systems and Methods*. John Wiley & Sons, Incorporated, Somerset, UNITED STATES, 2013.

[107] Christina L. Dix, Helen K. Matthews, Marina Uroz, Susannah McLaren, Lucie Wolf, Nicholas Heatley, Zaw Win, Pedro Almada, Ricardo Henriques, Michael Boutros, Xavier Trepat, and Buzz Baum. The Role of Mitotic Cell-Substrate Adhesion Re-modeling in Animal Cell Division. *Developmental Cell*, 45(1):132–145, 2018.

[108] John G. Lock, Matthew C. Jones, Janet A. Askari, Xiaowei Gong, Anna Oddone, Helene Olofsson, Sara Göransson, Melike Lakadamyali, Martin J. Humphries, and Staffan Strömblad. Reticular adhesions are a distinct class of cell-matrix adhesions that mediate attachment during mitosis. *Nature Cell Biology*, 20(11):1290–1302, 2018.

[109] Manuela F. Azzola, Helen M. Shaw, John F. Thompson, Seng-jaw Soong, Richard A. Scolyer, Geoffrey F. Watson, Marjorie H. Colman, and Yuting Zhang. Tumor mitotic rate is a more powerful prognostic indicator than ulceration in patients with primary cutaneous melanoma. *Cancer*, 97(6):1488–1498, 2003.

[110] Benoite Méry, Jean-Baptiste Guy, Alexis Vallard, Sophie Espenel, Dominique Ardail, Claire Rodriguez-Lafrasse, Chloé Rancoule, and Nicolas Magné. In Vitro Cell Death Determination for Drug Discovery: A Landscape Review of Real Issues. *Journal of Cell Death*, 10, 2017.

[111] E III. Frei and JP Eder. *Combination Chemotherapy*. BC Decker, Hamilton, 6th edition, 2003.

[112] Robert A Gatenby, Ariosto S Silva, Robert J Gillies, and B Roy Frieden. Adaptive Therapy. *Cancer Research*, 69(11):4894–4903, 2009.

[113] B. Zhao, M. T. Hemann, and D. A. Lauffenburger. Intratumor heterogeneity alters most effective drugs in designed combinations. *Proceedings of the National Academy of Sciences*, 111(29):10773–10778, 2014.

[114] John O'Brien, Ian Wilson, Terry Orton, and François Pognan. Investigation of the Alamar Blue (resazurin) fluorescent dye for the assessment of mammalian cell cytotoxicity. *European Journal of Biochemistry*, 267(17):5421–5426, 2000.

[115] Thermo Scientific. alamarBlue Assay for Cell Viability, 2019.

[116] Frans Widdershoven, Andrea Cossettini, Cecilia Laborde, Andrea Bandiziol, Paul P Van Swinderen, Serge G Lemay, and Luca Selmi. A CMOS Pixelated Nanocapacitor Biosensor Platform for High-Frequency Impedance Spectroscopy and Imaging. *IEEE Transactions on Biomedical Circuits and Systems*, 12(6):1369–1382, 2018.

[117] Glenn M. Walker, Nancy Monteiro-Riviere, Jillian Rouse, and Adrian T. O'Neill. A linear dilution microfluidic device for cytotoxicity assays. *Lab on a Chip*, 7(2):226–232, 2007.

[118] Choong Kim, Kangsun Lee, Jong Hyun Kim, Kyeong Sik Shin, Kyu Jung Lee, Tae Song Kim, and Ji Yoon Kang. A serial dilution microfluidic device using a ladder network generating logarithmic or linear concentrations. *Lab on a Chip*, 8(3):473–479, 2008.

[119] R Baker. *CMOS : Circuit Design, Layout, and Simulation*. IEEE Press/Wiley, Hoboken, N.J, third edition, 2010.